DOUG LE1000

Deep Ocean Underwater Glider,
Long Endurance 1000m-rated

Year II of the
“Idea on Monday, Deployment on Wednesday”
Innovation Cycle

2.013 Engineering Systems Design

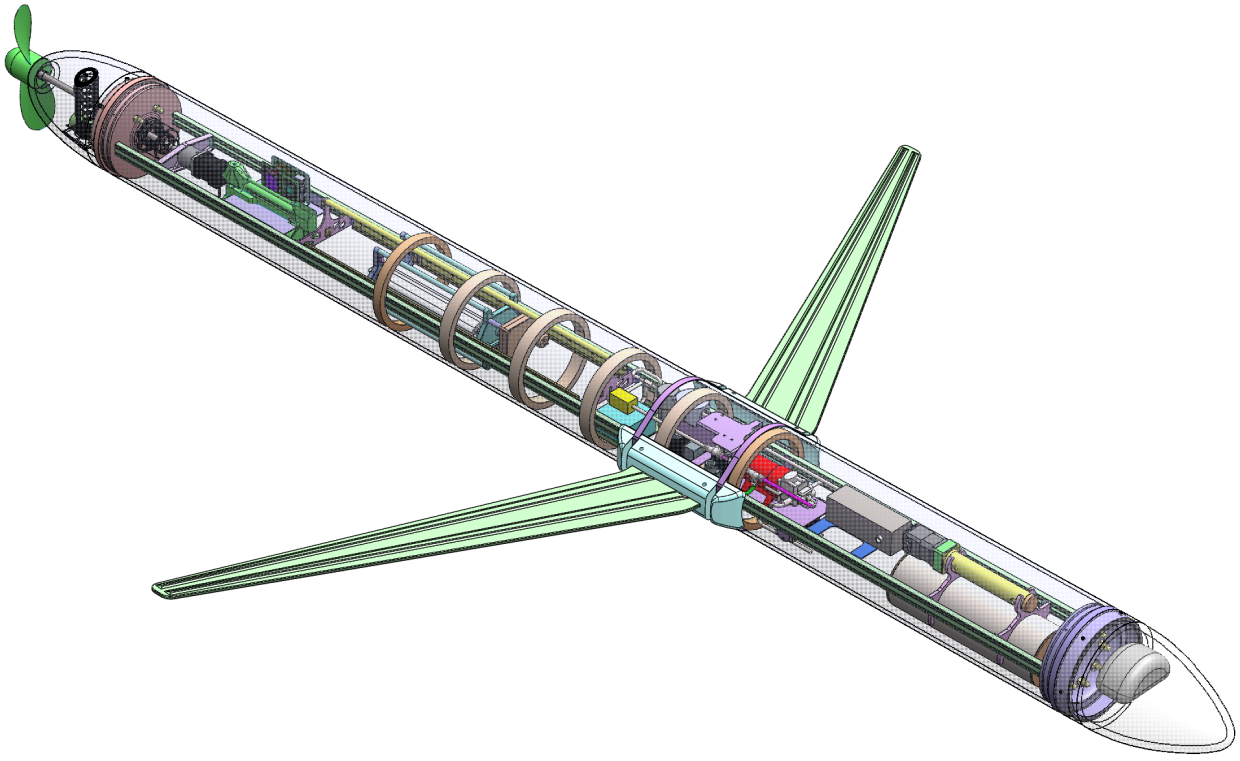

Office of Naval Research ONR Science & Technology

LINCOLN LABORATORY
MASSACHUSETTS INSTITUTE OF TECHNOLOGY

WOODS HOLE OCEANOGRAPHIC INSTITUTION 1930

ENGINEERING SYSTEMS DESIGN DEVELOPMENT 2.013 2.014

Executive Summary

“Two thirds of the earth's surface and 99% of the earth's biosphere, the volume of the earth that supports life, is ocean yet we currently monitor less that 2% of it and we have explored less than 5% of it.” Developments in unmanned underwater vehicle (UUV) technology have enabled the sampling of oceanographic data and allowed operators a greater access to this historically challenging operating environment, yet there are still significant opportunities for innovation in the UUV space.

We build on the work of the 2019-2020 2.013/4 team. The previous year’s vehicle, RAPID, utilized a piston-based buoyancy engine to profile a vertical column of up to 1000m below sea level. The key innovation behind RAPID was leveraging mechanical simplicity to enable value at scale. Deploying multiple RAPID vehicles through a swarm data sampling strategy is now a potential reality.

This year, our team used RAPID’s design as a starting point to build a vehicle capable of a 30-day endurance with a 2 knot burst speed and a 0.2 knot cruise speed. Our vehicle, Deep Ocean Underwater Glider (DOUG) Long-Endurance (LE), affectionately named DOUG for short, utilizes a hybrid propulsion design to meet the endurance and speed requirements. A buoyancy engine utilizes hydrogen produced by a novel aluminum-water reaction, which is also used for a hydrogen PEM fuel cell, the primary energy system. The buoyancy engine is supported by glider wings and a propeller, which allows us to achieve energy efficient movement while retaining our burst speed capability. DOUG also hosts a suite of navigation, communication, controls, and electronics equipment that utilize novel swarm-capable methods for improving our data sampling abilities. Lastly, DOUG’s mechanical design, including the structural hull and individual subsystems, have been motivated by a mission to keep total manufacturing costs under $50K.

Inspired by feedback from sponsors during the design process, we aimed to contextualize this year’s design with a 4-year plan to ultimately deliver an entirely new paradigm for UUVs -- *Idea on Monday, Deployment on Wednesday*. Building on last year’s sampling and swarm innovation with this year’s long endurance innovation means that we are on track to making the vision of *Idea on Monday, Deployment on Wednesday* a reality.

Acknowledgements

The team would like to thank the following for their contributions to our project.

The 2.014 RAPID development team: **Samer Awale, Max Beeman, Thi Bui, Mateo Correa, Nicholas Fritzinger-Pittman, Caela G. Gomes, Jeevesh Konuru, Sandra Li, Christina Meyer, Lance Neil, Jadorian Paul, Joseph Pierre, Vianna Quenon, Max Raven, Emilio Sison, Miana Smith, and Oscar Zheng.**

Doug Hart, **Michael Wardlaw** and **Jean Sack**, the 2.013 instructors, for their patience, guidance and expertise during this challenging virtual semester. They provided the critical structure necessary for the class to come together and gently steered our decision-making process through many obstacles.

Michael Trice and **Juergen Schoenstein**, the 2.013 communications instructors, for their careful attention during length design reviews, and their thoughtful feedback even during late-night practice runs.

Our generous WHOI sponsors, **Mike Abbot and Chuck Sears,** and their feedback during the semester.

David Larson, for his incredible depth of knowledge on fluids, math, and so much more, without whom we would have been stranded in a mathematical sea.

Joseph Olson, owner of **Cetacean Research Technology**, for his insight on underwater acoustic hydrophones and projectors.

Guy Farruggia and **Jim Friel**, fellow and principal electrical engineer at Areté Associates, for their guidance on future directions for the sensor package, cost drivers, and sensing performance tradeoffs.

Jim Windgassen, engineering fellow at Northrup Grunman and inventor of NIOBICON connectors, for providing us the opportunity to incorporate new underwater connectors in our vehicle.

Reza Ghaffarivardavagh and the MIT Media Lab's Signal Kinetics group for introducing us to piezo-acoustic backscattering and developments in battery-free underwater communication technology.

Charles Dawson of MIT's Model-based Embedded and Robotics Systems Lab for steering us towards key navigation techniques.

Jennifer Zimmerman and **Vince Jelsema**, manager and engineer at Sea-Bird Scientific, for providing technical information on Sea-Bird's CTDs.

Peter Godart, PhD Candidate, for providing guidance on aluminum-water reaction and providing preliminary experimentation of aluminum reaction in oil.

Team Roster

Hydro Team
Shantanu Jakhete*^
Emma Kelley
Audrey Gaither
Becca McCabe
Max Halkenhauser
Hayden Stalter
Marcus Badgett
Sam Gantman

Energy Team
Linda Pratto*
Chad Wilson
Gerhard Rencken
Aleks Siemenn

Navtronics Team
Julia Wyatt*
George Chen
Tyler Ray
Gavin Vandenberg
Makita Erni
Yehoon Lee
Isaac Martinez

Structures Team
Zach Kutschke*
Ryan Koeppen
Johnson Huynh
Sophia Cheung
Daysia Douglas
Minsu Jung
Sam Alyassini

* Subteam CTO ^Team CTO

Table of Contents

List of figures

List of tables

1 Background and Motivation

1.1 Motivation

The ocean is a challenging environment. To quote from the original problem statement, “Two thirds of the earth's surface and 99% of the earth's biosphere, the volume of the earth that supports life, is ocean yet we currently monitor less that 2% of it and we have explored less than 5% of it. Fundamentally, we are blind to what is going on in our own backyard.” To contextualize the ocean problem space, we propose potential use cases or areas of interest:

1. *Algae bloom detection*: Harmful algal blooms, also called "red tide", are defined by photosynthetic organisms growing out of control. These blooms are typically detected by satellite imagery, but this is limited by surface visual condition.
2. *Oil spill detection*: Oil spills cause potentially catastrophic economic and environmental damage, and current methods for tracking oil spill movement are limited to surface monitoring, usually through imagery. Being able to track the boundary of plumes, especially at depth, could offer better insight to the oil spill movement.
3. *Pipeline Inspection*: Pipeline corrosion and cracking detection is an arduous and expensive process, with potentially catastrophic environmental consequences if not inspected regularly. Reducing the time to complete inspection missions would make pipelines safer and more economical.
4. *Plastic pollution characterization:* While research typically leverages satellite and aerial imagery to characterize plastic pollution, there is a need to investigate plastic content at depth. More research, especially to characterize movement of plastic at various depths could aid monitoring and mitigation methods.
5. *Fish stock monitoring:* Global fish stocks in biologically sustainable levels have decreased over time, and commercial fishing waters are typically overfished. Current methods of evaluation, such as trawling, are expensive and inaccurate, so an improved data sampling strategy could improve fishing policies and regulations.

There are two main takeaways from the use cases: (1) All require frequent, long term, subsurface data collection and transfer and (2) all result in money, labor, and/or wildlife saved if detected earlier. Unmanned underwater vehicles (UUVs) provide the best opportunities to solve these problems.

1.2 System requirements

The requirements for the entire vehicle package presented here are derived from a combination of sources. First are specifications made by various sponsors and instructors, then any additional requirements derived from those primary ones, and then finally tertiary ones driven by the RAPID system.

Requirement	Value	Reasoning
Depth	1000 m	Sponsor Requirement
Max Speed	2 knots (1 m/s)	Sponsor Requirement
Duration	30 days	Sponsor Requirement
Max Payload Power	200 W	Instructor Requirement
Max Scan Area/ Distance*	400 km	From Sample Use Cases
Max Cost*	$50k	From RAPID
Max Size / Weight*	80kg	From RAPID
Max Data Latency*	1 hour	From RAPID

Table 0: **Overall System Requirements.** Note that requirements marked with an asterisk are not mandatory requirements

The table above highlights the given system requirements (the derived requirements will appear in their relevant subsections). The maximum range we are targeting was yielded early on from a preliminary study of a few sample use cases that we might employ DOUG to, such as in oil spill boundary characterizations and pipeline free span detection. For instance, it was determined that 400 km would cover the length of roughly 75% of undersea pipelines, and would have also allowed us to scan a significant portion of the perimeter of the Deepwater Horizon oil spill. Currently, our system does not meet this requirement on its own though if used as part of a swarm of vehicles it would be trivial. Past this, the only strongly imposed requirements came from our instructors and sponsors, which were for the maximum operating depth, peak payload power, and the mission duration. From the RAPID system we also derived some soft requirements for the system size and cost. We are looking to manufacture each system for $50K or less (the cost of RAPID), and we wish to stay within a size and weight limit such that it would be reasonable to deploy and recover the system from a

small boat/vessel with a 2-man crew. This latter consideration was intended to make DOUG far simpler and cheaper to use.

1.3 System Overview

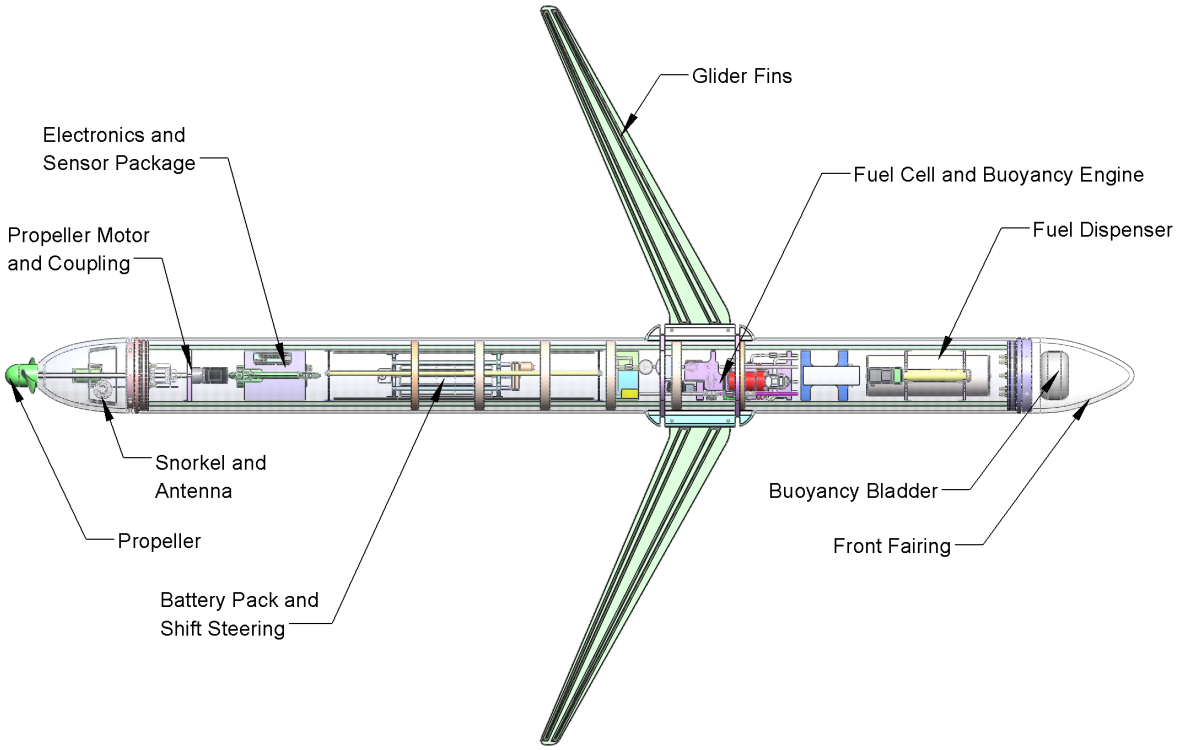

Table 1: **Summary of system specs.**

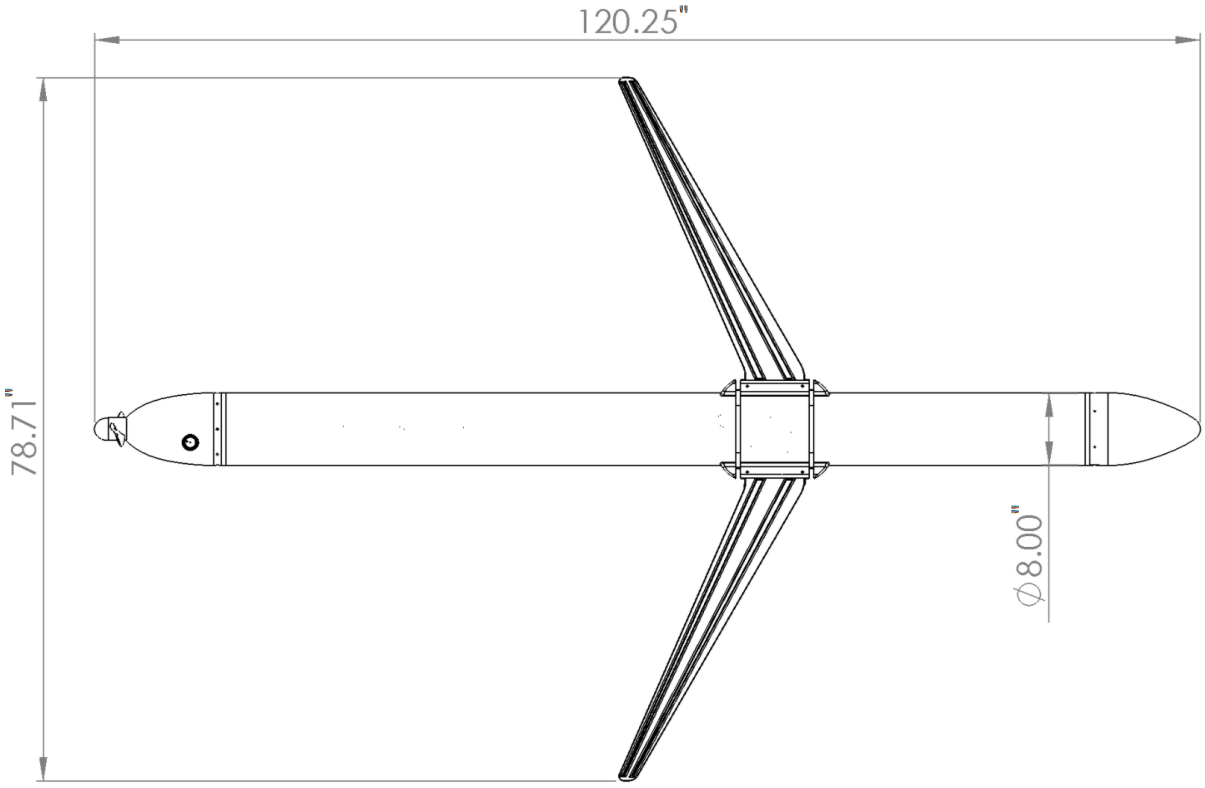

Variable	Value
Total Est. Weight	77 kg
Total Est. Cost	$19,500
Length	120.25 in. / 3.05 m
Wingspan	78.71 in. / 2.00 m
Outer Hull Diameter	8.0 in.
Inner Hull Diameter	7.5 in.

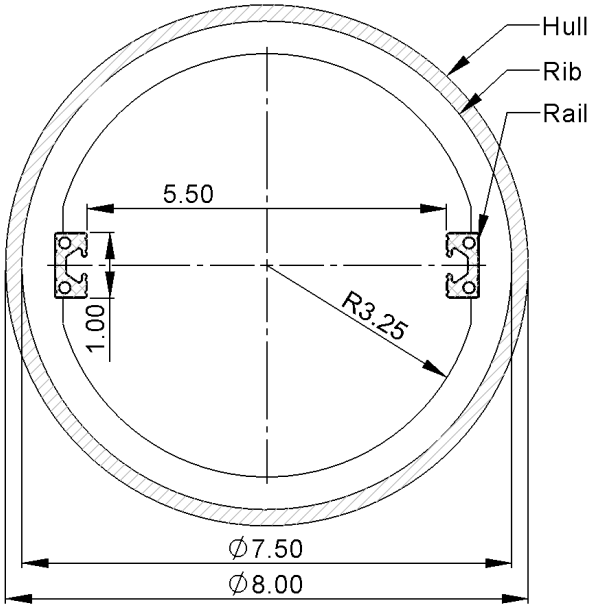

1.4 Design Strategy

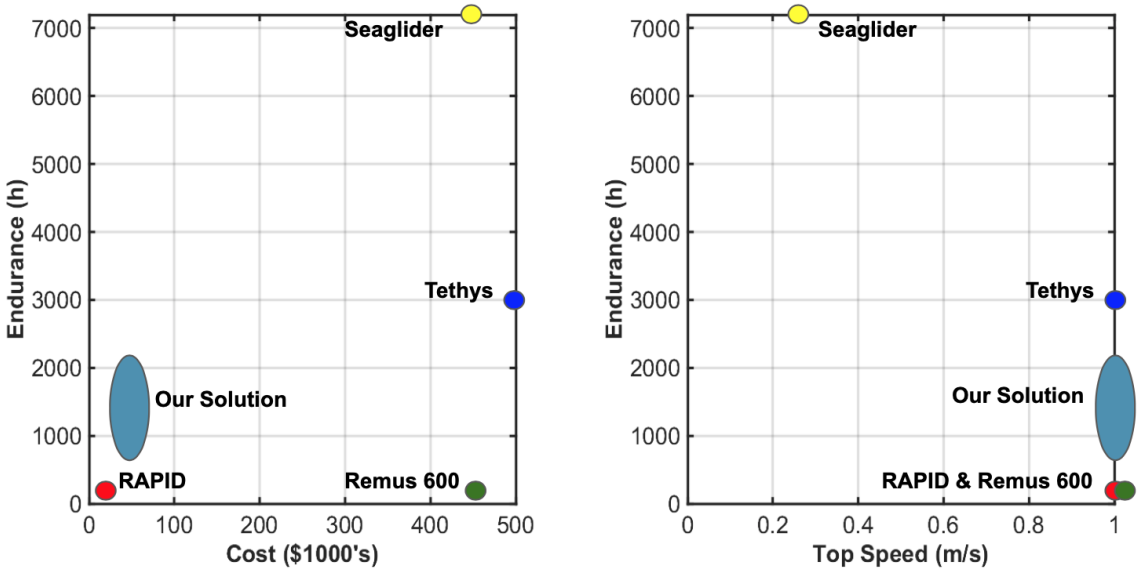

The current paradigm for ocean exploration and UUV usage is slow and poses high barriers of entry to new innovators. Technology is developed on a custom-basis and platforms are typically designed for singular use-cases, which means development is expensive and lengthy. Some companies aim to solve this issue by leveraging a service model, which defrays capital expenditure costs to operators, however, this still doesn't address the issue of a rapid-turnaround capability. This issue is largely a function of the

current UUV deployment methods - because most UUVs measure endurance in a matter of hours , they are restricted to being supported by a surface vessel. In the case of research UUVs, this typically means staffing and operating a research vessel, which also means there is a bottleneck in deploying sensing missions quickly, or in a cost-effective manner. As shown in the figure above, our main goal was to provide value innovation by extending the endurance and maintaining the price point of RAPID.

The design process for DOUG was one of disruptive innovation. To avoid the issues with the current paradigm (designing for singular use cases), the design process worked backwards to develop capabilities, almost agnostic of use cases. This approach of disruptive innovation allowed for a higher risk appetite and for the eventual development of a system that has more potential and applicability.

1.5 Idea on Monday, Deployment on Wednesday

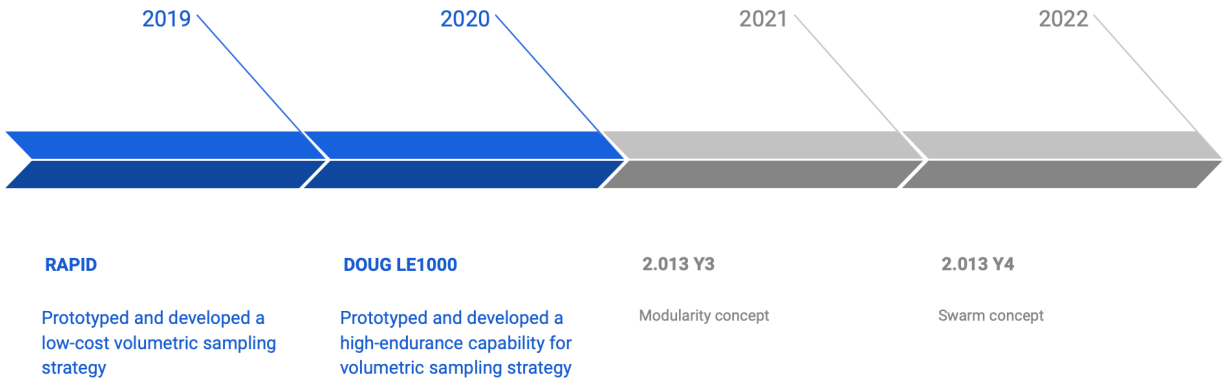

During the design process this semester, sponsors expressed interest in a system that enabled “an ***idea on Monday, and deployment on Wednesday***”. An ambitious idea, this vision represents an entirely new paradigm of ocean research. Reducing the barriers of entry for both veteran researchers and newcomers would accelerate oceanographic research to an entirely new level.

To contextualize this vision and provide an actual pathway to achieving it, several key innovation checkpoints were proposed, as part of a 4-year plan. RAPID is considered year 1, which prototyped and introduced a new cost-effective volumetric sampling strategy. This year, DOUG expands on RAPID by introducing a long-endurance capability to the underlying volumetric sampling strategy. Although a more detailed study is warranted, we identified modularity and development of the swarm concept as the two remaining technical checkpoints in the 4-year plan. Modularity would enable

operators greater flexibility in deploying UUVs. Improving the process for manufacturing, assembly, and essentially retrofitting UUVs for different mission types would mean a quick-turnaround capability could be reached. All of these distinct innovations would culminate at the end in the actual swarm concept scoped in the original RAPID design.

In any case, the vision for “Idea on Monday, Deployment on Wednesday” has helped contextualize the design process and has provided a pathway for moving RAPID and DOUG closer to actual use.

2 Energy system

This section describes the energy system which is designed to power DOUG for a 30-day mission. The system must power all of the components used for propulsion, control, navigation, communication, and data acquisition.

It was determined early in the design process that a simple battery system, typically used on UUVs, would become too massive to be feasible. In addition, lithium-ion batteries were not encouraged by the customer due to safety concerns. Instead of relying on battery storage alone, vehicle endurance is achieved while minimizing weight and size requirements through a hybrid energy system. The system consists of an aluminum-powered hydrogen proton exchange membrane (PEM) fuel cell and a photo-voltaic (PV) array, which are used in conjunction to charge a Nickel-Metal Hydride (NiMH) battery pack. This section describes the integration of these subsystems to meet DOUG's power and endurance needs.

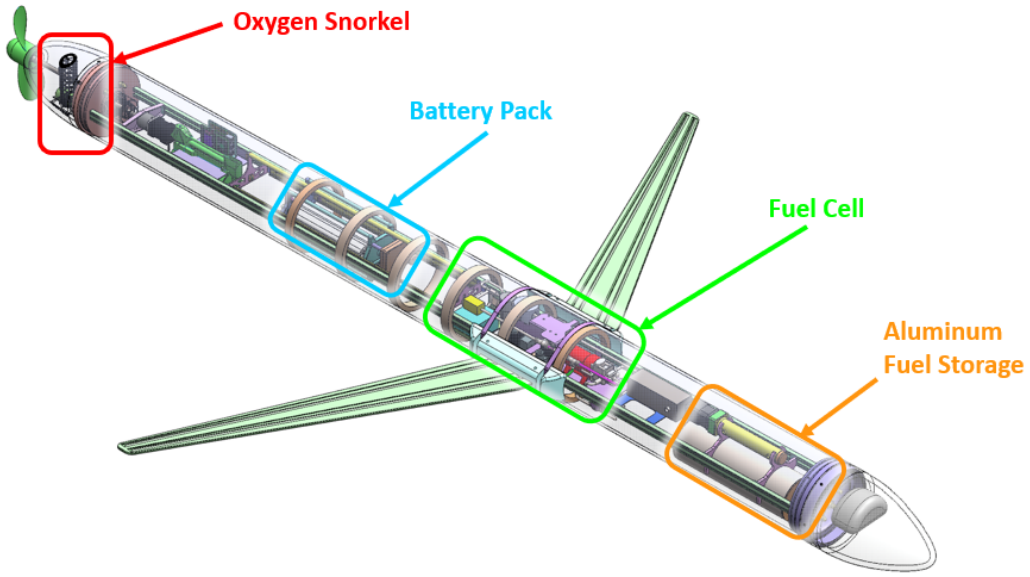

Figure 1: **Energy system location on DOUG.** Solar panels are located on the top surface of the vehicle and fins (not shown). The fuel cell is located at the forward end, while the battery pack is used for weight shift control. Aluminum is stored in the forward fairing, while the oxygen snorkel is located in the aft fairing.

2.1 Energy system requirements

The vehicle is required to operate for a minimum of 30 days. This endurance requirement is the primary driver of the energy system design. A summary of system requirements is documented in Table 2.

Requirement	Value	Reasoning
Mission Length	30 days	Sponsor Requirement
Maximum External Pressure	10 MPa	Sponsors require 1000m depth
Minimum Ambient Temperature	0-10° C	Sponsors require 1000m depth
Maximum Burst Speed	2 knots	(1 m/s). Required by sponsor
Total Vehicle Weight	80 kg	Enables 2-person deployment
Total Vehicle Cost	$50k	Achieve lower cost than RAPID

Table 2: **Energy system requirements.**

Versatility of the vehicle operation is an additional, soft requirement. Using the concept of *Idea on Monday, Deployment on Wednesday*, the design is able to accommodate changes in the mission profile. The design is functional for a range of dive times and payloads. For added flexibility, the battery pack is large enough to allow the vehicle to "park" at depth for up to 12 hours during a storm.

Energy-system specific requirements are derived from the mission profile shown in Figure 2. Power requirements are listed in Tables 3-5.

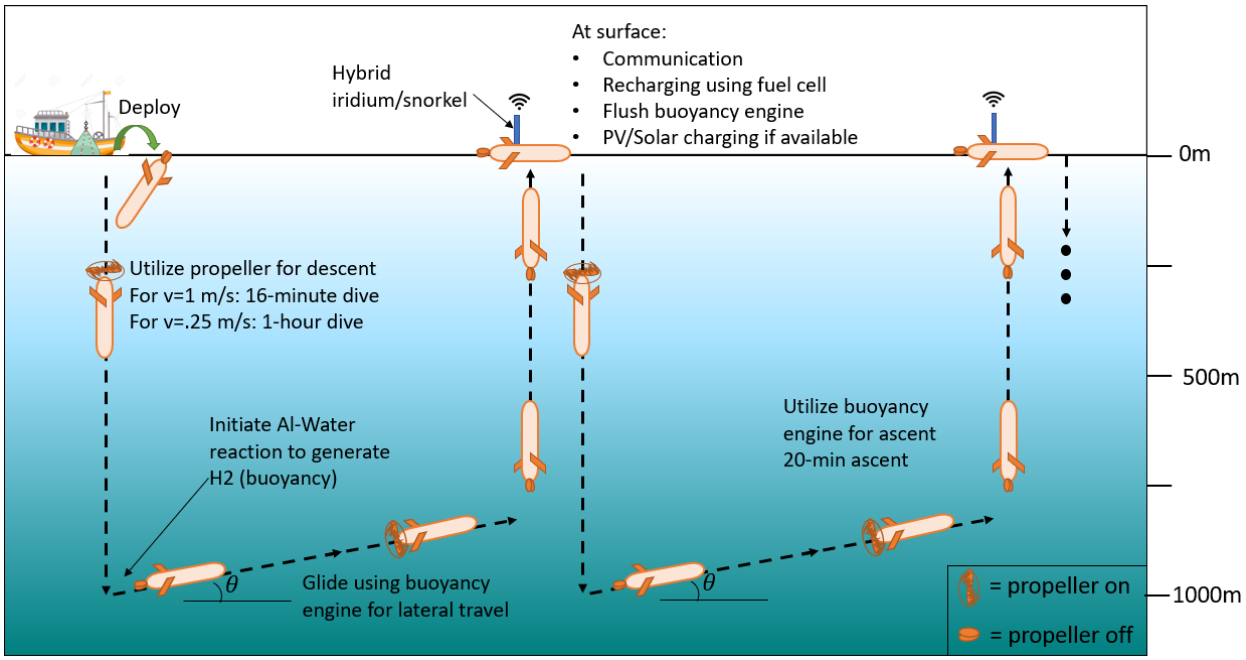

Figure 2: **Energy mission profile.** Generic mission profile used for energy calculations. Target 8 dives per day (3 hours each) for 30 days.

The dive cycle chosen for the energy requirement calculation is a 3-hour dive cycle. This cycle time meets several system requirements. A descent speed of .25 m/s is appropriate to allow high resolution sampling, which results in a 1-hour descent. The energy storage estimated for the mission accounts for use of a propeller to propel the vehicle at the maximum required speed (1 m/s) about 10% of the time in the event that currents are strong. A descent at maximum speed would result in a descent time of approximately 16 minutes.

The ascent time is about 20 minutes, and is derived from the buoyancy engine characteristics. See Section 3.3.2 for details. The dive cycle described by Figure 2 requires approximately 1 hour of charging time, leaving approximately 30 minutes at depth for a 3-hour dive cycle. For 30-days, it is estimated that the vehicle will make 240 dives.

The power requirements listed in the following tables are categorized as follows:

- Payload (on during dives)
    - Propulsion via Propeller
    - Data acquisition via hydrophone
- Hotel Load: minimum consistent power
- Surface energy requirements

Component	Nominal Power Req. (W)	Voltage (V)
IMU	0.014	3.7
Clock	0.002	3.3
Controller	2.5	5
Hydrophone (Acoustic Positioning)	2.4	12

Table 3: **Hotel load power requirements.**

Component	Nominal Power Req. (W)	Voltage (V)
Propulsion (Propeller Motor)	Burst Speed, 1 m/s: 44 Dive Speed, 0.25 m/s: 2.75 Cruise Speed, 0.1 m/s: 0.38	24
Data Acquisition (CTD)	0.286	12

Table 4: **Payload power requirements.**

Component	Nominal Power Req. (W)	Voltage (V)
GPS	0.102	3.3
Iridium	0.17	5
Snorkel system	2.77	12
Hydrogen fuel cell controller	N/A	Purging Valve: 6V Blower: 5V
Aluminum fuel system	18W	24V
Plumbing operation (valves and seawater pump)	Pump: 4 Solenoid Valves: 18 (each)	Pump: 12 Solenoid Valves: 12

Table 5: **Surface operation power requirements.**

Based on the assumptions listed above, and accounting for efficiency and losses, a 3-hour dive cycle requires 29 Wh of energy. **For 240 dives, the energy storage requirement is 6.96 kWh per mission.**

It is likely that not every dive will be the same. Versatility is a key attribute of the system. For this reason, the NiMH battery pack is oversized at 240 Wh. The additional energy storage allows variation in the dive profile, in the event that the propeller is used for propulsion for a greater amount of time than expected, or if the vehicle is parked at depth for a longer period of time. If the battery pack is depleted, it can be recharged by an additional aluminum-water reaction, or by supplementary energy from the PV array.

The fuel cell system is designed for a 3-hour dive, but can easily operate at a different design point. Based on the "Idea on Monday, Deploy on Wednesday" ideology, Figure 3 shows energy requirements for a range of dive cycle times, given the power requirements listed in Tables 3-5.

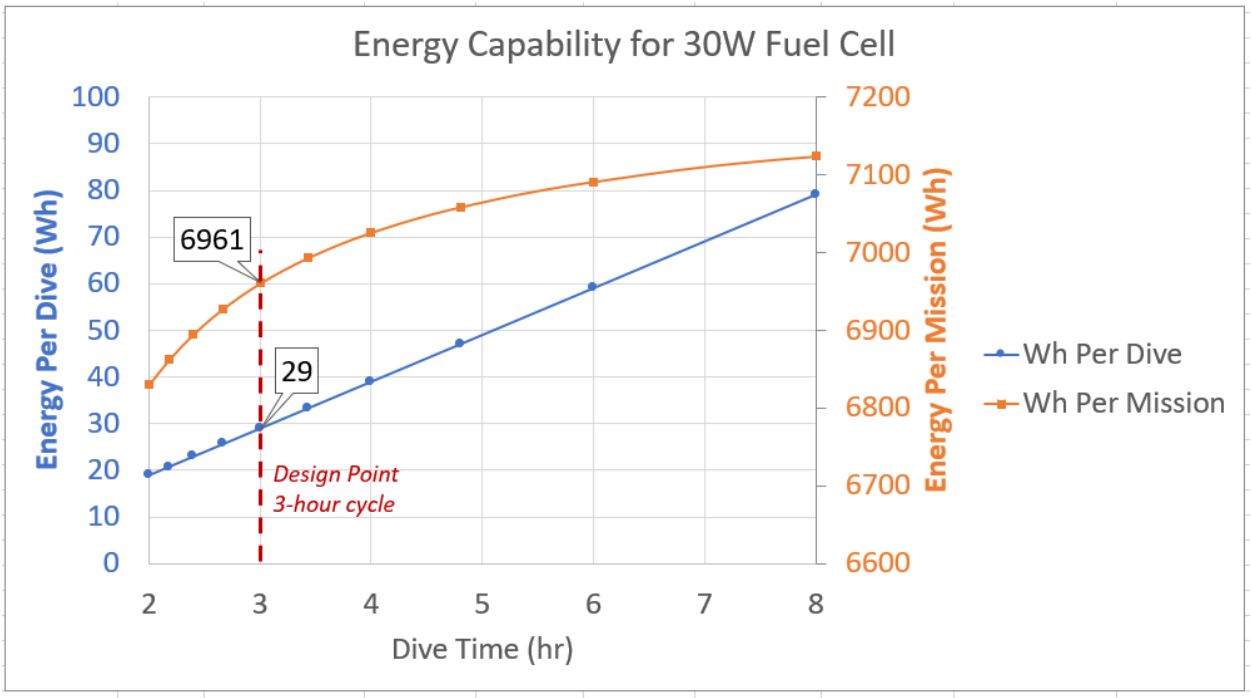

Figure 3: **Energy requirements vs dive time.** For reference, longer dives result in greater mission energy requirements. The design point of a 3-hour dive is shown.

2.2 Energy system overview[1]

The primary energy source for DOUG is a 30W hydrogen PEM fuel cell. The fuel is stored in the form of aluminum powder, suspended in oil at 60% concentration by volume. At depth, the aluminum-water reaction is initiated to generate the hydrogen needed to power the next dive cycle. This hydrogen acts as a buoyancy engine by expanding an external bladder until the vehicle reaches the surface. The hydrogen is then consumed in the fuel cell and converted into electricity and used to charge the battery pack.

At the surface, a snorkel is deployed, and an air vent is opened to create an air-breathing hull. With a continuous supply of air, the fuel cell is able to operate and charge the battery pack. If the sun is out during daytime operation, PV cells on the surface of the vehicle will assist in battery charging at a rate of 6.2W. Before the next dive begins, a pump is used to flush the buoyancy engine with seawater to prevent excessive buildup of the reaction byproduct which could impede the reaction performance. Reference Section 3.3 for a detailed description of buoyancy engine design and operation.

As shown in Tables 3-5, there is a range of voltage requirements for various system components. The electrical system, including voltage regulators, are shown in Figure 4.

[1] Sharkh, S., and Griffiths, G., 2003, “Energy Storage Systems for Unmanned Underwater Vehicles,” Underwater Technology, **25**, pp. 143–148.

Component	Weight (kg)	Volume (L)	Cost (USD)
Hydrogen fuel cell	0.37	0.28	366
Plumbing	2.85	10.9	1,187
Aluminum fuel	5.8	2.9	400
Snorkel system	.5	.5	350
Battery pack	5	2	100
PV system	.05	.140	250
Electrical components	.15	.12	90
Total	**14.7**	**14.7**	**$2,743**
% of Budget	**18.4% of 80kg**	**18.4% of 80L**	**5.5% of $50k**

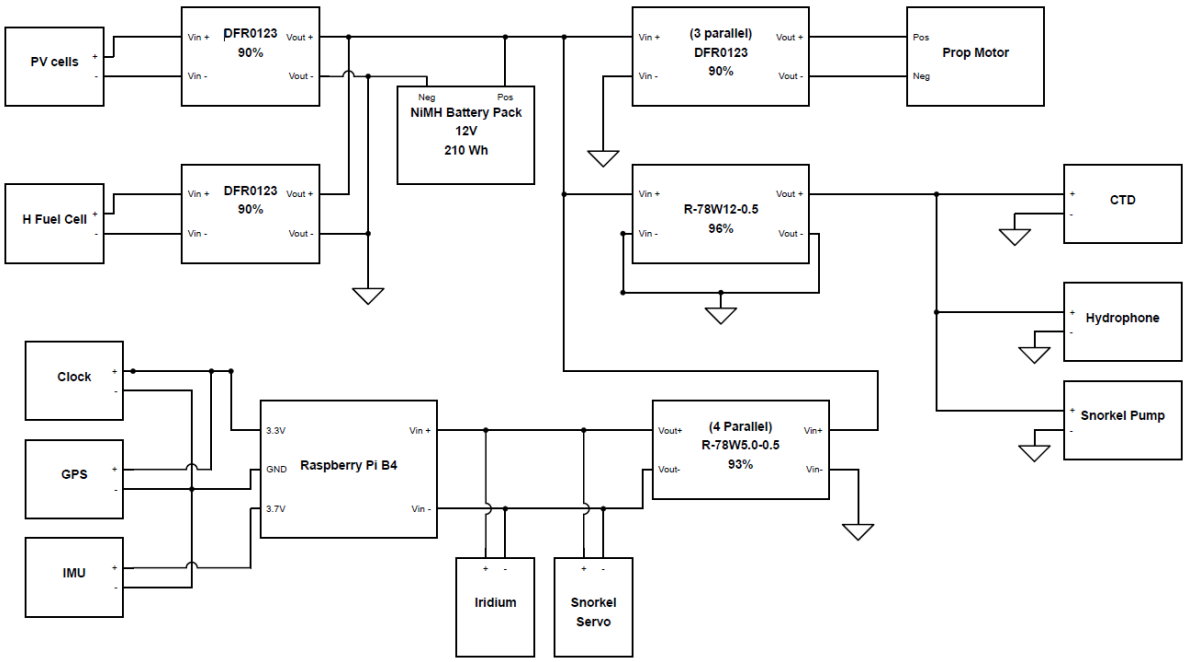

Figure 4: **Electrical diagram.** Schematic of Electrical System, including the DC-DC converters to regulate the voltages. Multiple converters in parallel are represented as single components.

Table 6: **System weight and cost breakdown.**

2.3 Battery pack

A significant factor in the development of our unmanned underwater vehicle (UUV) is storing the energy required for a 30 day mission, in conjunction with fuel cell and solar charging between dives. To do so, batteries will be used. Batteries are a well-defined technology commonly found in UUVs that will allow us to safely power all onboard propulsion systems and electronics while operating up to 1000m deep in the ocean. Consistent trends between battery types allow us to choose Nickel Metal Hydride (NiMH) as the logical choice for energy storage aboard our UUV. The following analysis details these trends and concludes with a look at NiMH and potential issues we may encounter when operating our power system.

2.3.1 Battery selection

Several different battery chemistries exist on the market today, with power density being a valuable comparison parameter. Lithium-based batteries clearly outperform their counterparts in terms of both gravimetric and volumetric power densities and will be used for comparison's sake in this report. However they pose a significant safety risk due to a tendency to explode and are therefore not being considered for this UUV. Typical UUVs use either Li-ion or, if safety is a concern, NiMH, so there is significant precedent for using this battery type in an underwater vehicle application. NiMH has higher power densities than lead acid or NiCd batteries and has a life cycle much greater than rechargeable alkaline (whose life cycle ~ 1-10 charges, with a significant drop in capacity after a single use).

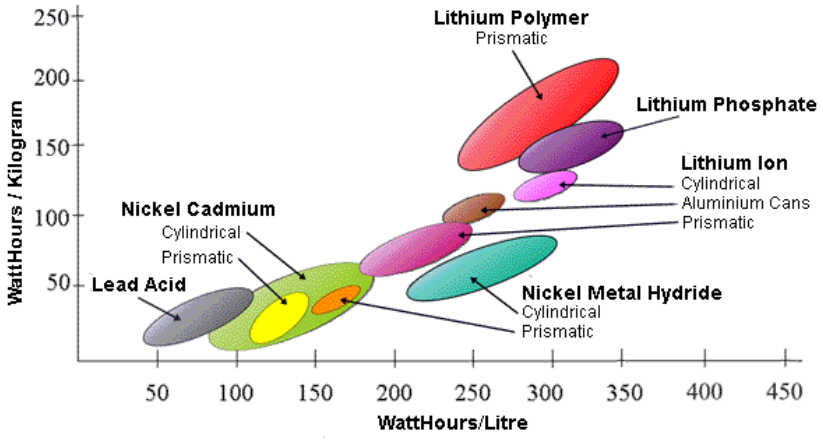

Figure 5: **Battery energy density comparison.** Common battery chemistries compared via volumetric and gravimetric power density ranges.[7]

It is beneficial to use rechargeable (secondary) batteries in our system instead of primary batteries because carrying the energy for the entire 30 day mission in batteries would put us over the 100kg weight limit (or be a substantial portion of the weight if mission energy consumption is closer to 7 kWh). Therefore, some form of power generation (solar panels, hydrogen fuel cells, etc.) is necessary and will interface well with rechargeable NiMH batteries. Overall, NiMH batteries offer a cheap, abundant, energy dense, easy-to-use energy storage method for our UUV.

2.3.2 Battery pack architecture

Specifically chosen was the Energizer AA NiMH battery, whose properties are listed in Figure 6 below.

Current Storage	2.5 Ah	Recharge capability	~10^2
Voltage	1.25 V	Self discharge rate	50-80% @ 12 months
Weight	30 g	Capacity at 0 °C	80%
Lifetime	2-5 years	Cost	~$5 per battery

Figure 6: **Battery Characteristics.** Essential battery metrics for designing an UUV energy system.

In the expected environment this battery will maintain the general shape of the 1.2 V profile, with actual (dischargeable) capacity predicted to be ~80% of rated capacity

due to ambient temperatures around 0 °C. Charging dynamics are not significantly affected by temperature. Voltage depression, aka “memory”, is not an issue with the latest version of Energizer’s NiMH batteries. Furthermore small pressure variations from atmospheric conditions do not noticeably affect battery performance, although the hull design will limit these pressure fluctuations and therefore pressure is not a concern for this subsystem.

The battery pack will be assembled out of many Energizer AA batteries in an architecture shown in Figure 7. In total it is a 12 V, 240 Wh pack (80 batteries). A 3D printed plastic casing with copper embedded will hold and connect all the batteries (not shown below), and integrate with the weight-shifting mechanism onboard.

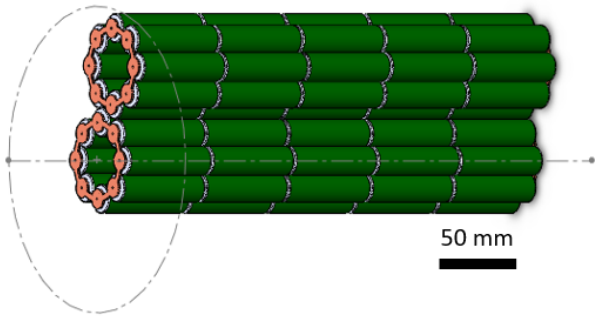

Figure 7: **Battery Assembly.** Batteries are assembled into cylinders, connected via copper cutouts and designed to fit into the weight-shifting apparatus onboard. The sketched circle has a diameter of 6 inches, allowing for room between the batteries and the hull. Also, the circle shows the path of the batteries as they are rotated via the weight shifting mechanism. This off-center center of mass is essential for the operation of the vehicle as it allows for shifting the vehicle’s COM port or starboard with one rotational input.

2.4 Hydrogen fuel cell

2.4.1 Primary energy system selection

Nickel-Metal Hydride batteries have an energy density of approximately 60 Wh/kg. If batteries were chosen as the primary energy system, a 7-kWh mission would require 116 kg of batteries. A battery pack of this size would far exceed the mass target of 80kg for the entire vehicle. For this reason, the team evaluated several fuel storage options as a primary energy system, which is used to charge a 240 Wh battery pack.

A PEM hydrogen fuel cell was chosen as the primary energy system, with aluminum fuel storage. Alternative design choices are summarized in the decision tree, Figure 8.

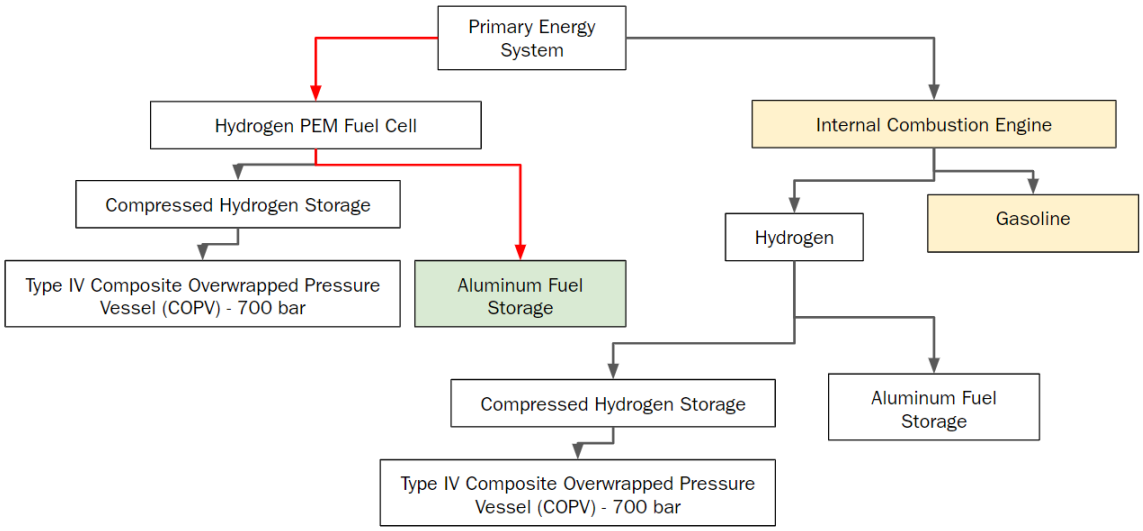

Figure 8: **Decision tree for primary energy system.** The hydrogen fuel cell with aluminum fuel storage was chosen for its low size and weight requirements, although it is the highest risk system.

The hydrogen fuel cell is preferable to an internal combustion engine because there are no carbon emissions, and it operates with less noise and less heat generation. In addition, initial estimates revealed that the internal combustion engine would likely be larger in both size and weight, and comparable in cost. The hydrogen fuel cell system carries risk due to the limited experience with fuel cells on UUVs, especially those powered by aluminum. Although the hydrogen fuel cell is the higher risk option, it was chosen for this design because of the weight and cost advantages, in addition to providing an innovation opportunity in the UUV industry.

The downside to fuel cell energy conversion is the complexity involved in hydrogen storage. The options for hydrogen storage are compressed gas tanks or aluminum storage. High-pressure Composite Overwrapped Pressure Vessels (COPVs) exist for hydrogen storage up to 70 MPa, and are used on fuel-cell powered automobiles. Due to the size and weight of these gas tanks, they would be suited for a larger system as they are expensive and heavy. For this reason, aluminum fuel storage was chosen.

2.4.2 Fuel storage requirements

Aluminum fuel is an experimental option for storage of hydrogen fuel. The aluminum fuel is stored onboard the vehicle, and reacted in small amounts with an excess of seawater to generate hydrogen. The aluminum-water reaction is shown in Equations (1) and (2). [2] [3]

$$2Al + 4H_2O \rightarrow 3H_2 + 2AlOOH \quad (1)$$
$$2Al + 6H_2O \rightarrow 3H_2 + 2Al(OH)_3 \quad (2)$$

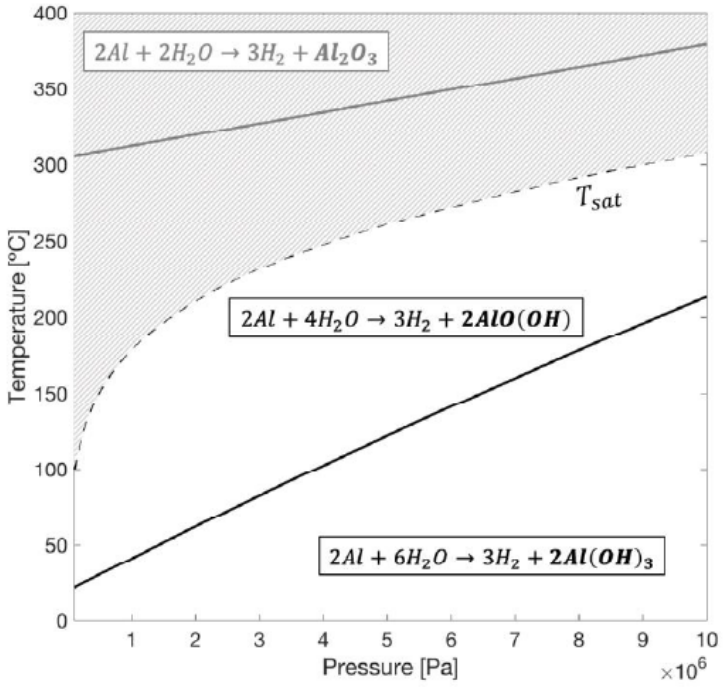

Figure 9: **Aluminum-water reaction transition diagram.** In 5°C water, at 1000m depth, the reaction is likely to produce aluminum hydroxide rather than aluminum oxyhydroxide.[4]

The energy density of aluminum fuel is 8.61 Wh/g, 50% of which is converted to chemical energy during the aluminum-water reaction. For a fuel cell efficiency of 40%, the usable energy density of the aluminum fuel is 1.722 Wh/g-Al. Thus, a 29-Wh dive cycle requires 16.84g of aluminum fuel.

---

[2] Fischman, J. Z., 2019, "The Development and Characterization of Aluminum Fueled Power Systems and a Liquid Aluminum Fuel," Thesis, Massachusetts Institute of Technology.

[3] "The Development and Characterization of Aluminum Fueled Power Systems and a Liquid Aluminum Fuel."

[4] Fischman, J. Z., 2019, "The Development and Characterization of Aluminum Fueled Power Systems and a Liquid Aluminum Fuel," Thesis, Massachusetts Institute of Technology.

As described in later sections, additional hydrogen is required in order to achieve a high enough pressure differential to maintain flow into the fuel cell. For this reason, 20g of aluminum is reacted per dive. **For 240 dives, 4.8kg of aluminum storage is required.**

Using the Equations (1) and (2), each aluminum reaction generates 2.22g of hydrogen per dive. Based on aluminum-water reaction experiments, ~6x water is required to reliably react the aluminum. Based on Equation (1), at least 160g of water is required per dive. See Section 3.3.2 for further details of the aluminum reaction properties.

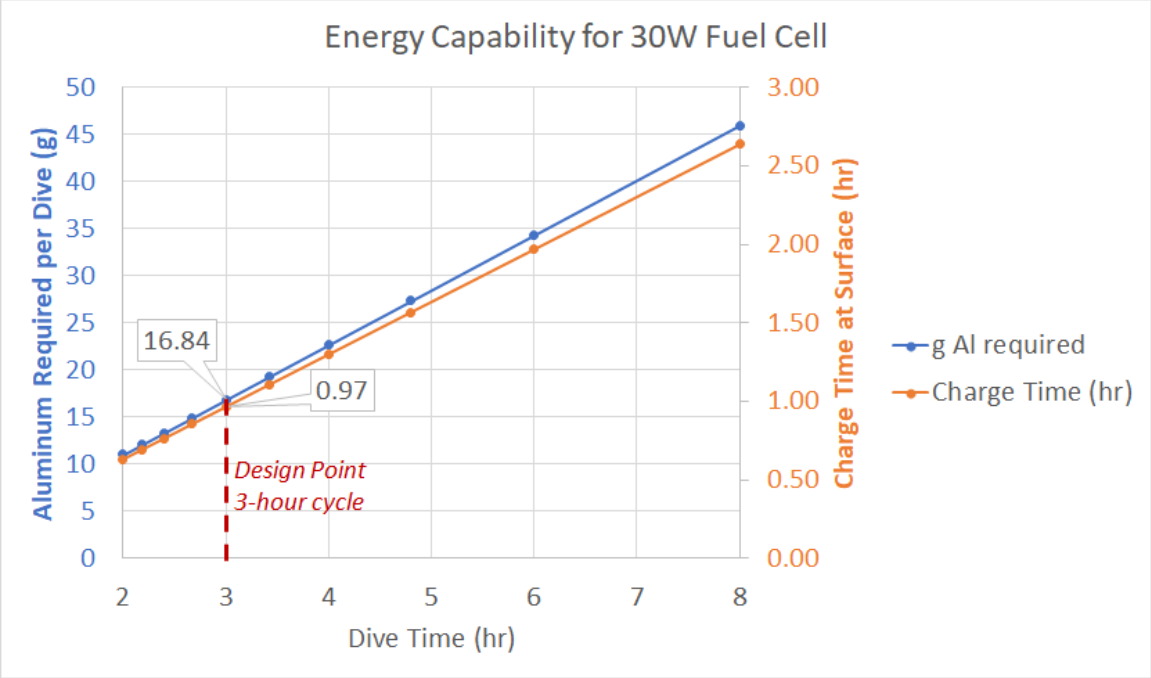

Figure 10: **Aluminum fuel and fuel cell charging time requirements per dive.** For the 3-hour dive cycle, about 15g of aluminum is required per dive. The fuel cell must charge for approximately 1 hour on the surface.

2.4.3 Hydrogen fuel cell architecture

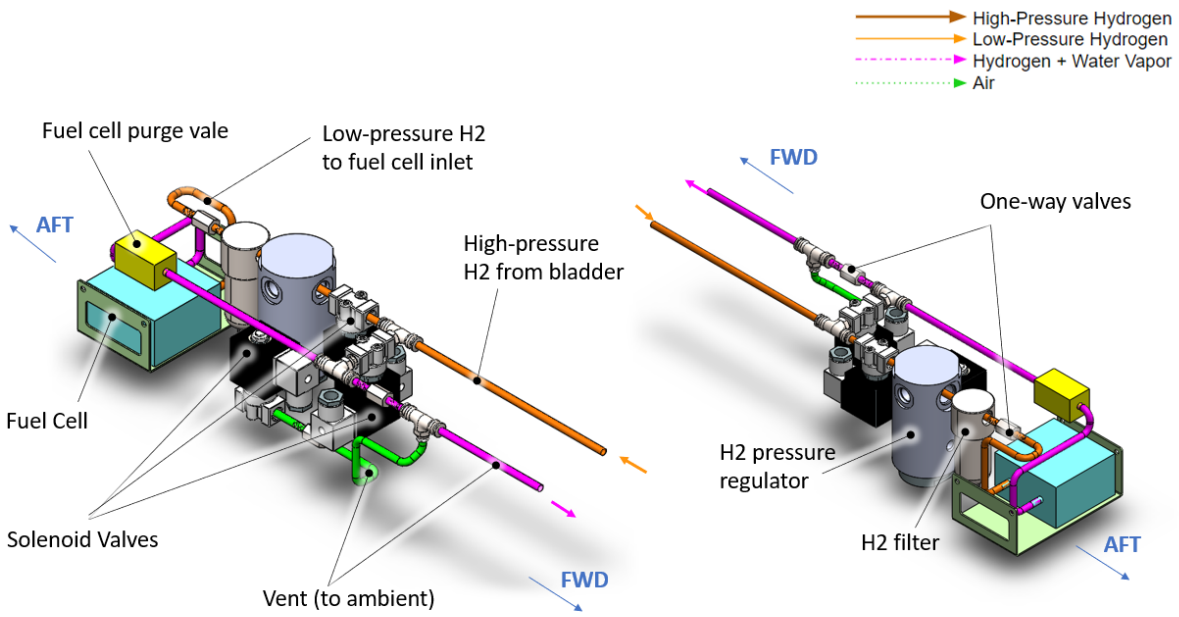

Figure 11: **Fuel cell architecture and plumbing.**

The fuel cell chosen for DOUG is a Horizon H-30 fuel cell, which operates at 30W. The 30W size is suitable to both minimize fuel cell mass and cost, without requiring excessive charging time. The fuel cell system is shown in Figure 11, with a 2D schematic shown in Figure 13.

Hydrogen from the bladder will enter the pressure hull via steel tubing at approximately 5 MPa. As shown in the specifications in Figure 14, the fuel cell operates at 145-155 kPa (absolute), A TESCOM 20-1200 series with a steel body is used for regulating the incoming hydrogen. The steel body version of the pressure regulator can handle an inlet pressure up to 70.2 MPa and therefore is sufficient to handle the pressure required for this application. The flow of hydrogen from the bladder to the fuel cell is dependent on the pressure in the bladder. The fuel cell operates at 0.15 MPa, therefore hydrogen flow occurs when bladder pressure exceeds 0.15 MPa. Figure 12 shows the change in bladder pressure as hydrogen is consumed by the fuel cell. The pressure in the bladder falls below 0.15 MPa with <0.1g of hydrogen left over, therefore <0.1g of hydrogen is wasted per dive cycle. This additional hydrogen also keeps the vehicle positively buoyant during battery charging, which allows the PV array to operate for the entirety of the charging process.

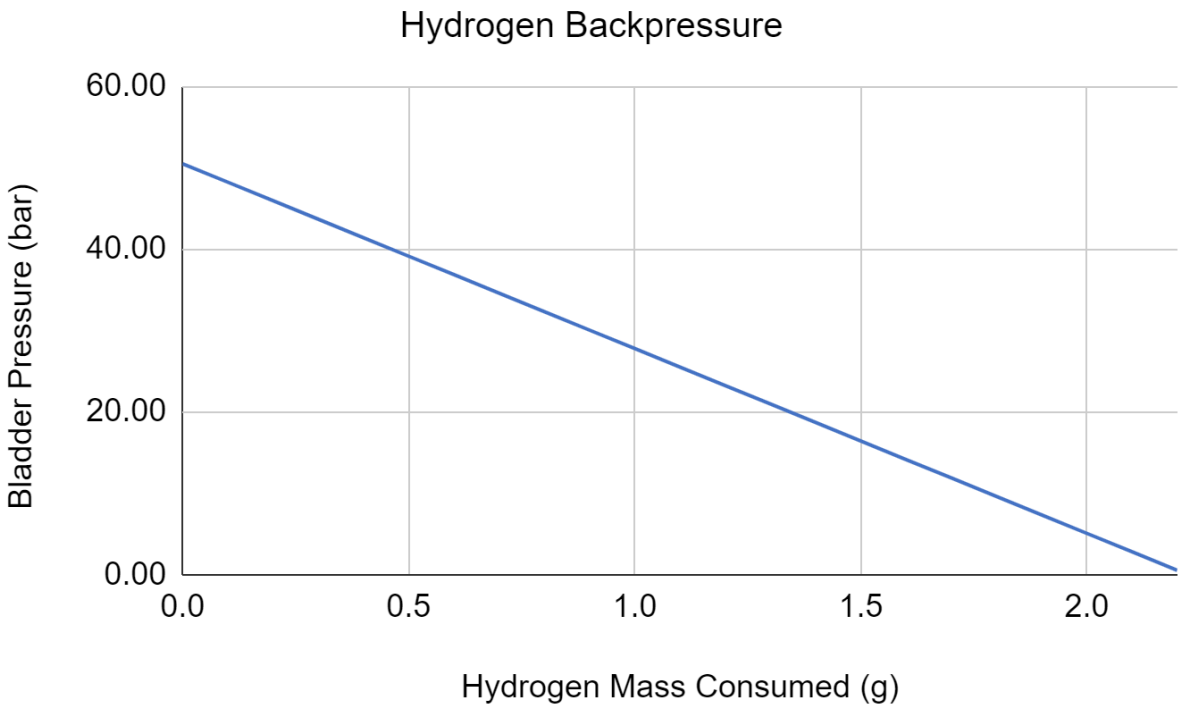

Figure 12: **Bladder pressure versus hydrogen consumption.** The bladder falls below 0.15 MPa with <0.1g of hydrogen left over.

The fuel cell also requires hydrogen gas to be at 99.995% purity or higher. The hydrogen gas must be dry, with no water in the vapor. While the H-30 fuel cell comes with a purifier, the specs of this purifier are unknown. To reduce risk in the system design, the team specified a Parker 0.3-Micron stainless steel particulate filter, model PF501. According to specifications, this filter can remove solid particulates from the gas as well as any liquid droplets (water or oil) which may enter the hydrogen line from the bladder. This filter can not separate air, however. The bladder flushing system is designed such that air is not introduced into the bladder. This can be done by flushing the system after all hydrogen has been reacted and is emptied from the bladder. At this state, the system is neutrally buoyant and will be submerged under the water. At this time, the bladder can be flushed from inlets at the bottom of the vehicle to avoid the risk of air bubbles entering the bladder. This particle filter can accommodate pressures up to 2.07 MPa, therefore should be placed downstream of the pressure regulator. [5]

The fuel cell outlet consists of a mixture of hydrogen and water vapor. An orifice may be used at the outlet, as shown in Figure 13, to increase the backpressure on the outlet

[5] “Parker - 1/4" Port, 4" High x 1.56" Wide, FRL Filter with Stainless Steel Bowl & Manual Drain - 60314754 - MSC Industrial Supply” [Online]. Available: https://www.mscdirect.com/product/details/60314754?fromRR=Y.

and reduce the amount of hydrogen passing through the cell. This system must be tested before use. For simplicity of the system and to reduce cost and weight, the team chose to vent the fuel cell products. This vent line, as shown in fuschia in Figures 11 and 13, is coupled with the air vent line. This combined gas vent exits the pressure hull through the forward end cap, and exits the nose fairing through the top surface of the vehicle.

The design could be improved by making use of these products, at the expense of cost and weight. A condenser can be added to the system on the outlet side of the fuel cell in order to separate the water vapor from the hydrogen. The hydrogen can be recycled in the fuel cell, and the water can either be ballasted or used for trimming.

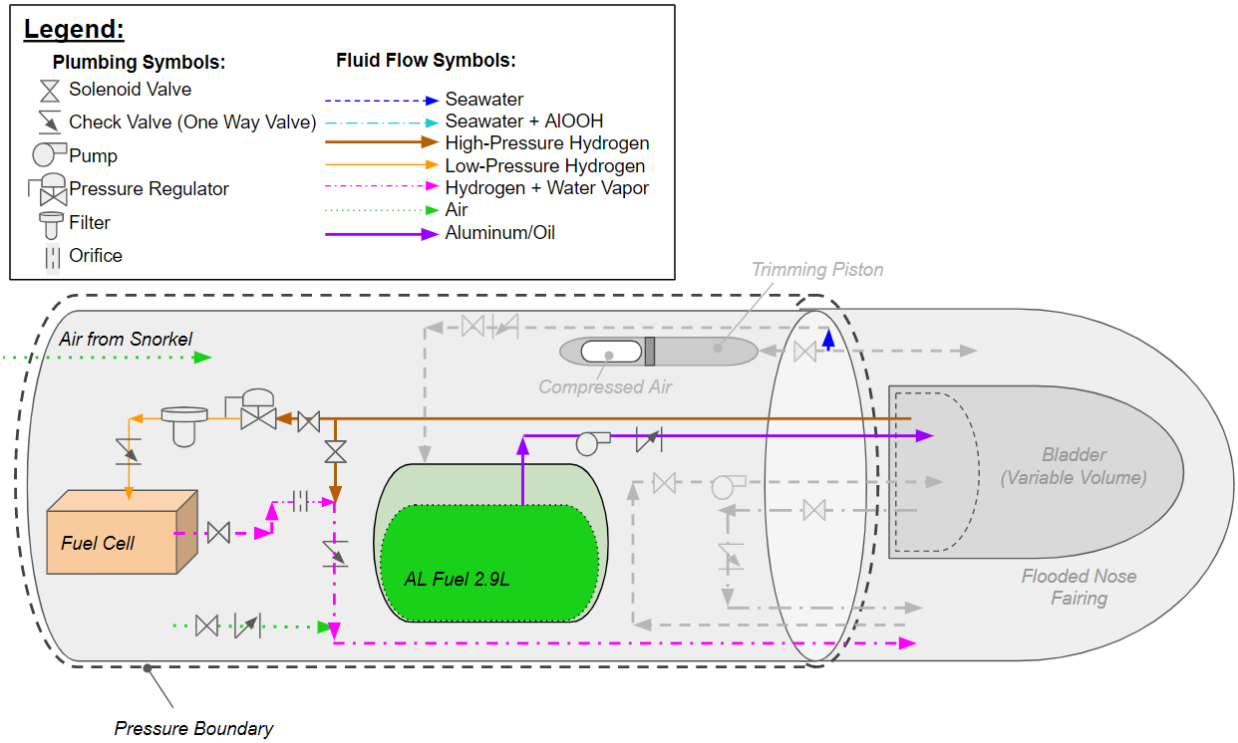

Figure 13: **Fuel cell plumbing schematic.** Gray arrows represent buoyancy engine components, defined in Section 3.3.

Type of fuel cell	PEM
Number of cells	14
Rated Power	30W
Performance	8.4V @ 3.6A
Purging valve voltage	6V
Blower voltage	5V
Reactants	Hydrogen and Air
External temperature	5 to 30ºC
Max stack temperature	55ºC
H2 Pressure	0.45-0.55bar
Hydrogen purity	≧99.995％ dry H2
Humidification	self-humidified
Cooling	Air (integrated cooling fan)
Weight (with fan & casing)	280grams(±30 grams)
Controller	90 grams(±10 grams)
Dimension	8cmX4.7cmX7.5cm
Flow rate at max output*	0.42 L/min
Start up time	≦30S at ambient temperature
Efficiency of stack	40% @ at full power

Figure 14: **Hydrogen PEM fuel cell specifications**[6]**.** The fuel cell requires hydrogen at 0.45-0.55 bar (0.045-0.055 MPa) gage, with 99.995% purity.

The hydrogen PEM fuel cell generates electricity via a electrochemical reaction, as shown in Equation (3)

$$H_2 + \frac{1}{2}O_2 \rightarrow H_2O \tag{3}$$

The reaction of 20g of aluminum, results in 2.22g of hydrogen gas per dive cycle. From Equation (3) it is determined that 17.8g of oxygen is required per dive. According to the hydrogen fuel cell specifications, the inlet flow rate of hydrogen is 0.42 L/min at maximum power. At 0.15 MPa, the hydrogen flow rate is 0.027 moles/min. From Equation (3), 0.013 moles/min of oxygen is required. Since air enters the fuel cell through the ambient air, the volume flow rate of oxygen is 0.304 L/min at 0.1 MPa. Air makes up 20.95% of air by volume, therefore the minimum flowrate of air required to operate the fuel cell is 1.45 L/min.

Because of the large quantity of oxygen required to run the fuel cell, onboard oxygen storage is unfeasible for our design target. Instead, a snorkel is used at the surface, along with an air vent, to circulate air through the pressure hull at a rate of 2 L/min. This

[6] “AIR COOLED STACKS | HORIZON FUEL CELL TECHNOLOGIES,” duplicated [Online]. Available: https://www.horizonfuelcell.com/hseries.

airflow supplies oxygen to the fuel cell while providing a continuous supply of cooling air. The snorkel design is detailed in the following section.

2.5 Snorkel

To operate the fuel cell at full capacity, air must be supplied at a minimum flow rate of 1.45 L/min. Ensuring we have a reliable flow of air to the fuel cell is critical for long-term operation of the vehicle. To minimize system weight, volume, and complexity, we down-selected from an array of air-supply and air-storage designs and honed in on a telescoping snorkel that supplies air to the fuel cell during a resurface.

2.5.1 Snorkel construction

The telescoping snorkel actuates up and down perpendicular to the hull using a simple pulley-motor system. The snorkel serves two key functions: (1) bring the air tube above the water and wave surface to funnel air into the fuel cell and (2) bring the antenna to an appropriate height for data transmission. The soft system requirement imposed by these two functions is to have the snorkel actuate up to 12” above the water. With the proposed construction of the snorkel, both the air tube and the antenna can achieve a height of up to 14”.

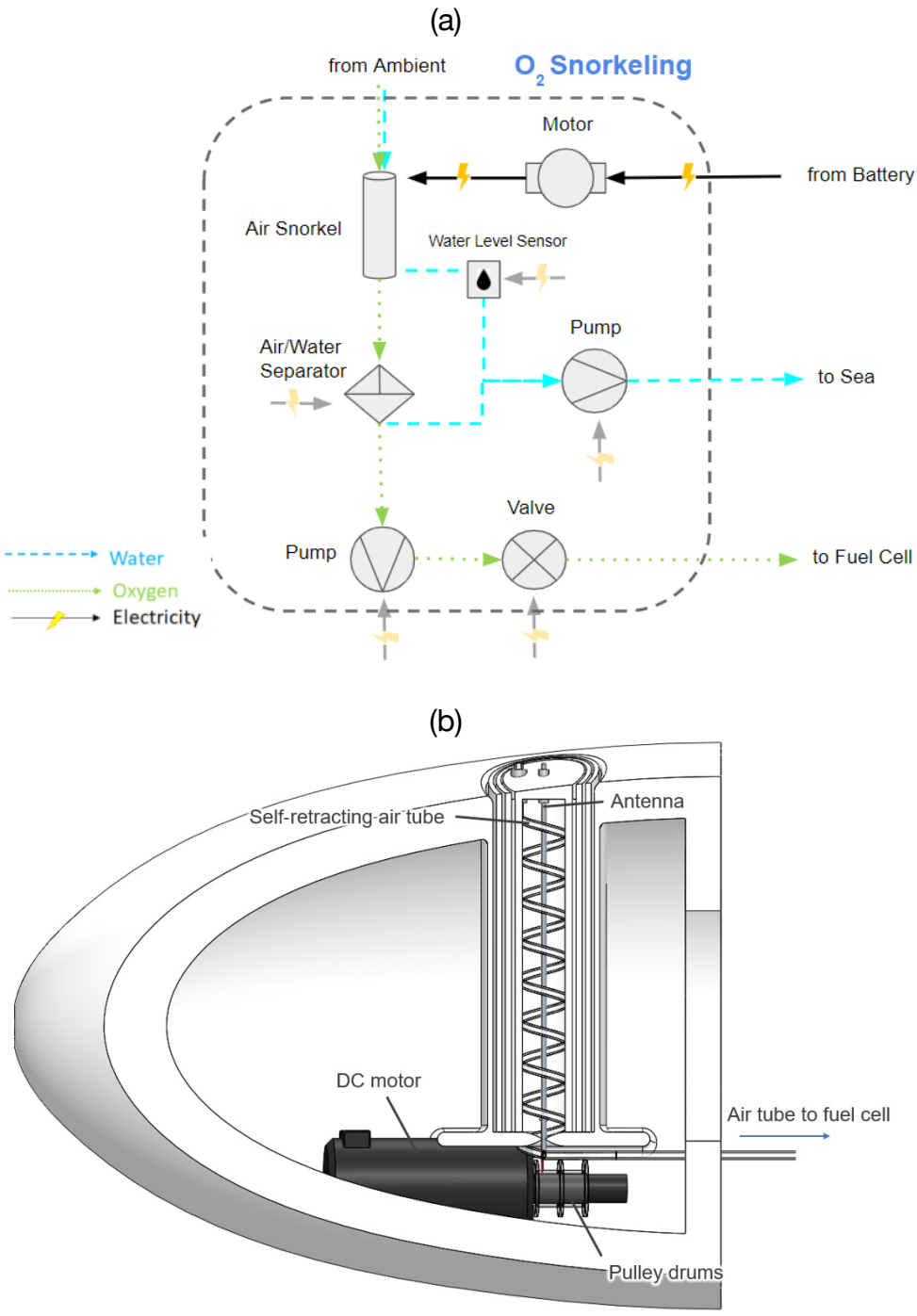

Figure 15: **Snorkel construction.** (a) System diagram of the snorkel energy flow and (b) CAD of the snorkel is integrated directly into the 3D printed rear fairing.

The snorkel is 3D printed using ABS filament (which is stronger and more resilient than PLA) and it is designed to be nested within the flooded rear fairing of the UUV. To improve the reliability of the snorkel, a high spacing value between nested tubes of 0.08” is set to ensure they do not jam. The inner diameter of the innermost tube is 1” to give space for the 0.07” ID self-retracting polyurethane air tube (with coil 0.75” OD) and the antenna, shown in Figure 15 (b). There is a valve at the tip of the air tube which opens only when the snorkel is actuated up to minimize water intake; wires for the valve can be directed down the air tube. In case of any water intake, an air-water separator is installed before the air pump which drains any excess water out to the sea. For improved reliability, a water sensor can be installed to pump out large volumes of water from the tube, however, this is likely redundant given the valve installed at the tip of the air tube. Air is then pumped from ambient, through the snorkel and air-water separator into the fuel cell, shown in Figure 15 (a). The pump used to funnel the air from ambient to the fuel cell is rated at 2.0 L/min to meet the system requirement of supplying air to the fuel cell at 1.45 L/min.

2.5.2 Snorkel actuation

For the snorkel to achieve a height of 12” above the water level, it actuates vertically and perpendicular to the hull when the UUV is resurfaced. A soft requirement of the snorkel system is imposed to minimize the volume taken up by the snorkel construction such that it can fit in the rear fairing along with the actuation motor and the propeller. Therefore, to balance the maximizing height requirement and minimizing volume requirement, the snorkel tube is split into four constituent tubes, three of which actuate and one of which is fixed to the fairing. Additionally, minimizing the number of consitutnet tubes improves reliability by reducing the number of moving pieces and the amount of friction endured by the pulley.

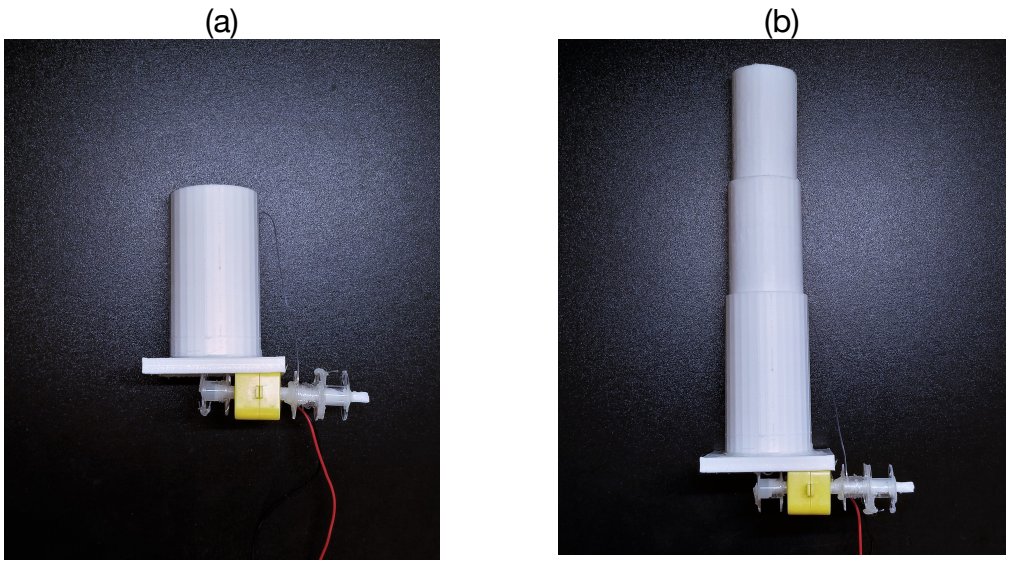

Figure 16: **Snorkel actuation.** (a) Unactuated state of the snorkel and (b) actuated state of the snorkel. The prototype is to-scale in the width dimension and ⅗-scale in the height dimension. The tubes are 3D printed with PLA filament and are actuated via a 10 lb load bearing fishing line pulley tethered to a DC motor.

Thus, constituent tubes are designed to be 5” in height (with 1” innermost diameter, 0.13” wall thickness, 0.08” tolerance between tubes) meaning that when they are unactuated, the tubes only take up 5” in the vertical direction and when actuated they can achieve a maximum height of 14” (5” for each actuated tube minus 1” for the pulley holes), shown in Figure 17 on the following page.

2.5.3 Pulley threading

To provide clarity on how the pulley is threaded in this telescoping snorkel design, Figure 17 shows the threading process of the pulley within the nested tubes.

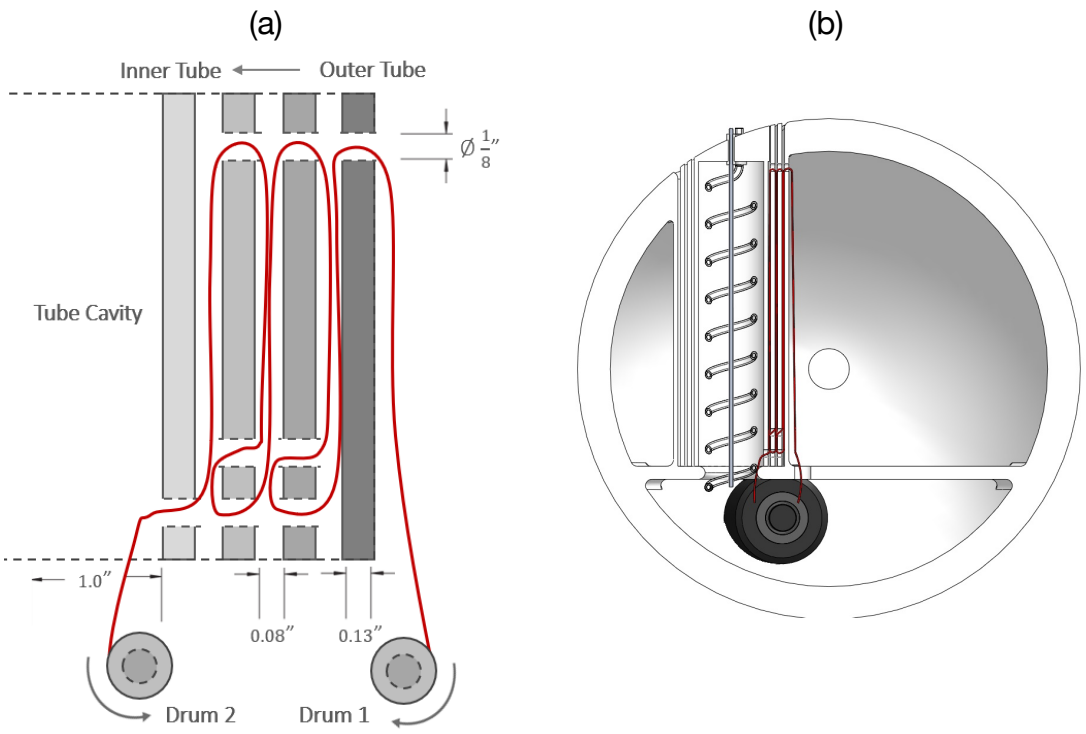

Figure 17: **Pulley threading schematic.** (a) Detailed cross-section of the pulley threading schematic with dimensions and (b) CAD cross-section of the pulley threading schematic where the red line is the pulley. The pulley is threaded through holes within each tube and then tethered to drums affixed to the motor. The pulley is tethered to each drum in opposite directions such that when the motor runs in the forward bias, the tubes actuate up and when the motor runs in the reverse bias, the tubes actuate down.

From trial and error with the functional prototype shown in Figure 17, an ideal pulley for this construction is a thin, high-load bearing fishing line. A high tension is applied to pulley if the motor over actuates the drums in either direction as well as when the pulley experiences too much friction between pipes. To ensure that the pulley does not snap, a high-load bearing (10 lb) fishing line is used; using a fishing line as the pulley also ensures that it is thin enough to clear the tolerance between pipes which helps to minimize friction.

2.5.4 Other snorkel designs and challenges

Other designs, such as a 90° actuated snorkel and an on-board air storage bladder , were conceptualized but were too difficult to implement to the existing architecture. For example, the 90° actuated snorkel had too complex of a mechanism located at its pivot point which introduced challenges in properly sealing the hull where the snorkel

protruded. Additionally, the on-board air storage bladder was our first idea for an air-supply system but would introduce unnecessary volume restrictions to the hull and logistical concerns regarding implementation, similar to on-board water storage; since the UUV will be resurfacing, air is accessible and the storage of air for the entire 30-day mission is redundant.

2.6 PV array

2.6.1 PV array geometry

To meet the required mission energy of 7 kWh or 29 Wh per dive, a flexible photovoltaic (PV) array is installed on the hull of the UUV. During the mission cycle of the UUV, it is continuously resurfacing to snorkel air and transmit data, therefore, there is an opportunity to harvest light as a means to reduce the amount of stored aluminum fuel required to meet the mission energy

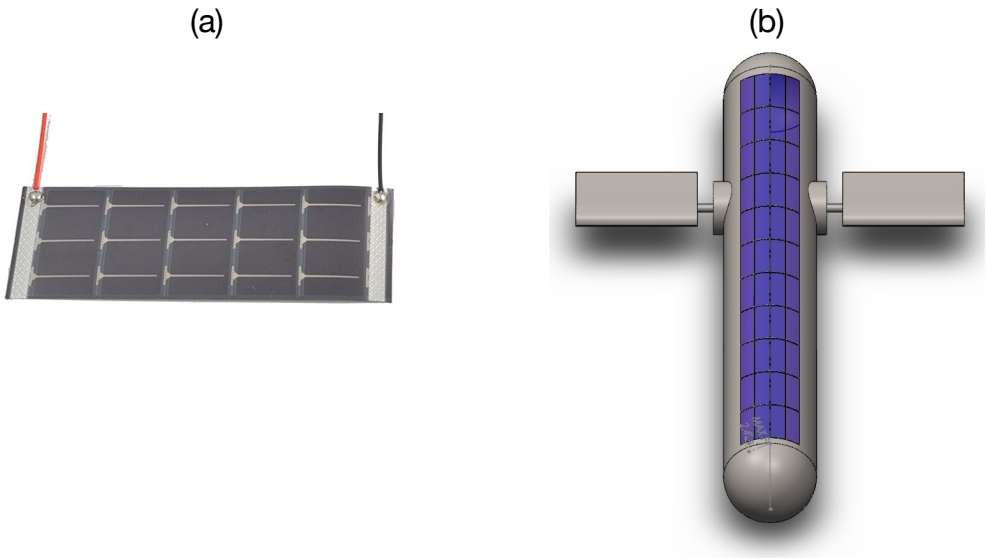

Figure 18: **PV array on the hull.** (a) Powerfilm MP3-37 3 V, 50 mA flexible solar modules ($5/unit) used to construct the PV array on the hull and (b) CAD of the PV array installed on the hull of the UUV.

To maximize the energy harvested by the solar modules, the modules are arranged in a 11 × 4 array (11 rows, 4 columns), which has a 290 in^2 footprint. This geometry maximizes the PV surface array normal to the incident insolation because ±15° about the apex of the hull is utilized for generation. Each module is rated for a maximum flexure of 30° hence the current PV array geometry adheres to this specification. The design choice to connect individual PV modules to construct the array instead of using an off-the shelf module array was governed by the flexure specification. Given the size

of most pre-assembled PV arrays, the flexure would exceed the rated 30° if installed on a cylindrical hull.

2.6.2 PV array circuit and power output

The design of the PV circuit was governed by the goal of minimizing losses due to partial shading of PV modules. Partial shading of a PV array occurs when modules experience unequal lighting conditions and the most shaded module throttles the total power output of the system proportional to the magnitude of shading. This throttled current occurs when PV modules are electrically arranged in series; to avoid the current throttle, the PV modules are wired in parallel, shown in Figure 19.

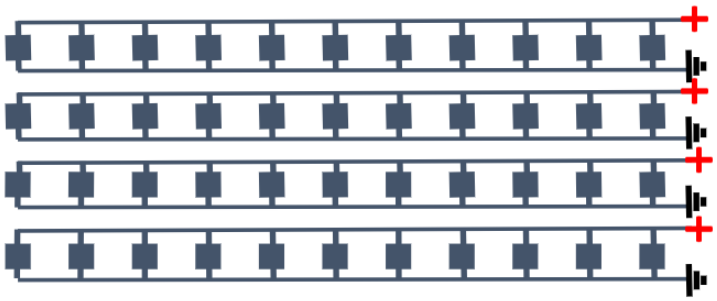

Figure 19: **PV array circuit design.** The 44 modules are arranged in parallel to minimize partial shading losses. This circuit has a rated output of 3 V, 2200 mA, and 6.6 W.

In the case of a single module being completely shaded, the maximum partial shading loss of this fully in-parallel, 44-module PV array would be 2.3 % (*i.e.,* 1/44) whereas with a fully in-series circuit, the loss would be 100 %. Although partial shading losses have been minimized, electrical losses are incurred due to the wiring and connections between modules. Connectivity losses between PV modules are typically noted to be 0.5 % by the National Renewable Energy Lab (NREL). Wiring losses of the PV modules are calculated in Section 2.7.3 to be 40 mW/m. Assuming we use a length of wire equivalent to the root of the PV array footprint to connect all 44 modules, given the 6.6 W rated array, 0.1 W is lost due to wiring; equating to 1.6 % loss due to wiring.

Using the rated power and loss values, an estimated power output value of the PV array is calculated. The estimated power of the circuit is computed using the maximum power output condition. The maximum power output condition for the entire array is when the angle of incident insolation is normal to the apex of the hull. As this angle diverges from 90°, the estimated power of the array decreases proportional to the

angle of the sun relative to the surface of the module, θ. The following equation is used to calculate the estimated power of the 44-module PV array:

$$P_{est} = P_{rated}\,(1 - \ell_{wire})(1 - \ell_{conn})sin(\theta) \tag{4}$$

Where $P_{est}$is the estimated power output, P_{rated} is the rated power, $\ell_{wire}$is the wire loss, $\ell_{conn}$is the connection loss, and θ is the angle of the sun relative to the surface of the module.

PV Array Column	Minimum θ [degrees]	Rated Power [W]	Estimated Power [W]
1	82.5	1.65	1.6
2	75.0	1.65	1.5
3	75.0	1.65	1.5
4	82.5	1.65	1.6
Total		**6.60**	**6.2**

Table 7: **Estimated power breakdown.**

Therefore, for the maximum power condition, the estimated power output of the PV array is 6.2 W, accounting for approximately 21% of the typical dive cycle energy requirement if the vehicle charges at the surface for one hour. The PV array could fully charge a 29 Wh-dive by charging on the surface for approximately 5 hours.

2.6.3 Other PV array designs and challenges

Several other PV module circuits were analyzed including full series connection, combined series-parallel connection, and bypass diode constructions. The full parallel connection was chosen because it naturally minimizes self-shading loss. Series and combination connections require bypass diodes for each module in series to mitigate self-shading, in turn, increasing circuit complexity. Thus, the series and combined series-parallel designs were not chosen. Additionally, a challenge of surface fouling may occur on the PV modules as a result of salt deposition. However, it is unclear as to

whether the losses due to this fouling will be significant since the UUV will resubmerge after a given amount of time to wash away the deposited solids.[7] [8] [9] [10] [11] [12]

2.7 Electronics integration and wiring

To ensure smooth integration between our two different energy generation methods, energy storage and our wide array of electric payload, we need to make available multiple nodes with voltages matching the payload requirements, and ensure that the cabling can handle the required currents.. The operating voltages and currents of each of the components are summarised in the Table 8 on the following page.

---

[7] "Bypass Diodes | PVEducation" [Online]. Available: https://www.pveducation.org/pvcdrom/modules-and-arrays/bypass-diodes.

[8] "Shading Losses for PV Systems and Techniques to Mitigate Them," Aurora Solar Blog.

[9] Marion, B., Adelstein, J., Boyle, K., Hayden, H., Hammond, B., Fletcher, T., Canada, B., Narang, D., Kimber, A., Mitchell, L., Rich, G., and Townsend, T., 2005, "Performance Parameters for Grid-Connected PV Systems," *Conference Record of the Thirty-First IEEE Photovoltaic Specialists Conference, 2005.*, IEEE, Lake buena Vista, FL, USA, pp. 1601–1606.

[10] Dupré, O., Vaillon, R., and Green, M. A., 2015, "Physics of the Temperature Coefficients of Solar Cells," Solar Energy Materials and Solar Cells, **140**, pp. 92–100.

[11] "PowerFilm Solar: Electronic Component Solar Panels Spec Sheet."

[12] "Solar Radiation on a Tilted Surface | PVEducation" [Online]. Available: https://www.pveducation.org/pvcdrom/properties-of-sunlight/solar-radiation-on-a-tilted-surface.

Component	Voltage [V]	Max Current [mA]
PV cells	3	2200
H Fuel Cell	8	3750
Battery (charging)	14	5950
Battery Discharging	12	4630
Motor	24	3490
CTD	12	24
Hydrophone	12	200
Snorkel Pump	12	300
Snorkel Servo	5	500
Iridium	5	34
Raspberry Pi B4	5	1200
Clock	3.3	0.65
GPS	3.3	31
IMU	3.7	3.8

Table 8: **Summary of vehicle electrical components and requirements.**

To make voltage adjustments, we use DC DC Buck/Boost Converters, which have higher efficiencies than linear voltage regulators.

2.7.1 Step-Up DC DC converter (Boost)

For the cases where we require step-up voltage converters, we selected the *DFR0123.* With an input and output range of 3.7-34 V, at an efficiency of 90%, it falls well within our required operating range. While the rated power is only 15W, which is less than we will need in some instances, multiple converters can be coupled in parallel, without incurring any additional penalty, besides mass, volume and cost. The numerical values of these three penalties is fairly low though.

This component will be used between the power generation sources and the battery, as well as in from the battery to the motor.

2.7.2 Step-up DC DC converter (Buck)

For those cases, where we need to reduce voltages, we will make use of the R-78W range from Recom Power. We will use two different models (R-78W5.0-0.5 and R-78W12-0.5) for 5 and 12 V outputs, operating at efficiencies of 93% and 96% respectfully, and an input voltage of up to 32V. These components are very small, and can only handle a maximum current of 500 mA. But, similar to the step-up models, we can stack these in parallel as well, without incurring any loss penalties.

These converters will be used downstream of the battery to create one 12V and one 5V node, for the remaining payload requirements. Figure 20 shows the different voltage nodes and current values along the individual wires in the DOUG LE1000 system.

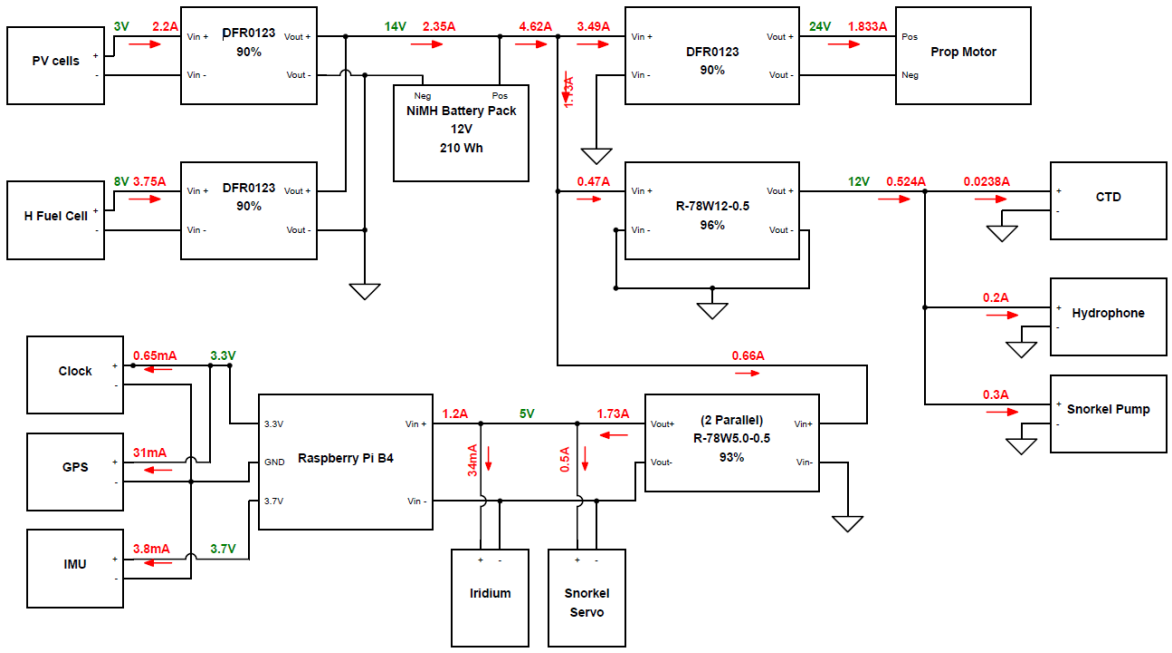

Figure 20: **Electrical Schematic of the DOUG LE1000.** Electrical schematic of the power system, including the values of the voltage nodes as well as the values of the maximum current flowing through each of the wires.

2.7.3 Wire Gauge Selection

Larger currents in wires require larger diameter wires, but add additional weight and cost to the system. Thinner wires also increase the resistivity and thus power loss along the length of the wire according to the formula:

$$Loss = rlI^2 \tag{5}$$

Where *r* = resistivity [ohm/meter], l = length [meter] and I = current [*Ampere*]
The following wire gauges were selected for the respective connections, optimizing between mass increase and losses, with more weight resting on the power losses of the system, in terms of our higher order system requirement of endurance.

Connection Path	Max Current [mA]	AWG Gauge	Wire Diameter [in]	Loss [mW/m]
PV to converter	2200	14	0.064	40
Fuel cell to converter	3750	12	0.081	75
Converter to battery	2350	14	0.064	45
Battery Out	4620	12	0.081	110
Step-up to motor	1833	14	0.064	30
12V components	524	18	0.04	5
5V components	1730	24	0.02	260
5V to Pi	1200	24	0.02	125
Pi to 3.3V components	31.65	24	0.02	0
Pi to 3.7V components	3.8	24	0.02	0

Table 9: **Summary of electrical components and requirements.**

2.7.4 Subsystem Breakdown

Column	Quantity	Cost [US$]	Mass [g]	Volume [cm^3]
DFR0123	5	37.50	120	108.8
R-78W12-0.5	2	17.34	9.6	3.42
R-78W5.0-0.5	4	33.60	19.2	6.84
Total		**88.44**	**148.8**	**119.06**

Table 10: **Cost, mass, and volume summary for electrical components.**

2.8 Energy next steps & test plan

2.8.1 Hybrid Fuel Cell / Buoyancy Engine System

Because the hybrid fuel cell buoyancy engine is a novel system, various aspects of the system design must be validated through testing.

Fuel cell performance: One major unknown in the fuel cell operation is the consistency and flow rate of the outlet. This appears to depend on back pressure. In order to optimize the outlet and reduce the amount of wasted hydrogen, testing should be done using a digital mass flow meter capable of measuring gas flow. A condenser may be used downstream of the mass flowmeter to determine the percentage of water vapor in the outlet gas. An orifice should be used to restrict the outlet flow, and product composition should be measured for a range of orifice sizes, with the goal of reducing the amount of hydrogen purged from the fuel cell.

Aluminum reaction: There are a range of tests that should be done to validate the aluminum-water reaction at the specified conditions. The reaction should be tested at the specified temperature and pressure (0-10°C, 10 MPa), as well as for the aluminum fuel composition specified (60% aluminum, 40% canola oil plus additives) and in seawater. Vitamin C has been referenced as an additive to the aluminum fuel composition that will prevent the salt in the seawater from impeding the aluminum reaction. Tests should be done to characterize the reaction time. Potential mechanisms

for injecting the fuel should be tested, in order to maximize the surface area of fuel as it is injected into the bladder and minimize reaction time.

2.8.2 Fuel Cell Operation and Snorkel

The fuel cell performance should be tested by running the fuel cell in a simulated pressure hull with the snorkel and air vent design. Thermocouples should be placed at the surface of the fuel cell as well as several locations in the ambient air to monitor the fuel cell temperature and ensure that the air flow provided is sufficient to maintain fuel cell temperature below 65°C. Heat transfer analysis may also be done to better predict the thermal conditions of the fuel cell.

2.8.3 Propeller Power Regeneration

Further design work should be done to take advantage of potential propeller power regeneration in the event that the propeller is used to reduce vehicle speed, particularly during vertical ascent. Using this propeller power can assist in battery charging and increase vehicle endurance. This energy conversion mechanism is not possible with the current design due to the propeller being a passive folding propeller. If the system were to be improved to take advantage of propeller regeneration, it would need to incorporate a fixed propeller or a folding propeller with a locking mechanism.

3 Hydrodynamics and Propulsion

This section describes the vehicle's hybrid propulsion system and the design of the glider wings. It was decided early on in the design process that both a propeller and buoyancy engine would be integrated in an attempt to increase energy efficiencies, achieve speed-related system requirements and provide flexibility in mission profile. Glider wings would allow the vehicle to move laterally at slow speeds without the propeller, and at moderate to high speeds with reduced propeller power.

3.1 System requirements

Requirement	Value	Reasoning
Mission Length	30 days	Sponsor Requirement
Maximum External Pressure	10 MPa	Sponsors require 1000m depth
Maximum Burst Speed	2 knots	(1 m/s). Required by sponsor
Maximum Bladder Vol. Change	500 mL	Packaging constraints, see Section 3.5

Table 11: **Hydro system requirements.**

This subteam's design process was heavily centered around two of the vehicle's system requirements: achieving a vehicle speed of 2 knots (1 m/s) and serving a 30-day mission. It was decided that the vehicle must be able to travel at 1 m/s in both the horizontal and vertical direction, but travelling at this speed would not be feasible for 30 days. Therefore, our team chose a cruise speed requirement of 0.1 m/s to accommodate the 30-day requirement. This allows the vehicle to cover a range of 400 km, assuming that the vehicle moves laterally for 70% of the time, using the remaining time to ascend, descend, and recharge at the surface. 400 km was deemed sufficient based on an analysis of common UUV use cases for scientific data collection and pipeline monitoring. Another self-imposed requirement for the buoyancy system was the change in volume of the bladder, or deltaV, set at 500 mL. This was selected with vehicle speed requirements in mind but was ultimately driven by packaging constraints and is discussed further in Section 3.5.

3.2 Hydrodynamics and Propulsion system overview

Both a buoyancy engine and propeller are used in this vehicle for lateral and vertical movement in the ocean. The 1 m/s burst speed requirement served as a motivating factor for a hybrid system, seeing as a pure buoyancy engine system would need to create an unrealistically high change in volume. Additionally, it was assumed that a hybrid system would be generally more energy efficient than a pure propeller system, with the propeller used for only a portion of the mission. Finally, the propeller introduces a finer element of control than the buoyancy engine can achieve on its own, especially when considering a buoyancy engine that is controlled by a variable aluminum-water reaction. In other words, it is much easier to turn with a propeller. At depth, aluminum reacts with seawater within a bladder. Hydrogen gas is a product of this reaction, serving to inflate the bladder and create positive buoyancy at depth. When the vehicle wants to descend, all hydrogen gas is expelled from the bladder. The vehicle is neutrally buoyant with an empty bladder, so in order to dive, the vehicle adjusts its center of mass to pitch the vehicle's nose towards the ocean floor and uses the propeller to provide thrust.

3.3 Aluminum buoyancy engine system

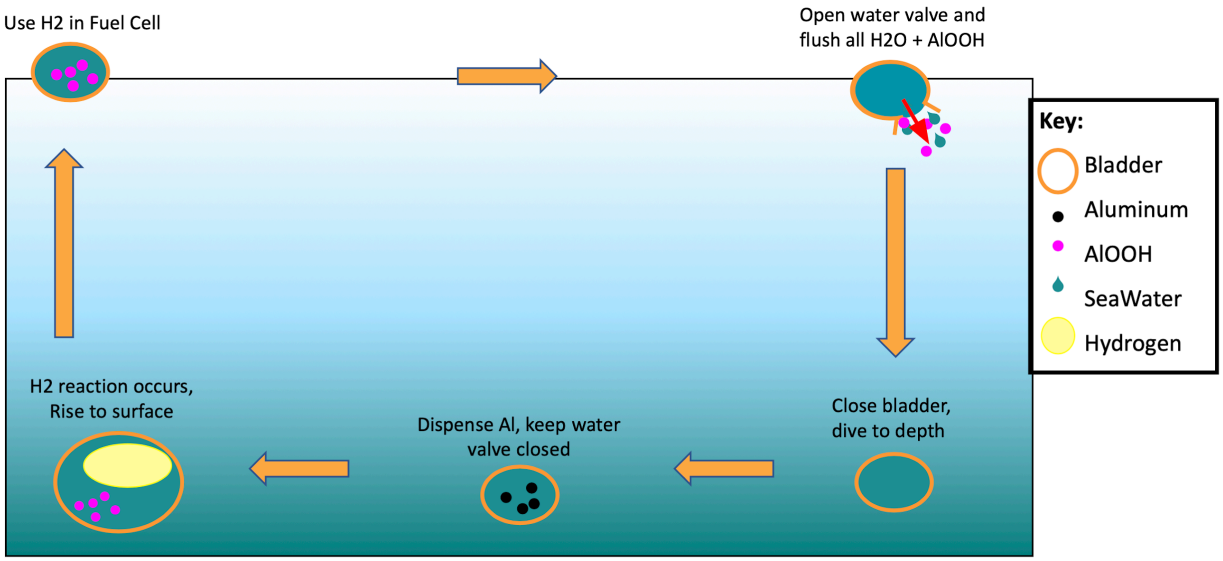

Figure 21: **Aluminum buoyancy engine cycle behavior.** State of the reaction bladder as it traverses a single dive cycle. Aluminum and water react here to produce H2 and AlOOH.

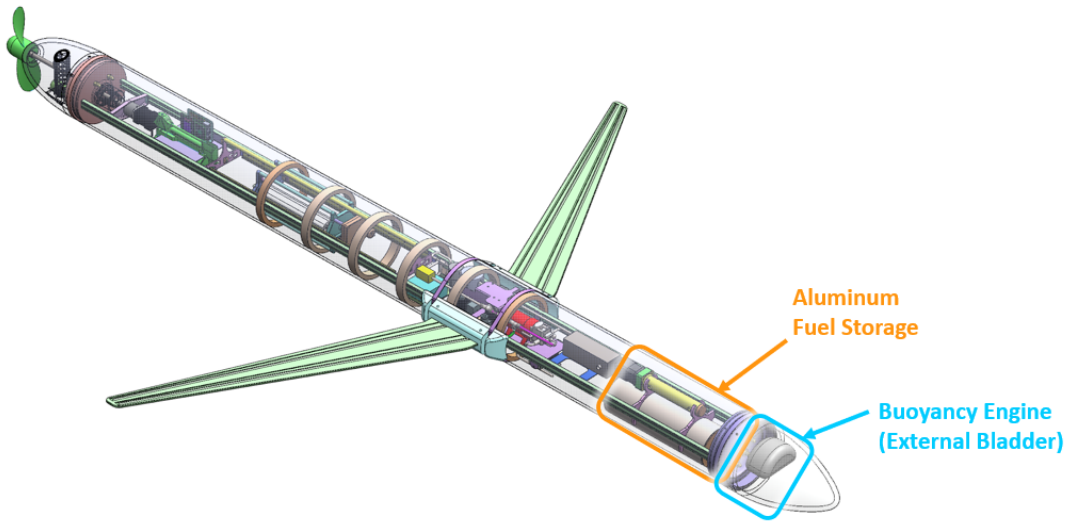

Figure 22: **Aluminum buoyancy engine location on vehicle.**

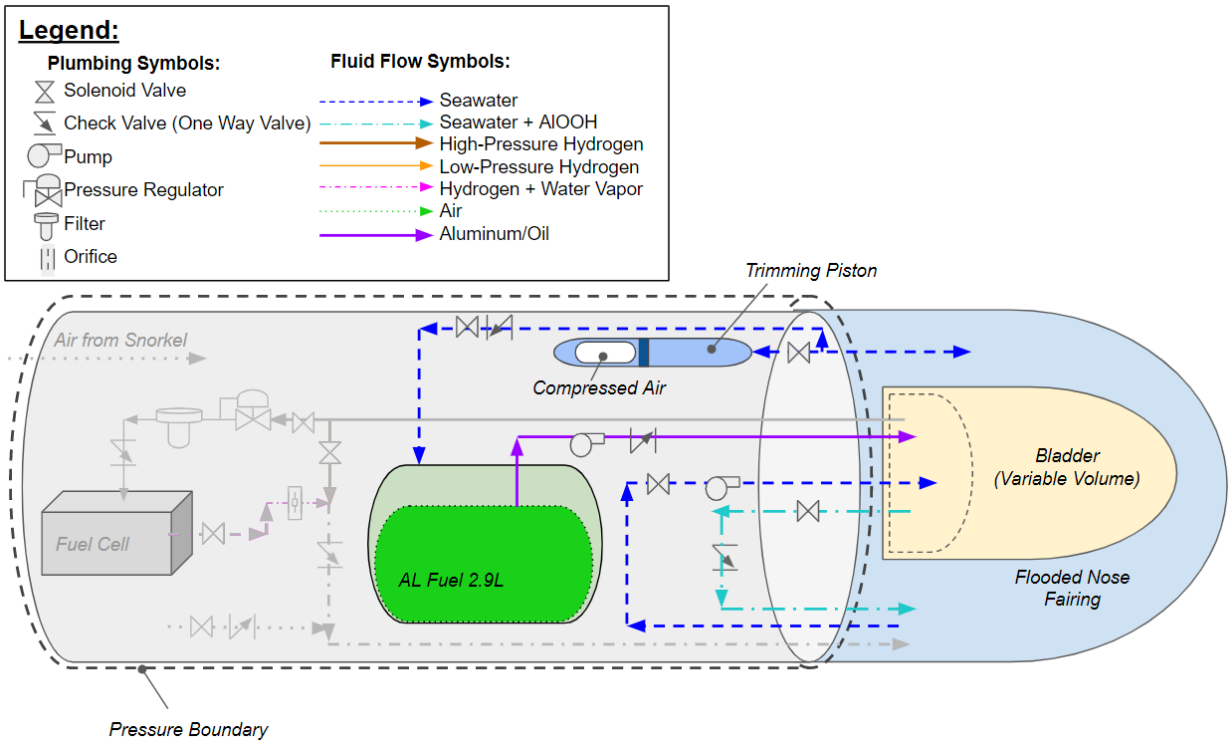

Figure 23: **Aluminum buoyancy engine schematic.** The layout of the buoyancy engine, as located in the front nose of the vessel including valves, pumps, bespoke piston elements and the reaction bladder itself. Gray arrows are for energy subsystem components, shown in Figure 13.

3.3.1 Reaction Bladder

The reaction for the system's hydrogen production will occur within the 'Reaction Bladder.' This bladder serves two purposes: expanding / contracting in order to act as a buoyancy engine, as well as serving as the location of hydrogen production.

This bladder will be made of a mylar-reinforced material due to mylar's proven ability to contain high pressures of hydrogen with low leakage rates. The bladder will be rated to 3 ksi (20 MPa) of pressure, which translates to a material yield strength of 20 MPa, which is well within the range of expected bladder materials. The bladder is expecting an internal pressure of around 5 MPa at surface, and up to 10 MPa of pressure at the maximum 1000m expected depth. The 20 MPa rating accounts for a high factor of safety and reflects currently available materials.

The bladder will be compressible, with a maximum volume of 0.6L, in order to account for the 0.5L change in volume needed for the buoyancy engine as well as the small amount of aluminum and water needed for the reaction. The bladder is designed to be corrosion-resistant in order to survive the vehicle's endurance requirement while being exposed to seawater throughout the mission.

3.3.2 Aluminum Reaction Properties

A detailed account of the ideal reaction, including hydrogen generated and corresponding Al required, can be found in Section 2.4.2. Here we will discuss this reaction's impact on the bladder from a thermodynamic perspective. As shown in Figure 24, the hydrogen generated will attempt to assume a pressure equivalent to external conditions, which varies based on depth by expanding the bladder. As discussed in Section 3.3.1, the reaction bladder volume is limited to 0.5L of hydrogen expansion, as shown in Figure 24 (a). This bladder volume change directly corresponds to a buoyant force and thus a vertical velocity, both of which are plotted in Figure 24 (b) and (c), respectively.

The buoyant force is calculated using Equation (6):

$$F_B = \rho g V \tag{6}$$

Where ρ= 1000 kg/m3, g=9.81 m/s2, and V= vehicle volume. The vehicle is designed to be neutrally buoyant at sea level with an empty bladder. The hull compresses linearly with depth up to .09L at 1000m. This hull compression is factored into the buoyancy

calculation, shown in Figure 24 (b). Because the reaction time is slowed at low temperature, high pressure conditions, the reaction must be timed during the descent so that the vehicle becomes positively buoyant at the appropriate depth. Testing must be done to accurately predict reaction times.

Vehicle descent velocity is controlled by the propeller. Vehicle ascent velocity is driven by the buoyancy engine and is calculated using Equation (7):

$$v = \sqrt{\frac{2(\rho V g - mg)}{\rho k A}} \tag{7}$$

Where m = 80kg (vehicle target mass), k= 0.3 (coefficient of drag), and A= 0.032 m^2 (vehicle cross sectional area).

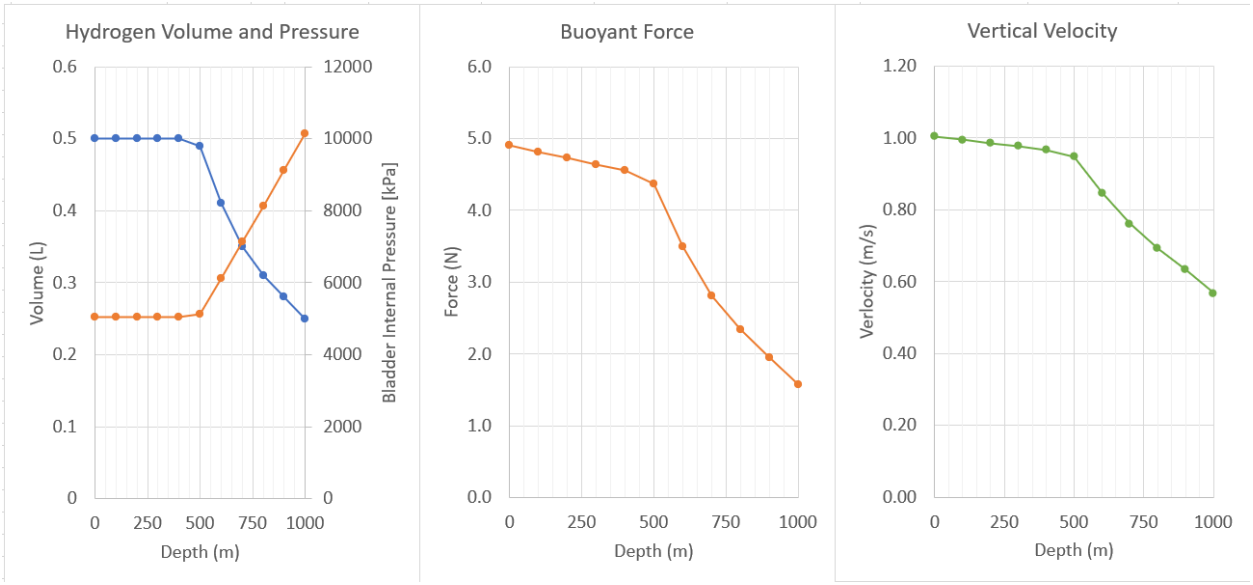

(a) (b) (c)

Figure 24: **Vertical ascent profile.** Buoyancy and vertical velocity for vehicle ascent, using 20g of Aluminum.

Aluminum in water is an exothermic reaction, with approximately 50% of the aluminum's chemical energy (29.1 MJ/kg) being released as heat. The time-averaged temperature of the reaction can be estimated using Equation (8):

$$Q = h\Delta T \tag{8}$$

Where *Q* is the heat released by reacting 20 g of Al, which has a reaction energy of 15.7 MJ/kg Al. By using an estimated heat transfer coefficient *h* based on the expected mass and specific heat of the Mylar bladder, the water, and the aluminum, and by setting the ambient temperature just outside the bladder at 273.15 K, we calculated a bladder internal temperature on the order of 350 K. While just an order-of-magnitude estimate, this temperature is well below the melting point of the mylar bladder and thus we conclude thermal gradients will not be a concern when operating our buoyancy engine.

3.3.3 Aluminum Fuel System

The way in which aluminum fuel is dispensed into the reaction bladder is a determining factor in the accuracy and reliability of the reaction. [13]

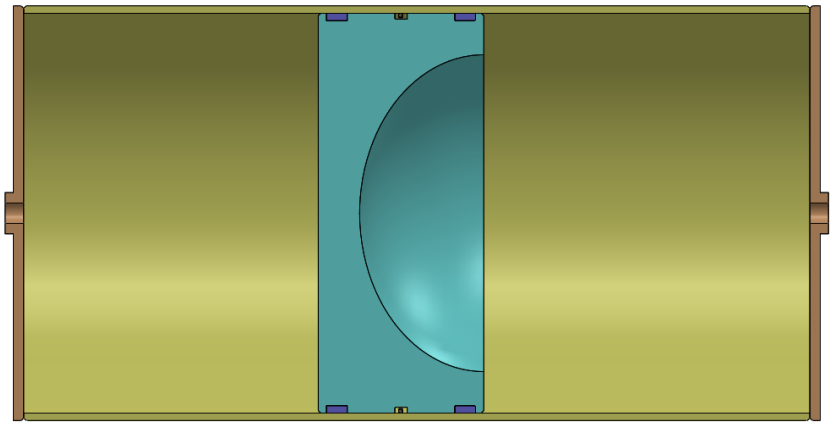

Figure 25: **Aluminum Dispensing System.**

At the beginning of the design process, it was thought that the aluminum could be dispensed at the surface into the empty bladder, simplifying the backpressure and sealing requirements of the dispensing mechanism and its plumbing. However, to ensure a flexible mission profile, the team chose to pursue a dispensing mechanism that could be utilized at most points of the dive-cycle – to begin a new reaction after venting below the surface or to reinvigorate a slow-starting reaction. The decision tree below shows the eventual selection of the aluminum dispensing system and fuel type.

[13] Fischman, J. Z., 2019, “The Development and Characterization of Aluminum Fueled Power Systems and a Liquid Aluminum Fuel,” Thesis, Massachusetts Institute of Technology.

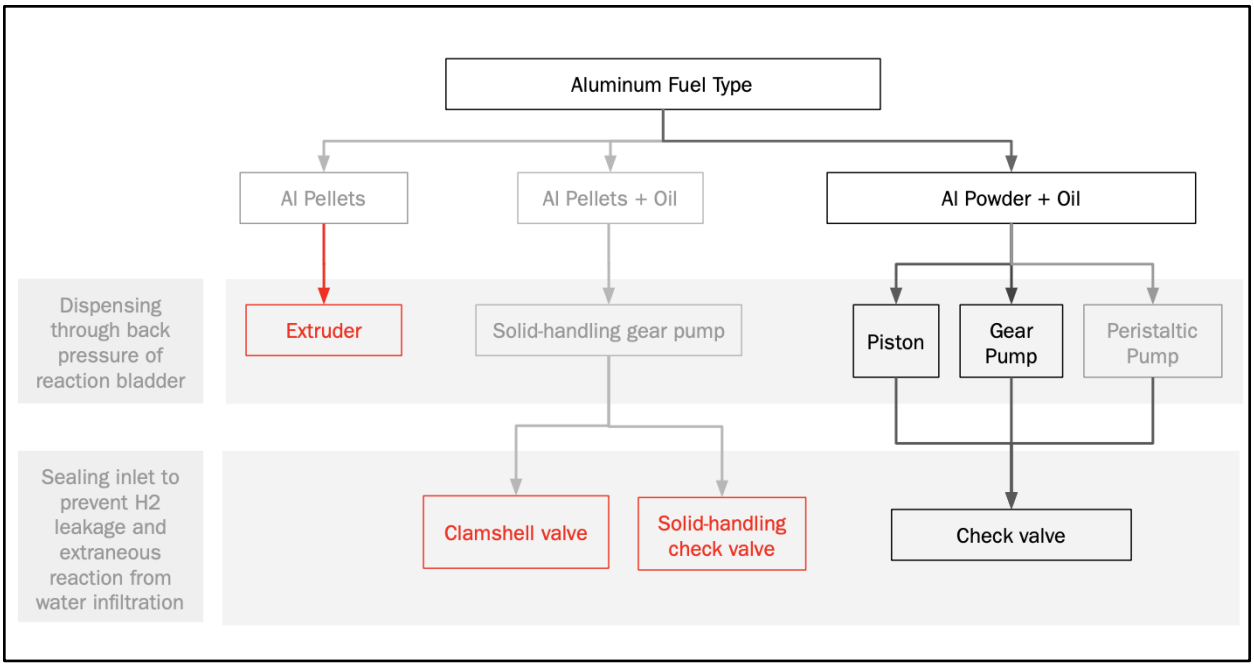

Figure 26: **Decision tree for aluminum fuel, dispensing mechanism and valve type.** Note the primary goals: dispensing through backpressure of the reaction bladder and sealing the fuel storage against hydrogen gas and water.

A secondary goal of facilitating water intake simultaneous to aluminum dispensing to balance the mass of the aluminum lost over the entire mission led to the selection of a piston and a high-viscosity gear pump. The passive piston stores the fuel in an increasingly small volume to ensure consistency in the gear pump's function. While aluminum fuel decreases over the course of the mission, the back end of the piston pulls in sea water, matching lost volume 1:1. As discussed in the proceeding section, the aluminum fuel is denser than water so the adjacent trimming piston accounts for the additional water intake for a complete mass balance.

As explained in Section 2.4.2, aluminum storage is required onboard the vehicle to provide hydrogen to the Hydrogen fuel cell. In coupling the buoyancy engine with the fuel cell, hydrogen generated from the aluminum-water reaction can be used to make variable buoyancy, and then to generate electrical energy. While the aluminum fuel buoyancy engine has greater risk compared to the oil-pump or piston based buoyancy engine used in RAPID, the innovation opportunity spans the short and long term. Within the scope of this class and the subsequent 2.014 build process of DOUG, the coupling of the fuel cell and buoyancy engine leads to mass, volume and power savings. Investing in aluminum fuel also forecasts innovation in the underwater vehicle space beyond this project.

As researched by Fischman,, aluminum fuel can be a liquid composed of activated aluminum powder particles suspended in oil. In line with the endurance of DOUG, the aluminum fuel solution does not settle significantly after 30 days and does not fluctuate in viscosity between 7 C and 45 C. Fischman also tested a pellet form of the fuel, but found lower reaction rates. [14]

As described in Section 2.4.2, the vehicle will require 20g of aluminum for a 30 day mission. At the time of this design process' conclusion, Fischman's Thesis work stood out as the most promising forrary into aluminum fuel design and application. Thus, the liquid aluminum fuel for this vehicle is as recommended in Fischman's thesis: 60% aluminum powder and canola oil. This mixture yields a liquid of 1.98 g/mL – 12.4mL is needed per cycle and 2.9L per mission.

3.3.4 Pumps and Valves

The buoyancy engine system will be designed to maximize the endurance of the overall system. An aluminum reaction approach will be used to produce hydrogen that will inflate a bladder to help reach a 30-day mission requirement by recycling the produced hydrogen [Section 2.4.2]. Thus, the buoyancy engine and bladder will be connected to the hydrogen fuel cell system through pipes and valves. Additionally, it was later discovered that an immense amount of water is needed to react the 4.8kg of aluminum that would be needed for the mission, so instead of storing fresh water onboard, an open-system is designed for which seawater is pumped throughout the process.

All of the isolation valves, check valves, regulator valves, pipe connectors, and pipes that are needed to operate the buoyancy engine will be sourced to withstand at least 10 MPa, will be resistant to corrosion from sea water, will be able to be controlled through an onboard controller, or will not need any direct controller to function during operations. These requirements assure that the system will be autonomous while being about to withstand all possible pressures that the system may endure during operations. The pump will be selected to flush out excess sea water and ALOOH byproduct at the surface of the ocean. Thus, the pump will only need to operate at least 0.2 MPa.

[14] Fischman, J. Z., 2019, "The Development and Characterization of Aluminum Fueled Power Systems and a Liquid Aluminum Fuel," Thesis, Massachusetts Institute of Technology.

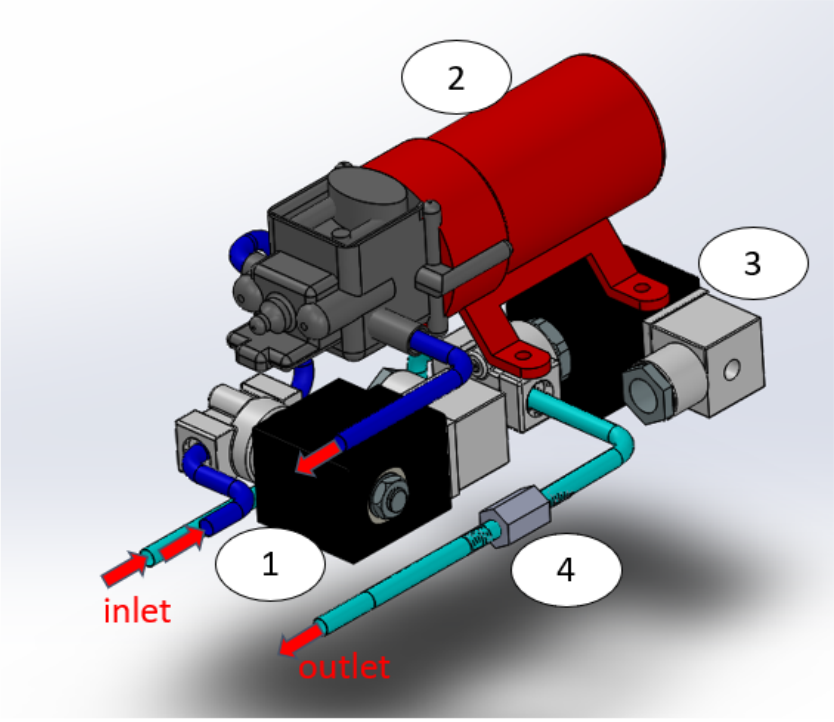

Figure 27: **Flushing Component of the Buoyancy Engine.** Figure 27.1: **Inlet Isolation Valve** Figure 27.2: **Pump** Figure 27.3: **Outlet Isolation Valve** Figure 27.4: **Outlet Check Valve**

The flushing operation shall be carried out as such:

1. An isolation valve will open allowing water to pass through [Figure 27.1].
2. Ocean water will be pumped into the bladder [Figure 27.2].
3. Another isolation valve will be open to allow the bladder to flush out the ALOOH byproduct from the bladder [Figure 27.3]. Outlet will be located at the bottom of the bladder to assist in removing byproduct which has settled at the bottom of the bladder.
4. The check valve is used to prevent backflow of the sea water back into the bladder while the bladder is being flushed [Figure 27.4].

3.3.5 Trimming

In addition to the main buoyancy engine, the overall system will also require a supplemental trimming buoyancy engine. This additional engine will be used to adjust the vessel density by pulling more seawater into the vessel to replace air. There will be a need to adjust density in a variety of instances. As the Aluminum stored in the aluminum fuel tank is depleted, it will be replaced with seawater. However, the seawater will have a lower density than the aluminum. This will require the trimming engine to add additional mass into the vessel to make up for the difference in fuel

density. It can also be used to adjust for miscellaneous buoyancy changes that cannot be controlled as accurately with the main hydrogen buoyancy engine. Utilizing a stepper motor, this buoyancy engine will be actuated with a piston and leadscrew. The 8 in long bore will provide 100 mL of displacement. The inlet of the trimming engine will be connected to the unpressurized section of the vehicle as shown in Figure 28. An isolation valve placed before the inlet will ensure that high pressure seawater at depth will not rupture the piston bore.

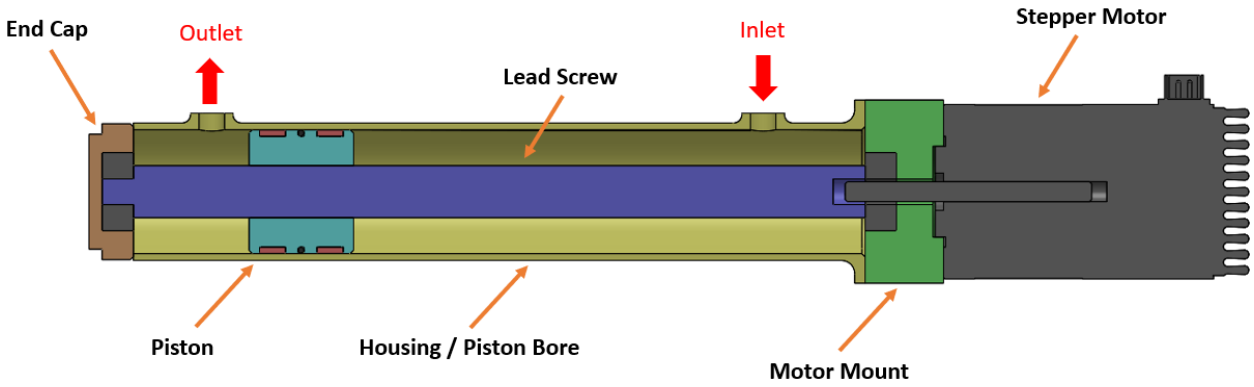

Figure 28: **Trimming Buoyancy Engine.**

3.4 Propeller System

The propeller system configuration can be seen in Figure 29. The propeller hub and blade geometry were designed using OpenProp, an open source MATLAB toolbox. The propeller design process yielded an optimal torque and rotation speed, which guided our choice of motor and planetary gearbox. Finally, with our goal of maximizing efficiency in order to reach our 30-day requirement, a magnetic coupling was chosen to mate the motor shaft to the propeller.

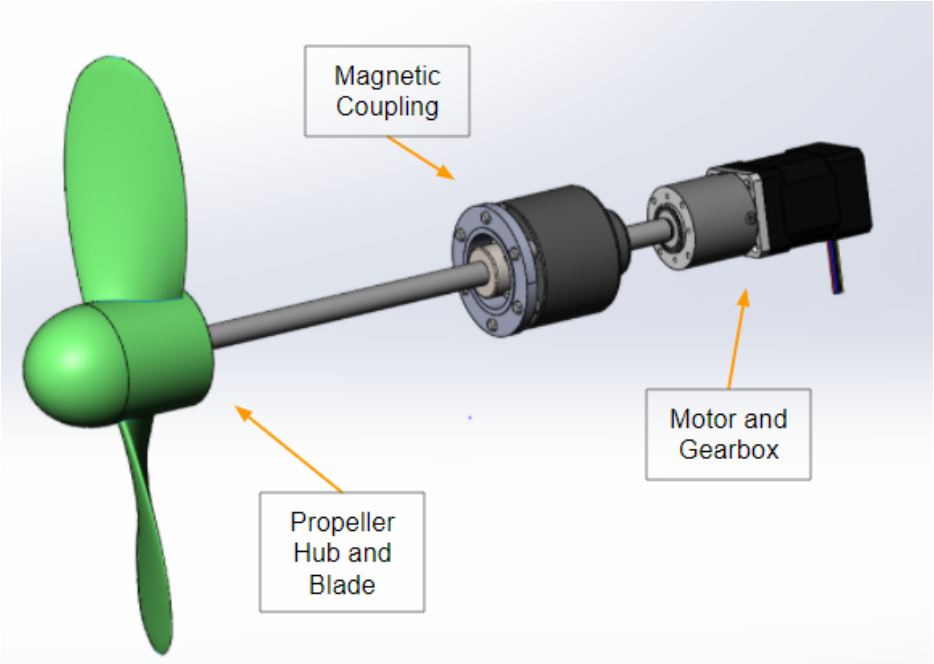

Figure 29: **Propeller System Configuration.** The propeller hub and blades, magnetic coupling, and motor-gearbox assembly pictured from left to right.

3.4.1 Propeller Design

3.4.1.1 Commercial Thruster Systems

Early in the design process, one of the major decisions to be made was whether to use an existing underwater thruster or a custom propeller / motor system to propel the UUV. Although an off-the-shelf thruster system would be desirable for the low cost and ease of integration, the majority of commercial thrusters consume large amounts of power and would not be suitable for a long endurance vehicle. In addition, because of the 30-day mission requirement, optimally designing a propeller and choosing a motor that directly reflects the required specifications would be the most advantageous when it comes to vehicle efficiency and endurance. Another alternative to designing the entire system from scratch was to purchase a commercial thruster, remove the

propeller, and add a custom designed propeller to the commercial motor / housing. This was initially considered as a viable option, but early stages of the propeller design process indicated that the motors in all of the commercial thrusters found operate at significantly higher rotation speeds than the optimized propeller would need.

3.4.1.2 OpenProp

After deciding to pursue a custom propeller, an open-source tool known as OpenProp was used for the propeller design. OpenProp is a MATLAB based software that utilizes lifting line theory to develop optimal propeller geometry given certain input parameters, shown below in Table 10. The software then takes these inputs and provides 3D geometry of the optimized propeller, as well as various performance characteristics of the design.

A Parametric Study Tool was used to optimize the input parameters and maximize propeller efficiency. As shown in Figure 30, this tool takes in the known fixed parameters (required thrust, ship speed, hub diameter, fluid density), and then a specified range of values for the varying inputs (number of blades, propeller diameter, propeller rotation speed). Required vehicle thrust was determined to be 25N, ship speed is 2 kts (system requirement), and hub diameter was chosen to be 0.06m (20% of the largest propeller diameter). In this study, the number of propeller blades was varied between two and three, as that is the most common practice for the majority of existing UUV systems. The propeller diameter was chosen to be the range of values from 8in to 12in, which corresponds to 100% of the hull diameter to 150% of the hull diameter. Rotation speed was chosen to range from 200 - 500RPM, which was decided by sweeping through a number of different rotational speeds and narrowing the range down based on efficiency.

Input Variables	
Number of blades	*2 - 3*
Propeller diameter	*8 - 12in*
Propeller rotation speed	*200 - 500RPM*
Required Thrust	*25N*
Ship Speed	*2 kts*
Hub diameter	*2.4in*

Table 12: **Input Variable Table**. OpenProp input variables and their respective values.

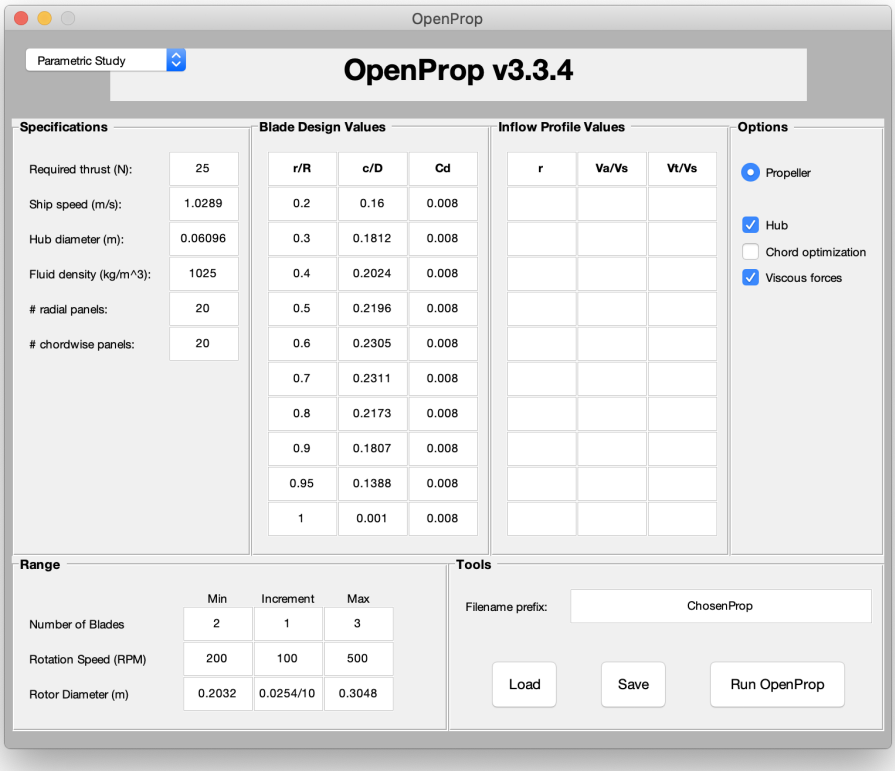

Figure 30: **OpenProp Parametric Study**. Fixed inputs shown in the Specifications tab top left, dynamic inputs shown in the Range tab bottom left. The Blade Design Parameters tab is auto-populated by OpenProp.

Results of the Parametric Analysis are shown below in Figure 31. Efficiency vs. propeller diameter is plotted in both graphs, with the only difference being that the first is for a two blade design and the second is for a three blade design. The different color curves illustrate the varying rotational speeds from 200 - 500 RPM for both blade configurations. As the graphs show, regardless of the number of blades, the most efficient design is a 12” diameter propeller spinning at 300 RPM. For the two blade design these values result in an efficiency of 73.2%, and the three blade design is 73.0% efficient. This efficiency trade-off led to the chosen design of two propeller blades, a 12” propeller diameter, and 300 RPM rotational speed.

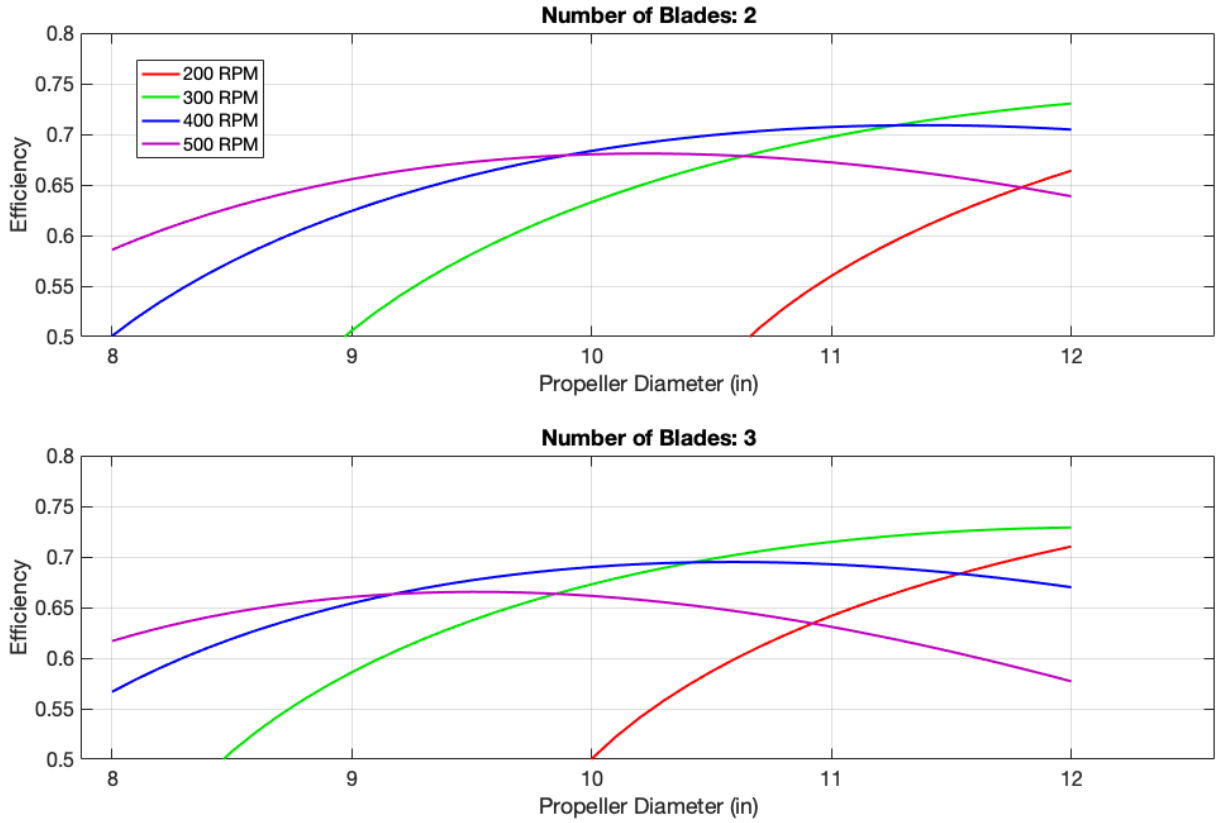

Figure 31: **Efficiency vs. Diameter Plots**. Two blade design shown on top and three blade design shown below that. Colored curves indicate running the propeller at different RPM values as shown in the legend top left.

The chosen propeller design was then input into the Single Design tool of OpenProp which outputs three-dimensional geometry and in depth propeller design analysis. Although this tool provides an extensive amount of information, there are only a few important performance values required to further the system design. These values include: the propeller efficiency is 73.2% (previously mentioned in the Parametric Study), the torque to the propeller shaft must be 1.12 Nm, and the required power is

35.2 W. These specifications will help later in the design process when it comes to motor selection, energy calculations, and overall system efficiency. The performance curves for this specific propeller geometry are shown below in Figure 32. It's important to note that the propeller efficiency falls slightly short of maximum efficiency for this given propeller geometry. In practice this is actually desirable as it allows the efficiency to remain high during unpredictable perturbations of inflow velocity to the propeller.

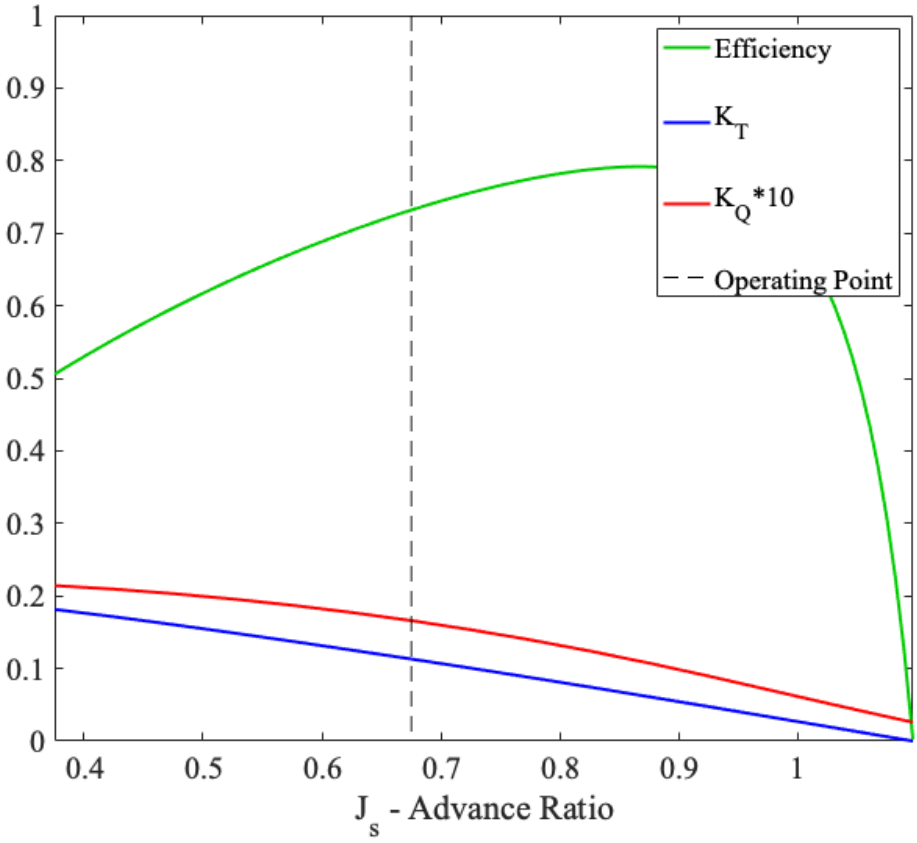

Figure 32: **Propeller Performance Curves**. Chosen propeller design shown by the dashed line. Efficiency shown in green, thrust coefficient shown in blue, torque coefficient multiplied by a factor of 10 shown in red.

3.4.1.3 Folding Propeller

Rather than going with a static, fixed pitch propeller the goal is to pursue a folding propeller design, similar to the propellers used by many racing sailboats. These foldings propellers are much more desirable than a fixed pitch prop. because they significantly reduce the amount of drag on the propeller. The way the mechanism works is when the vehicle is not operating the propeller the blades retract back to the folded position, but the blades are then passively actuated to the operating position through centrifugal forces when the shaft is spinning, A gear system between the two blades also ensures synchronized folding during operation.

Unfortunately, given the remote learning environment and the shortened semester, designing the folding mechanism is out of the project scope. Ideally, in the spring the vehicle will be tested with the chosen propeller geometry (which can be manufactured through 3D printing). If the propeller performs well the design of the folding mechanism could then be outsourced to a company such as Flexofold. Flexofold currently designs 2, 3, and 4 blade folding propellers for sailing applications.

Figure 33: **2-Blade Saildrive Composite Folding Propeller.** Image on the right shows the gear mechanism that allows the propeller to passively actuate from the folded position to the position shown by the image on the left.

3.4.2 Motor Selection

The motor selection process was centered around being able to achieve a top speed of 1 m/s while maximizing efficiency at this top speed. The mechanical power needed to propel the vehicle scales approximately with the square of the vehicle's speed. Therefore, operating at the vehicle's top speed requires roughly 16 times more mechanical power than its cruise speed of 0.25 m/s. By picking a motor whose peak efficiency occurs at the top speed, the vehicle minimizes the electric power loss.

A parametric study was conducted in OpenProp to determine how varying rotation speed and rotor diameter would improve efficiency. After inputting the vehicle's top speed (1 m/s) and required thrust to achieve that speed (25 N), the parametric study showed that maximum efficiency could be achieved with the propeller rotating at 300 rpm (referred to throughout the rest of the section as the DRS). Our motor search anchored around operating near this speed.

In order to achieve this rotation speed, our team explored brushless DC motors with gear reductions. The electronics subteam chose early in the process to implement a DC voltage source, so this led our team to choose between brushed and brushless DC motors. Further research indicated that DC motors would be better for our use case due to their superior efficiency and longer lifespan without maintenance. Initially, the plan was to maintain efficiency by using a direct drive system where the shaft of the propeller would be mated to the motor shaft. However, a preliminary survey of small brushless DC motors found that most motors were highly inefficient operating at low RPMs. For many motors, the rated torque was much higher than actual torque required at the DRS, or the DRS fell outside of the motor's range of continuous use. Therefore, our team determined a gearbox was required to achieve our ideal operating conditions.

With further exploration, the team chose to move forward with the Nanotec DB41M024030 with a high torque planetary gearbox attached. Table 13 lists characteristics of the top three motors we considered in making our decision. The most important characteristic was total efficiency, which is the product of motor efficiency, the gearbox efficiency, and the propeller efficiency.

$$\eta_{tot} = \eta_{motor} * \eta_{gear} \tag{9}$$

Figure 34 illustrates the efficiency and torque supplied at the shaft of the Nanotec motor-gearbox configuration as a function of the shaft speed.

Motor	Prop Diameter [in]	Operating RPM	Operating Torque [Nm]	Total Efficiency*
Nanotec *DB41M024030*	*12*	*320*	*1.1*	*0.6*
Transmotec *PDS4377*	*12*	*229*	*1.53*	*0.42*
Transmotec *PD80138*	*10*	*470*	*0.76*	*0.41*

Table 13: **Motor Comparison**. Motors were selected for comparison based on proximity to our ideal operating RPM. Of the motors surveyed, the three listed were our top three contenders, but with efficiency being of the utmost importance in order to achieve the 30-day requirement, our team is choosing to move forward with the Nanotec motor-gearbox configuration.

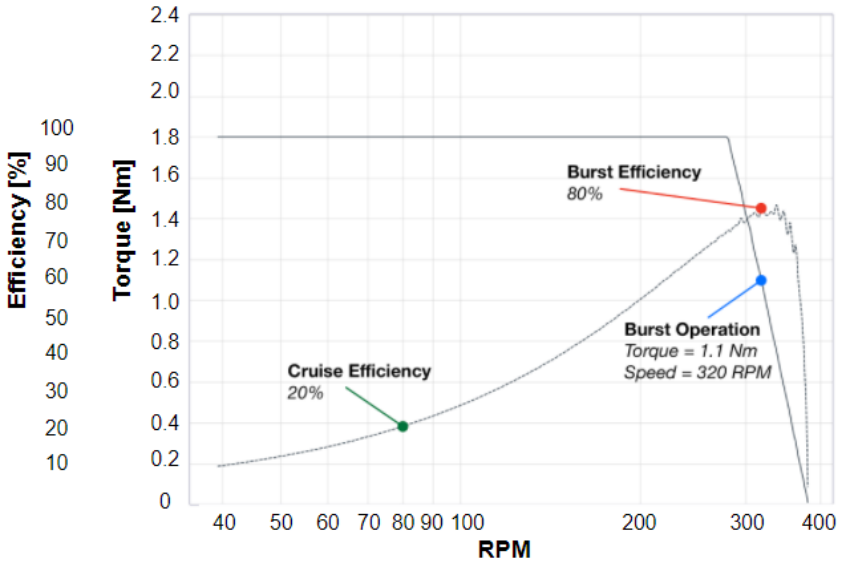

Figure 34: **Efficiency and Torque vs. Speed Curve**. Both cruise and operating characteristics are labelled on the graph, with maximum efficiency taking place at the vehicle's burst speed.

3.4.3 Coupling Selection

During our exploration of potential coupling methods, our biggest concerns were minimizing losses from the coupling as well as preventing any seawater from entering the pressure hull. Two methods were considered for coupling the propeller to the motor, both of which can be seen in Figure 35.

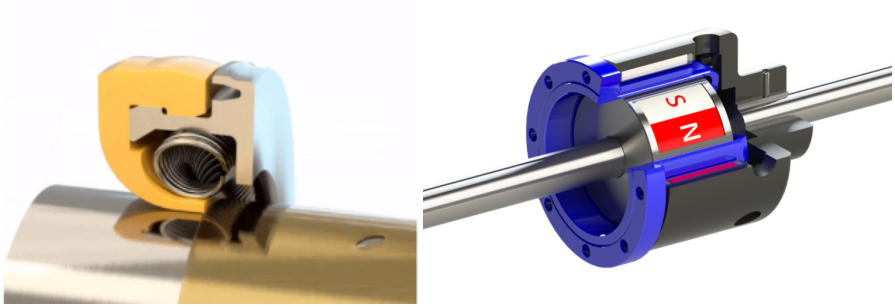

Figure 35: **Coupling Strategies**. An example of direct coupling is shown on the left. The piece shown surrounding the shaft is a high-pressure resistant dynamic seal. On the right, an example of the magnetic coupling strategy shows two magnets, one inside of another, separated by the blue top hat barrier.

The first concept directly coupled the motor shaft to the propeller using a single shaft that would extend from the motor shaft through the pressure boundary of the end cap, all the way to the hub of the propeller. Since the vehicle will be diving to depths 1000 meters, an extremely pressure-resistant dynamic seal would be required to prevent seawater from entering the pressure hull. The other concept centers around the use of a magnetic coupling. A shaft couples the motor to the outer magnet, and the inner magnet couples to the hub of the propeller. A top hat – shaped barrier is attached to the end cap of the hull, allowing for the inner magnet to rotate inside of the outer magnet.

Cost, ease-of-access, efficiency loss, and robustness for our use case were all considered in deciding between these two methods. The cost of direct coupling versus utilizing a magnetic coupling mechanism is much lower since many of the parts can be bought off-the shelf. Magnetic coupling would require the creation of a custom barrier, which drives up the cost of this option. On the other hand, direct coupling would require an extremely tight dynamic seal. This seal would result in detrimental losses due to friction that could be avoided by using magnetic coupling. Additionally, the dynamic seal would struggle to last for the entirety of a 30-day mission while being exposed to extreme variation in pressure. The magnetic coupling would be far more likely to perform at a high level throughout the entire mission. Ultimately, the

performance benefits of using a magnetic coupling far outweigh the cost benefit of directly coupling the motor to the shaft.

The vehicle will use the MTC-3 magnetic coupling supplied by Magnetic Technologies.[15] This company has previously worked with the 2.013 team, and has stated they are capable of creating a coupling that can withstand the deep ocean operating environment.

3.5 Glider Hydrodynamic Design

The glider system was designed to produce lift to provide buoyancy-power lateral motion at low speeds. Glider analysis was done using a two-dimensional steady-state hydrodynamics model that balances the lateral force, vertical force, and pitch moments on the vehicle. The simulation can be found on the project GitHub. A diagram of the simulation is shown below.

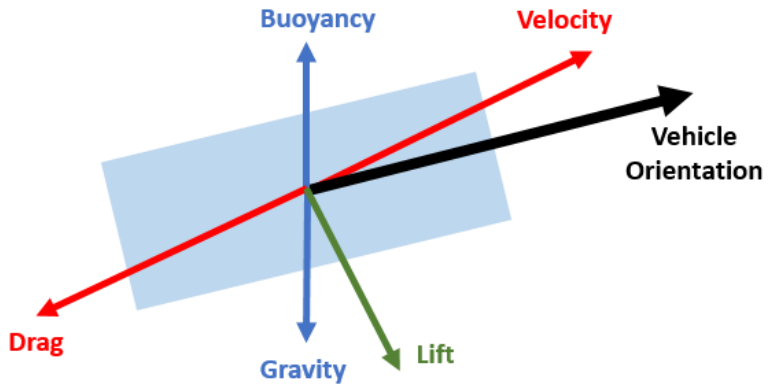

Figure 36: **Vehicle free body diagram**. Shown are the primary forces lifting on the vehicle as it moves through the water.

The simulation calculates the coefficients of lift and induced drag using an elliptical planform assumption. The total drag force is calculated as shown below. The wings create induced drag and skin friction drag, while the vehicle body creates form drag and skin friction drag.

For vehicle with wings:

$$CDA = 2SC_f(1 + \frac{2\pi a\alpha^2}{C_f(2+a)^2})$$

[15] "Magnetic Coupling | Magnetic Drive Pump | Magnetic Technologies Ltd."

For vehicle without wings:

$$CDA = C_f A_{wetted} + C_d A_{cross\ section}$$

where

A_{wetted} = wetted surface area

$A_{cross\ section}$ = cross sectional area

C_d = drag coefficient

Figure 37: **Calculation of drag force.**

In its current realization, the glider reduces the propulsive power required by the propeller when cruising, but it unfortunately does not allow the system to meet the 0.1 m/s average speed requirement (equivalently, 400 km range requirement) from purely the glider without the propeller. This is because analysis shows that enforcing this constraint would have raised the deltaV and therefore the required mass of aluminum fuel, making the full vehicle weight and volume unacceptable for user handling. Therefore, a packaging-constrained dV of 500 mL was selected. In order to still fulfill the range requirement, the decision was made to turn on the propeller not only when the vehicle is moving at burst speed, but also at cruise speed.

The necessity of using the propeller at low speeds is shown in the diagram below: with a dV of 500 mL, there are no reasonable combinations of glide angle and attack angle that meet the range requirement. This is undesirable because the propeller is less efficient in this range, so future teams should re-assess the importance of the 400 km range requirement. If this requirement can be sacrificed, the vehicle can glide without the propeller, reducing energy consumption.

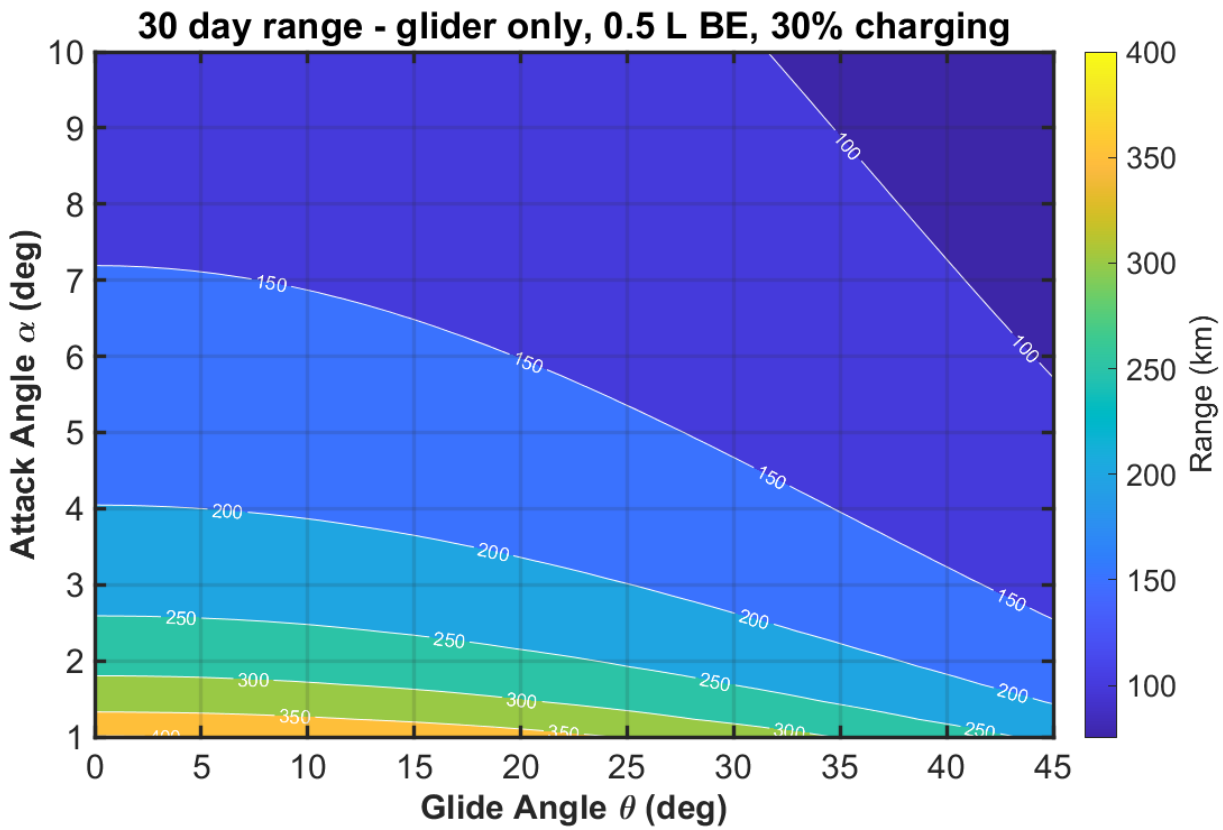

Figure 38: **30-day range plot**. This pot shows range in kilometers as a function of glide angle and wing angle of attack. This is useful for determining values for these parameters that fulfill our range requirement.

The same hydrodynamics simulation was used to guide the design of the glider wings themselves. Key system parameters, such as dynamic response, were found to be highly sensitive to the wing geometry. It was concluded that it is desirable to minimize wingspan (within stability limits) and maximize aspect ratio (within structural limits).

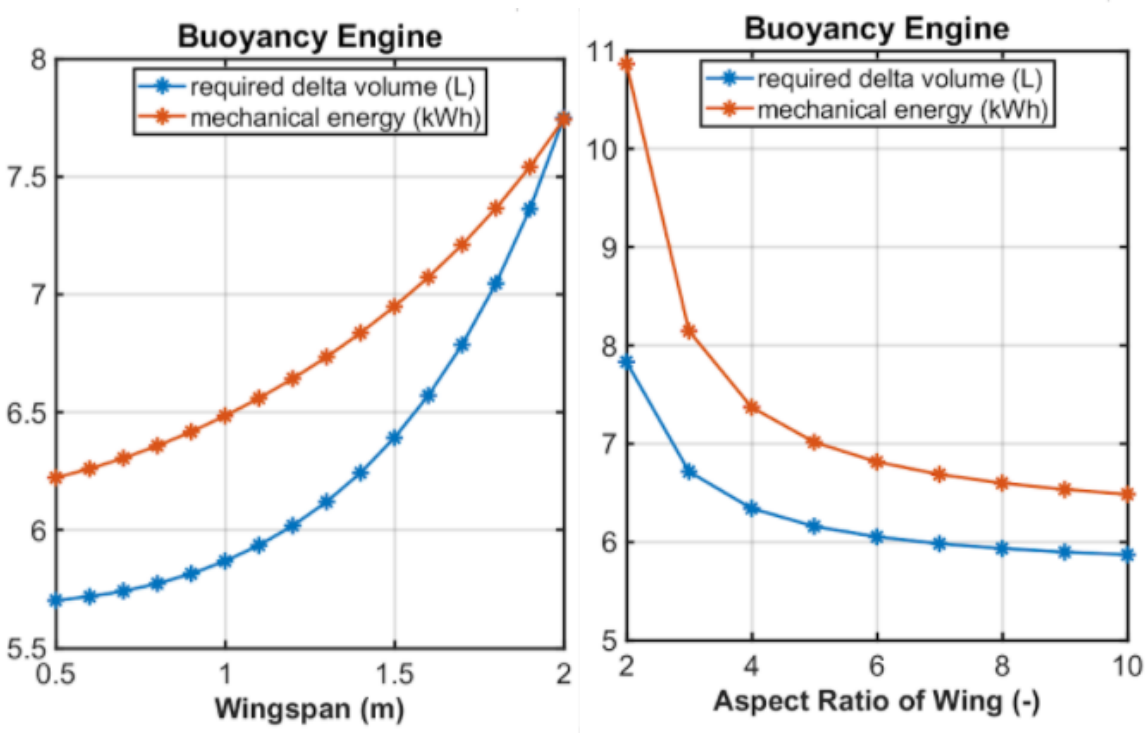

Figure 39: **Buoyancy engine plots**. This pot shows mechanical energy draw and required change in volume of the buoyancy engine as a function of wingspan and wing aspect ratio.

The following table shows the chosen hydrodynamic parameters of the glider wings. Future work could include selection and modeling of a known NACA foil geometry.

Cross section	Symmetric (to allow gliding up or down)
Shape	Flat profile, angled at 45 degrees (to avoid snagging on marine debris)
Wingspan	1 m
Aspect Ratio	15

Figure 40: **30-day range plot**. This pot shows range in kilometers as a function of glide angle and wing angle of attack. This is useful for determining values for these parameters that fulfill our range requirement.

4. Navigation, communication and controls

4.1 System requirements

Requirement	Value	Reasoning
Operating depth	1000 m	Sponsor requirement
Cruise speed	0.2 kts	Sponsor requirement
Maximum burst speed	2 knots	(1 m/s). Sponsor requirement
State estimation precision	20 m	Necessary to achieve desired waypoint following
Transmit collected data	n/a	Vehicle must be able to report data more frequently than just at the end of a 30 day mission
Communicate between vehicles	n/a	Necessary to execute swarm behavior

Table 14: **Navigation, communication and controls system requirements.**

4.2 System overview

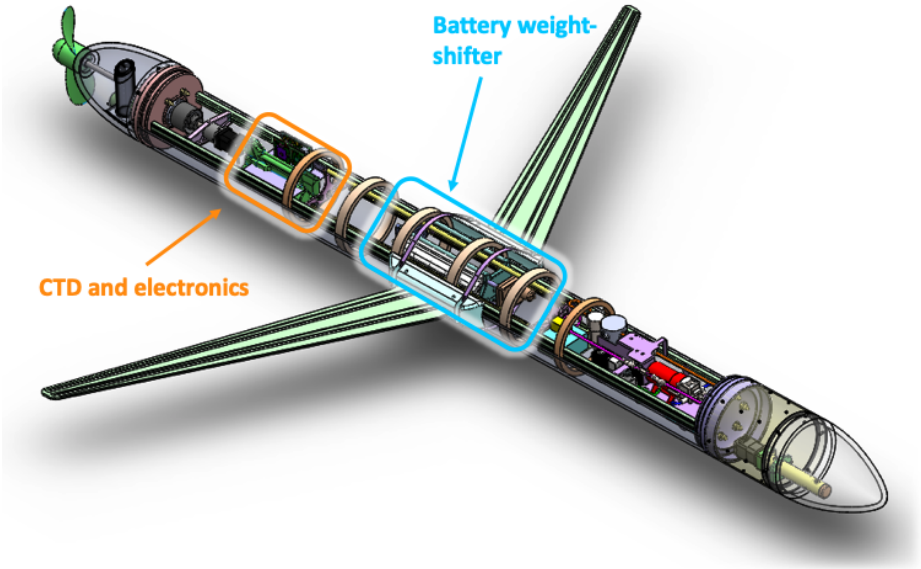

Figure 41: **Navtronics subsystem layout.** Most of the hardware, sensors and electronics in these subsystems are mounted between the skeleton rails towards the rear of the vehicle. The vehicle controller, detailed in section 4.6, is mounted in the middle.

The navigation, communication and controls schemes laid out here build on RAPID's groundwork, driven by the system requirements in Section 4.1. Each UUV independently navigates and collects data, and flags points of interest or data anomalies to be relayed to the rest of the swarm before the next dive. The following subsystems (navigation, communication, and dynamics & control) are designed to enable each vehicle to operate independently over long-endurance missions while supporting RAPID's swarm sampling behavior.

4.3 Navigation

There are many different types of sensor packages and techniques that can be used to aid in the navigation and positioning of an UUV. Combining these types of navigation systems can result in a more robust overall system capable of operating at multiple levels. Incorporating these combined systems into UUV allows them to operate at multiple depths and complete a broader range of missions than any single system.

In order to minimize error and ensure a wide range of operable environments, our system will combine 3 types of UUV navigation systems: an Inertial Navigation System (INS), a Global Positioning System (GPS), and an Acoustic Positioning System.

4.3.1 INS

INS systems combine 3 main sensors: an accelerometer, a gyroscope, and a magnetometer. INS is used to determine the position of the vehicle they are installed in. Taking the data from these sensors, they are able to sense the vehicle's linear acceleration, angular velocity, and magnetic field vectors.

These systems are common in UUVs because of their ability to operate in environments that are not suitable for GPS use. As our vehicle will be operating at depths of up to 1000 meters, the INS will be used to calculate the position of the vehicle when GPS cannot.

However, there are also drawbacks to the use of INS. These systems accumulate error (a.k.a. drift) over time as there is error associated with each measurement taken from these sensors. As INS does not have any dead reckoning points, using them over long periods of time leads to accumulation of error that becomes too large to manage. Our vehicle will be operating for many hours, so it will be necessary to incorporate a dead reckoning system.

4.3.2 GPS

Combining an INS system with a GPS can help reduce this positional error further. An INS/GPS integration helps offset the inherent drift of INS by utilizing GPS' ability to provide instantaneous positional accuracy. By providing an accurate instantaneous location periodically, the system can achieve a more accurate starting location for dead reckoning navigation.

The obvious drawback of GPS is that it is only usable in very shallow or surface conditions, as the signal cannot travel through water to the receiver. However, as our vehicle will be intermittently surfacing, this provides a perfect opportunity to use GPS for instantaneous positioning.

4.3.3 Acoustic positioning

A modern advancement in UUV navigation is the implementation (or fusion) of multiple sensors to reduce the uncertainty in position determination. Maintaining accurate localization of UUVs is difficult because electronic signals such as radio waves or GPS do not travel well underwater. A possible solution to this problem is the use of acoustic positioning, where acoustic signals are sent from a surface vehicle and received by underwater vehicles. The vehicle's 3-dimensional position can be computed by

triangulating the distance traveled by the three signals, much like how GPS works on land. Acoustic positioning has the ability to bound the uncertainty of the underwater UUV's position determination to around 10m.[16] This method is especially effective within a swarm of cooperating UUVs because we can lower the cost and complexity of the system by only using 1 hydrophone and 1 acoustic projector. Incorporating acoustic positioning into this system while utilizing the swarm sampling scheme would be able to increase the accuracy of the system to the point required by the system requirements.

The cost associated with this technique was a major concern for the group. Placing sensors all over the ocean floor in the area of each operation would be extremely inefficient. As a subteam we came up with a solution that fits in well with our overall UUV strategy. Figure 42 denotes our decision tree for choosing the right navigation scheme. We focused on the accuracy of the system, the implementation cost and time, the cost of the vehicle, and the complexity of the system to decide on an overall navigation scheme. We plan on utilizing the swarm technology pioneered by RAPID to our advantage by establishing some UUVs as points usable for dead reckoning.

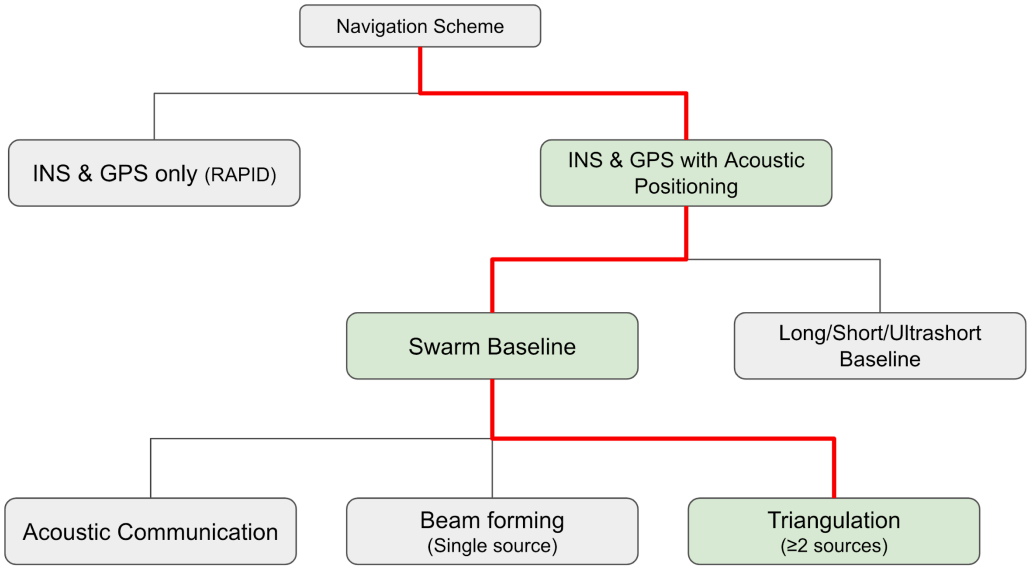

Figure 42: **Navigation Decision Tree.** The diagram above shows the options we investigated for an overall navigation scheme. As you can see we chose early on to add a form of acoustic positioning to our system. We ended up deciding on SLBL to lower cost and utilize the swarm of vehicles.

[16] Fallon, M. F., Papadopoulos, G., and Leonard, J. J., 2010, "A Measurement Distribution Framework for Cooperative Navigation Using Multiple AUVs," *2010 IEEE International Conference on Robotics and Automation*, pp. 4256–4263.

In our new Acoustic Positioning system, called Swarm Long Baseline (SLBL), we will be triangulating the position of the underwater UUVs using the surface UUV's position from a GPS link. The SLBL scheme begins by sending scheduled acoustic pings from the surface UUV to the underwater UUV, where they record the time at which the signal was received. Each UUV has a hydrophone (to receive acoustic signals) and an acoustic projector (to send acoustic signals). Using the GPS data and the timestamp from this acoustic ping, we can triangulate the position of the underwater UUV, giving us precise positional data to be associated with the data gathered by the UUV. This data is used to perform track reconstruction of the specific underwater UUV, and that track data is then sent back to the other UUVs in the swarm if an anomaly is detected.

4.3.4 SLBL Fusion Scheme

Our SLBL scheme uses all three of the navigation techniques described above to reduce the error in position determination. Each UUV in the swarm is intended to be homogenous, with one hydrophone and one acoustic projector. Figure 43 shows an example of our SLBL scheme with one UUV for ease of explanation. Please note that the SLBL scheme is intended to scale with the size of the swarm, so multiple UUVs will be performing the operations shown.

The following is a description of the example shown in Figure 43: First, the swarm of UUVs are deployed with a synchronized ping schedule and downloaded navigation path. All UUVs record the GPS coordinates of their starting positions and relevant surrounding vehicles. Next, some of the UUVs remain on the surface (the 3 blue ones in this example) to send out pings on a synchronized schedule. The underwater UUV receives the acoustic pings from each surface vehicle and calculates relative range data (euclidean distance) by multiplying the one way travel time of the pings by the speed of sound in water (see "Navigation Math" in the Appendix). Each surface UUV sends out an acoustic ping with a distinct frequency. The underwater UUV is able to distinguish which pings come from which surface UUVs by the received frequency of the ping. The relative range data is mapped to the specific surface UUV that sent the ping and stored. This pinging cycle repeats until the underwater UUV comes up to the surface.

Once the underwater UUV surfaces, it sends relative range data mapped to each surface UUV to a home base of operation via Iridium satellite. The surface UUVs will also send their GPS location mapped to each time they sent out a ping to the home base. Home base will combine the data and perform track reconstruction for the UUV that has just surfaced to determine precisely where the UUV was when collecting data. Home base would then send back position data to the other surfaced UUVs in the

swarm if an anomaly was found along the reconstructed path. The surface UUVs are also intended to switch places with the underwater vehicles to allow the previously underwater vehicles to recharge via solar panels and to gather oxygen through the snorkel. Operating together in this way, multiple vehicles could precisely map out and measure large volumes without the need to regularly come to the surface to obtain a GPS fix and without the need for dedicated surface vehicles.

For the position calculations and signal flow diagram of our SLBL scheme, please refer to the Navigation Math section of the appendix.

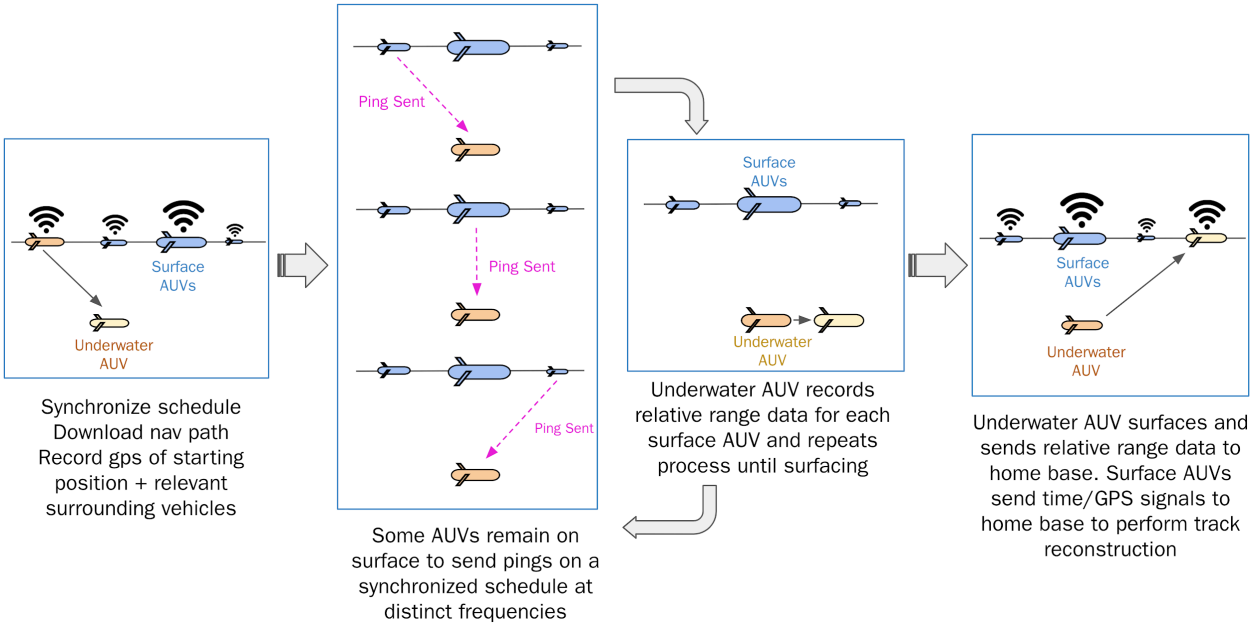

Figure 43: **SLBL Singe Vehicle Example.** This graphic depicts the process a single vehicle will go through in our SLBL scheme to allow for more accurate position determination. While this example only shows one UUV, this scheme is meant to be used with multiple in a swarm.

4.4 Communication

In order to control a swarm of vehicles, communication of information is a critical component in the larger scheme of operation. There are mainly three modes of communication: satellite communication via Iridium link, precise positioning via GPS, and short-range radio wave communication via WiFi.

When each UUV surfaces after its dive cycle, it establishes a connection with home base to transmit and download data through the Iridium link. At the same time, it will receive its absolute position through a GPS connection. WiFi communication is to be

used for short range communication. Since the vehicle must be completely sealed, vehicle initialization, programming, and data offloading will be done wirelessly via WiFi. Also, WiFi connection will serve as a fallback mode of direct communication between vehicles in case of malfunction in the Iridium link.

The communication links will be established through an antenna installed within the oxygen snorkel in order to ensure minimum contact with the ocean surface. As the snorkel extends to intake oxygen, communication connections will be established simultaneously.

Details regarding each mode of communication will be further elaborated in the respective subsections below.

4.4.1 Iridium

To lighten the computational load required for each vehicle, all data to be interpreted will be communicated back to home base. Afterwards, the processed data and new mission profile will then be sent to each vehicle via Iridium link.

Transmission of data from vehicle to home base will occur in two instances: after the vehicle has resurfaced, and prior to its next dive. After a vehicle has completed its dive, it will transmit the relevant information back to home base. The data package contains the IMU path of its dive; the time stamps of each received acoustic ping; time, position, and interest value of detected anomalies; its current status; and the GPS coordinates of its initial and final positions. As explained in Section 4.3.3, the time stamps of the acoustic pings will be matched with each source vehicle and compared with the IMU path to reconstruct the exact path of operation. The time and position of the detected anomaly will then be filtered with the calculated path, and the sampling map will be updated with its position and interest value.

The second transmission will occur before the next dive. While the vehicle is on the surface, it will operate as a source vehicle for acoustic positioning. With each ping, the vehicle will record its exact location and time. Before the vehicle initiates its dive, the data package containing the locations and timestamps of all transmitted pings will be uploaded to the home database for future mapping of pings received by other vehicles.

After the initial transmission of data is completed, the vehicle will begin downloading relevant data regarding its next dive. The mission profile of the next dive will be determined based on the updated sampling map. The new mission profile will include information on the path to take to explore a region of interest, the dive schedule, and

ping schedules of neighboring surface vehicles. The dive schedule will be allocated to ensure smooth transitioning of surface vehicles transmitting acoustic pings. This is to prevent possible gaps in regions where no surface vehicle can appropriately transmit the acoustic pings to nearby vehicles in operation. Since the ping schedules of all vehicles will be predetermined according to a time and frequency multiple access scheme, the pinging schedules of neighboring surface vehicles will serve as a reference for the vehicle to filter relevant pings. With a reference time frame to look out for acoustic pings from the surrounding surface vehicles, signals can be filtered from ambient noise, reflected signals, or irrelevant signals from faraway vehicles.

4.4.2 GPS

When the UUV surfaces, the vehicle will also establish a GPS connection. Through the connection, the vehicle will be able to record its global position in terms of longitude and latitude. Also, the internal clocks within the vehicle's microcontroller will be synced with the GPS signal. There are three cases in which the global position of the vehicle is to be recorded: the position of descent, position of ascent, positions of transmission of acoustic pings. All positions recorded will be transmitted to home base along with the time stamps via Iridium uplink.

In order to provide an exact reference for calculating the vehicle's path of operation, the GPS position of the start and end points of its dive are required. The positions of descent and ascent provide information for translating its travel path into absolute coordinates. The INS path data records the vehicle's movement from the beginning origin point. By inputting the GPS position of the initial point, the positions of the path can also be rendered in terms of global coordinates. Also, by comparing the final position of the IINS path and the actual position of ascent, the error rates can be computed to determine the margins of error for the positions of the vehicle underwater.

After the vehicle has surfaced, it will operate as a source of acoustic pings, transmitting the signals according to its predetermined schedule. At each instance of transmission, the vehicle must record its GPS position as a reference point for the vehicle underwater. While calculating an underwater vehicle's relative position will only require the distance traveled by the acoustic signal, in order to translate the relative position to absolute position, the GPS position of each ping's source is required.

Other than just obtaining the global coordinates, syncing the vehicle's internal clock is another key function of the GPS connection. Keeping an accurate track of time is integral especially for SLBL acoustic positioning since the vehicles will operate on a predetermined schedule. Furthermore, a precise record of transmitting and receiving

acoustic pings is required to calculate the distance traveled by each signal, and thus the position of the vehicle underwater. By synchronizing the internal clocks through GPS, the swarm can operate on the same temporal frame.

4.4.3 WiFi

WiFi connection is a mode of communication that will be mostly inactive during deployment. There are three cases in which WiFi will be utilized: as an alternative mode of communication in cases in which Iridium connection cannot be established, vehicle initialization prior to deployment, and data offloading after the vehicle returns to shore.

WiFi provides a fallback mode of communication in case of malfunction in a vehicle's Iridium link by allowing vehicles to communicate directly between each other. As an alternative short-range connection, the damaged vehicle will alert the surrounding vehicles of its status and position. With that information, the surrounding vehicles will then be able to notify home base for pickup via Iridium uplink.

Another use for WiFi communication is for users to communicate directly with the vehicle – vehicle initialization before deployment and offloading recorded data after returning to shore. While using wired signaling via LAN cable will allow such processes to be carried out faster, this method requires an opening breach in the vehicle's hull to access and connect to the vehicle's processor. However, considering the design of the hull to be perfectly sealed, using wireless communication was chosen instead. Before deployment, the basic information on the region of exploration, details of the swarm, required processes for operation, etc. will be downloaded. After retrieval, the observed data and relevant information that is saved internally will be offloaded.

4.6 Dynamics and control

The UUV is designed to be only controllable in its pitch and roll directions, with yaw achievable by coupling pitch and roll actuation in a banking motion. For this reason, the weight-shift control scheme is suitable for its intended use. RAPID used actuated fins and magnetic coupling to achieve elevation and turning control. We chose to move away from this design for three reasons. The first was to mechanically simplify the hull, which makes maintenance cheaper and simpler for long-endurance missions. The second was to reduce the number of custom-made coupling components, which are costly and labor-intensive to make. The third was to eliminate the need to puncture the pressure vessel. Because the primary vehicle hull cavity will be maintained at close to atmospheric pressure, it will need to withstand an enormous pressure differential. Eliminating as many areas as possible where components must penetrate through the

hull wall will help it maintain structural integrity longer and reduce hull manufacturing complexity.

Weight-shift control is a well-studied control scheme commonly used in the aviation space, particularly in hang gliders.[17] It allows for control of a vehicle's pitch and roll angles. By changing the position of the vehicle's center of gravity (CG), the offset between the gravitational force and the lift force creates a turning moment that allows the vehicle to bank to one side. See Figure 44. The simplicity of the design lies in the lack of control surfaces (such as rudders and elevators), unlike traditional aircraft control. When applied to the UUV, weight-shift control necessitates an actuatable center of mass in two dimensions, relative to the center of buoyancy and center of lift creates a moment on the vehicle. Each of the two dimensions allows the vehicle to pitch and roll respectively.

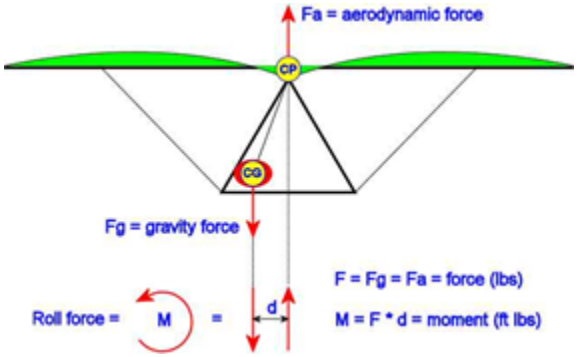

Figure 44: **Free body diagram illustrating forces acting on a weight-shifted hang glider.** Courtesy of Jeff Roberson.

The actuated mass mentioned above will be controlled using a Linear Quadratic Regulator (LQR) control algorithm. Given current positions, velocities, and accelerations from the path planning module, the LQR control algorithm is programmed to output the buoyancy force (adjustable by valves), the linear displacement of the mass (*delta_x* in Figure 45), and its tilting angle (*delta_gamma* in Figure 45). These inputs to the UUV (or the dynamical model of the vehicle in simulation) will result in net forces and moments to achieve the desired states. A high level overview of these input-output relationships is shown in Figure 45.

[17] 2008, "Weight-Shift Control Aircraft Flying Handbook, FAA-H-8083-5."

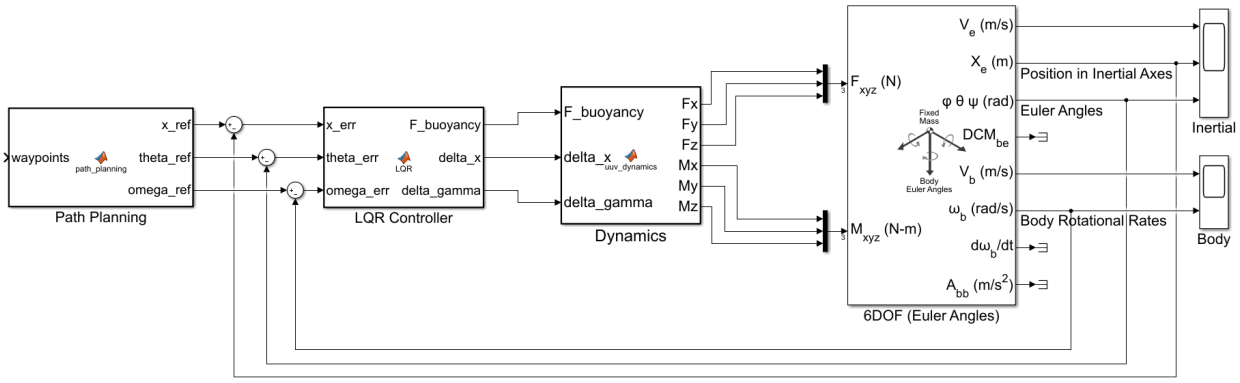

Figure 45: **System-level overview of the dynamics and control pipeline, constructed in Simulink.**

The UUV's control architecture can be categorized into three levels. On the low level, an LQR control scheme is used to actuate a mass, which controls the vehicle's pitch and roll angles, as mentioned above. The goal in this scheme is to match the vehicle's pitch and roll angles to the desired pitch and roll angles during turns. The medium level control entails waypoint commanding — given a destination, intermediate waypoint positions are generated along with the necessary velocities and accelerations, which are the inputs to the low-level LQR controller. Together, the two lower levels are used in the high level algorithm for swarm anomaly detection.

4.6.1 Control requirements

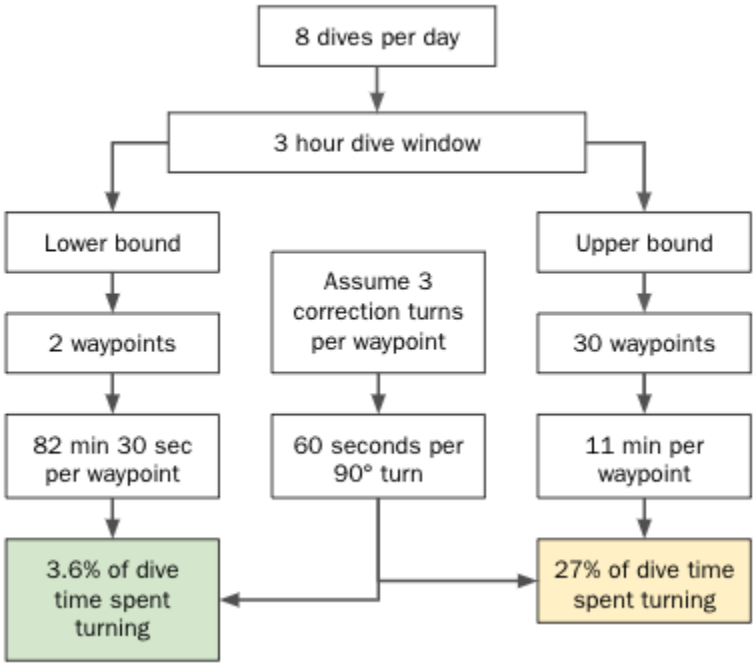

Figure 46: **Control requirement derivation.** A worst case dive profile with 30 waypoints to visit results in an upper bound of 27% of the dive time spent turning to navigate between waypoints.

Given an expectation of 8 dives per day over the 30 day mission, we derived a subsystem control requirement of 60 seconds per 90° turn in pitch or roll. Imposing an upper bound of 30 waypoints to be visited per vehicle per three hour dive allows for 11 minutes per waypoint. With an upper bound of three correction turns per waypoint trajectory, this requirement results in an absolute worst case of 27% of the dive time spent turning.

This 60 second turn requirement was extrapolated to define a requirement for angular acceleration, and subsequently, torque imposed by the weight-shifting mechanism. We can solve for α, angular acceleration, by integrating it over the 60 second turn window.

$$\int_0^{60}\int_0^{60} \alpha = \frac{\pi}{2} \tag{10}$$

$$\alpha = \frac{\pi}{3600} \tag{11}$$

This value of α can then be used to derive τ_{roll}, the amount of torque necessary to roll the vehicle 90° left or right. First, rotational inertia of the hull along its major axis can be determined.

$$I = \frac{1}{2}MR^2 \tag{12}$$

The rotational weight-shift mechanism must also be able to overcome the torque induced by lift of the wings as the vehicle rotates, τ_{lift}. $\rho$is the density of seawater, equal to $1000kg/m^3$, $v$is the linear velocity of the wings through the rotation, $C_L$is the lift coefficient of the wing, and $A$is the wing area.
Wing lift depends on these four variables.

$$F_{lift} = \frac{1}{2}C_L\rho v^2 A \tag{13}$$

$S$is the distance from the base of the wing to a given point on the wing. We can define $v_{rot}$and $A$from the wing geometry, where $W$is the width of the wing.

$$v_{rot} = \omega S \tag{14}$$

$$A = WdS \text{for a wing slice with length } dS \tag{15}$$

The lift coefficient can be approximated using the angle between $v_{forward}$and v_{rot}, θ Because $v_{forward} \gg v_{rot}$for the very small angular velocity needed to complete the rotation, we can make the approximation $sin(\theta_{apparent}) = \theta_{apparent}$. The lift coefficient subsequently can be determined.

$$C_L = 2\pi\theta_{apparent} \tag{16}$$
$$\theta_{apparent} = sin(\theta_{apparent}) = \frac{v_{rot}}{v_{forward}}$$

Substituting (14), (15) and (16) into Equation (13) gives us an expression for the lift force experienced by a wing slice with length dS. Integrating this over the length of the wing gives us the total resistive force of the wing.

$$F_{lift} = \int_0^L \frac{1}{2}2\pi\frac{v_{rot}}{v_{forward}}\rho(\omega S)^2 WdS \tag{17}$$

$$\tau_{lift} = F_{lift}\frac{L}{2} \tag{18}$$

This is the torque that the weight-shift controller must overcome in order to induce roll. Using Equations (12), the vehicle inertia, and (18), the resistive torque, we can determine τ_{roll}, the torque that must be imposed to complete a turn in 60 seconds.

(19)

Equation (17), τ_{lift}, evaluates to 8.203×10^{-7}N-m, almost negligible. The right-hand side of Equation (19), $I\alpha_{roll}$, evaluates to 0.0262 N-m. Even after adding τ_{lift}, τ_{roll}still evaluates to 0.0262 N-m. This value is our roll torque requirement: the amount of torque that must be generated along the vehicle's long axis to turn within the bounds of our performance requirements.

A similar derivation can be performed to obtain the torque requirement for pitch control. Vehicle inertia in this case must also account for the volume of water displaced through a given angle of rotation. $I_{vehicle}$along this axis is different.

$$I_{vehicle} = \frac{1}{12}ML^2 \tag{20}$$

$$I_{water} = \rho \int_{-L/2}^{L/2} x^2 \pi R^2 dx = \frac{1}{12}\pi\rho R^2 x^3 \tag{21}$$

A pitch control requirement of 90° in 60 seconds yields the same angular acceleration for pitch as for roll: $\alpha_{pitch} = \alpha_{roll}$. Using the combined inertia of the vehicle and displaced water, a pitch torque requirement can be derived.

$$\Sigma\tau = \tau_{pitch} = (I_{vehicle} + I_{water})\alpha_{pitch} \tag{22}$$

To meet this requirement, τ_{pitch}must be at least 0.1392 N-m. With a 3 kg battery, this only requires 4.64 cm of fore or aft displacement to turn nose-down or nose-up, respectively.

4.6.2 Weight-shifting hardware

The weight-shifting mechanism displaces the battery pack in order to generate pitch and roll torque. The battery pack is mounted between the two rails of the hull skeleton, and slides forward and aft in order to shift the vehicle's center of mass. Moving through its entire range of motion along these rails, the battery pack can shift the vehicle center of mass by 0.7 m in either direction. This fore-aft movement is driven by a motor and belt mounted on the rails. Lateral torque is generated by rotating the battery pack along its long axis, driven by a motor and planetary gear system mounted on the battery pack assembly. The battery pack's lateral center of mass is offset from the centerline by 1.5", allowing it to generate 0.1143 N-m in either direction. This maximum torque value sufficiently fulfills the roll torque requirement of 0.0262 N-m.

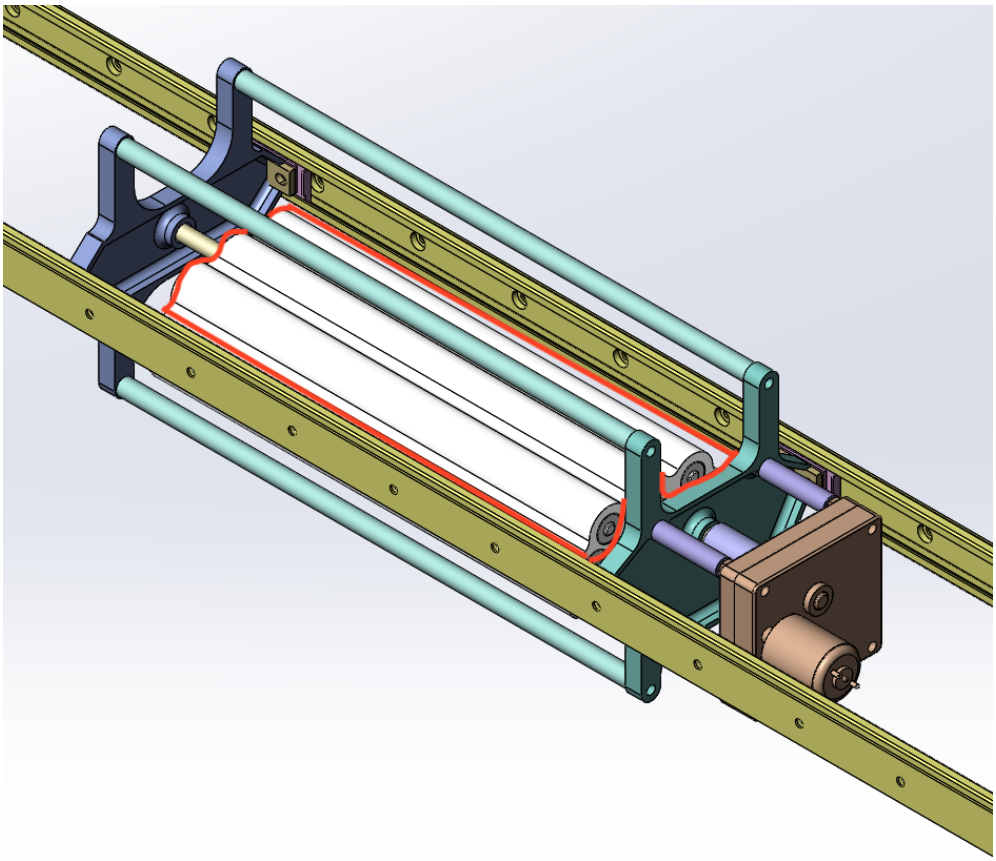

Figure 47: **Weight-shifting hardware configuration.** The battery, outlined in red, sits between the vehicle's two main skeleton rails, shown in yellow. It moves along these rails to control pitch, and rotates between them to control roll, driven by the motor visible at the end.

4.6.3 LQR pitch control

A Linear Quadratic Regulator (LQR) uses state-space representation for a system, which inherently implies that the system is modeled as linear. Specifically, for state vector **x**, input vector **u**, and system output **y**, we have equations

$$\dot{x} = Ax + Bu \quad (23)$$
$$y = Cx + Du \quad (24)$$

LQR is a type of optimal control scheme, optimizing for a cost function that takes into account system performance and control effort required, and making a tradeoff between the two. The cost function to be minimized is as follows,

$$J = \int_0^\infty (x^T Q x + u^T R u)\, dt \quad (25)$$

In the algorithm, the **Q** and **R** matrices penalize system output error and control effort, respectively. Since the UUV is designed for smooth trajectories with no stringent

response time requirements, the **R** matrix could be adjusted to directly penalize control effort, to conserve energy for achieving 30 day endurance for the vehicle. Penalizing control effort in this case translates to avoiding quick accelerations that cause the propeller to draw a lot of power. This would result in more relaxed trajectories and looser response time to input commands. Penalizing the Q matrix, conversely, pushes the vehicle to reach its target pitch or roll angle more quickly, potentially drawing more power. Implementation of LQR control seeks to balance these opposing goals.

The solution to this minimization problem is system gain, the **K** matrix. But in MATLAB, the system gain matrix could be found via the command $K = lqr(A, B, Q, R)$.[18]

4.6.4 Waypoint navigation

The swarm control and anomaly detection scheme described in Section 4.7 generates sequences of interest points that a designated vehicle must visit in its next dive. Navigating between two fixed points at depth presents a number of challenges, from the uncertainty in state estimation without GPS connectivity, to the variable nature of ocean currents that amplify state uncertainty. Furthermore, given the large turning radius of the vehicle, overshooting a trajectory can be a costly error, as it is time-consuming and inefficient to backtrack to a missed point.

The algorithm we will use for this control incorporates a number of solutions to these issues. It was designed as a control scheme for aircrafts flying in wind, but can easily be adapted to an underwater glider scenario by incorporating fluid and actuation parameters specific to our vehicle.

To account for the vehicle's large turning radius and slow maneuvering, the scheme incorporates a "look-ahead" distance, which tailors its current waypoint segment such that it passes its next waypoint at an angle conducive to reaching the following waypoint. Once the vehicle is within a set radius of its target waypoint, it begins to turn towards the next one. This parameter controls the balance between precision and smoothness of the trajectory. Relaxing it means the vehicle will not get as close to its goal waypoints, but will complete the trajectory faster and with less energy expenditure. Tightening it will result in greater positional accuracy at the cost of greater trajectory completion time and energy expenditure.[19]

---

[18] "Linear-Quadratic Regulator (LQR) Design." https://www.mathworks.com/help/control/ref/lqr.html.

[19] Osborne, J., and Rysdyk, R., "Waypoint Guidance for Small UAVs in Wind," *Infotech@Aerospace*, American Institute of Aeronautics and Astronautics.

As it was developed, this algorithm depends on regular GPS updates and wind speed estimates. Because neither of these are available underwater, the GPS position input will be replaced with the output of our IMU-based state estimator, as described in Section 4.3.1. Fluid velocity estimates will be pre-loaded on the vehicle using known data on global ocean current circulation before each dive. In non-tidal, offshore regions of the ocean, these velocities are nearly static for the mission durations considered for our vehicle. Even in tidal regions, current velocities and directions change predictably with each tide, so pre-loading this data would be simple.[20]

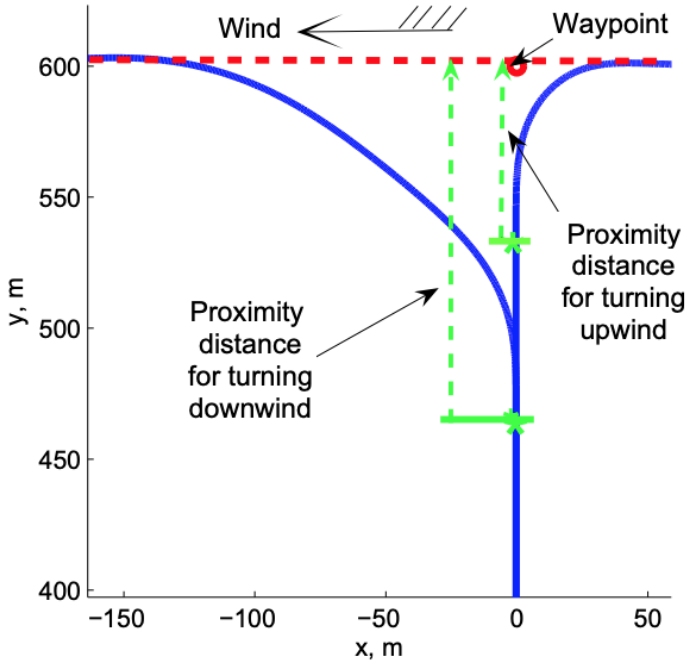

Figure 48: **Demonstration of look-ahead distance calculations in air.** These two trajectories are regulated by different look-ahead distances, stored in the lookup table. We can see that turning downstream requires a larger maximum look-ahead distance than turning upwind.

The algorithm also incorporates a lookup table, which increases performance in vehicles with actuation limits or low bandwidth command tracking. Inputs to the lookup table are initial course, desired course change, fluid speed and direction, and vehicle speed through water. The output is the “look ahead” distance necessary for maximum performance during course change. The table must be experimentally determined, either in simulation or in the field, for a particular vehicle, before it can be applied to mission scenarios.

[20] News, C. H., E&E, “Ocean Currents Are Speeding Up, Driven by Faster Winds,” Scientific American [Online].

4.6.5 Failure mode

In the event of a critical failure, a vehicle's only option is to surface as quickly as possible, as it cannot communicate directly with other vehicles or with the surface when it is at depth. As such, if a critical failure is detected, the vehicle enters a failure mode in which data collection stops and the buoyancy engine inflates to its maximum volume in order to ascend rapidly.

A critical failure is defined as any failure that threatens the lifespan of the vehicle–this includes valve failures, motor or board overheating, fluid leaking into the pressure hull, electrical shorting, and a multitude of other issues.

4.7 Swarm Control

Among many of the innovative advancements, one of the key advantages of DOUG is that the UUVs will be deployed in a swarm. While individual capabilities are limited due to reduced costs, as a swarm, multiple of these vehicles could efficiently explore, collect, and process data in a region of interest.

DOUG's operational scheme is largely based on RAPID. The end user defines the mission profile accordingly, downloads the relevant information onto each vehicle, deploys the swarm near the region of interest, and receives the collected data through either live updates via Iridium link or final offloading via WiFi after completion. Once deployed, each UUV explores and acquires data autonomously with the individual navigation, positioning, and control mechanisms elaborated in the above sections.

With each dive, the UUV collects the data to be processed offshore. After resurfacing, the UUV communicates with home base via Iridium link to transmit the raw collected data along with the received acoustic ping data for precise positioning. In order to reduce the computational load required from each vehicle, the data is only processed to detect anomalies by each vehicle and then collectively gathered at an offshore base. With the processed data, a map of the overall region is sampled according to interest value, and UUVs are directed to focus on the locations of high value. Interest values are calculated depending on the mission profile, whether it be an anomaly detection, a trend in data, or temporally changing effects. Through this continuous process of updating the mission operation, both widespread exploration of a region and detailed inspection of a location can be efficiently carried out.

4.7.1 Swarm Initialization

Prior to deployment, the end user determines a set of values to define the mission profile. The mission profile is then downloaded on each vehicle via WiFi. Depending on the purpose of the mission, the initialized mission profile may be customized to alter certain behavior of the swarm. Some of the values to be set are the following:[21]

- **Size of Swarm:** Number of vehicles deployed.
- **Region of Interest**: The region to be explored. The GPS coordinates of the region are meshed in three dimensions – longitude, latitude, and depth. Each node is represented by an interest value initialized at zero but to be updated throughout the mission. The spacing between nodes is defined by the spatial resolution value.
- **Depth:** While DOUG is designed to execute missions at depths up to 1000m, this value can be defined by the user for efficiency.
- **Spatial Resolution:** The distance between each spatial node. With higher spatial resolution, the region can be examined more thoroughly. However, that entails more accumulation of data per dive, presenting a tradeoff between duration of a single dive and sampling precision.
- **Maximum Node Visits:** Maximum number of times an UUV will visit the region near a spatial node.
- **Euclidean Distance Error:** The Euclidean distance bound that an UUV must be within in order to consider a node visited.
- **Acoustic Positioning Schedule:** The divided time schedule that designates which vehicle to be transmitting acoustic pings when on the surface. This schedule must be determined by the total number of deployed vehicles, the desired frequency of acoustic pinging, etc. In order to simplify the identification of the ping source, SLBL operates under a form of a Time Division Multiple Access scheme.
- **Acoustic Signal Frequency Assignment:** Each vehicle is assigned a unique frequency band or spectrum of chirp signals for acoustic pings to transmit. Along with the signaling schedule, a form of a Frequency Division Multiple Access scheme is also incorporated.

[21] Awale, S., Beeman, M., Bui, T., Correa, M., Fritzinger-Pittman, N., Gomes, C., Konuru, J., Li, S., Meyer, C., Neil, L., Paul, J., Pierre, J., Quenon, V., Raven, M., Sison, E., Smith, M., and Zheng, O, 2020, “R.A.P.I.D.”

4.7.2 Deployment

The swarm of UUVs will be deployed spread out at the region of interest by boat. Prior to activation, a number of UUVs will be initially designated to act as the surface vehicles for acoustic positioning while the rest will begin their dives. The exact number and scheduling of surface vehicles and underwater vehicles will depend on the swarm size, placement of vehicles, and acoustic pinging schedule. After the UUVs are deployed at the appropriate positions, they will be in an idle state, waiting for an activation ping transmitted via Iridium link.

4.7.3 Operating Modes

The UUVs operate under two modes: surface mode and underwater mode.

When the UUV is on the surface, it will be in 'surface mode.' In surface mode, the UUV will transmit and download data via Iridium link, receive its position via GPS, recharge the fuel cell, flush the buoyancy engine, and transmit acoustic pings according to the ping schedule. Before entering underwater mode, the UUV will download the updated sampling map of the region to determine its next dive.

'Underwater mode' refers to the main operating mode of the UUV. In underwater mode, the UUV will explore the spatial nodes in the region of interest according to a path based on a value priority queue while passively listening for acoustics pings. The value priority queue is determined by the interest values assigned to the nodes based on collected data, the distance from the nodes, and the distance of other UUVs to the nodes. All of this data will be available from the downloaded sampling map. The exact function of incorporating these values to determine the priority queue has not yet been decided.

As the UUV explores the nodes according to its decided path of waypoints, it will begin to collect data. If an anomaly has been detected along its path, it will record the time of detection and approximate position. This information will later be matched with the traveled path of the vehicle calculated with SLBL to find the exact position of the detected anomaly. Depending on the swarm anomaly response behavior, the UUV will either resurface immediately, entering surface mode, or continue its operation until the end of its dive cycle. The collected data will be stored until transmission in surface mode or complete offloading post mission.

Also, in underwater mode, the UUV will be passively listening for acoustic pings. Once a ping has been received, the UUV will store the timestamp of each reception. Since

the transmission schedule of surrounding surface vehicles is predefined, the UUV only needs to look out for pings within a reasonable time window. All of the stored timestamps of received acoustic pings will be transmitted to home base and matched with the appropriate surface vehicles to reconstruct its path.

4.7.4 Mission

The continuous switching between surface and underwater mode results in a cyclic process of collecting data, calculating its traveled path with SLBL, updating interest values of spatial nodes in the sampled map, determining its next path based on the value priority queue, and proceeding to its next dive.

To illustrate this, an example scenario with a simplified 3x3x3 grid is shown below. For the sake of visual clarity, the first 3x3 grid is not shown. A bird's eye view of the surface plane will show the positions of the vehicles as well.

For reference, the vehicles in blue represent vehicles in surface mode, and the vehicles in tan represent vehicles in underwater mode. Red circles represent spatial nodes with interest values assigned to each node.

The UUVs are initially deployed around the region of interest. Each spatial node is initialized with interest values of zero.

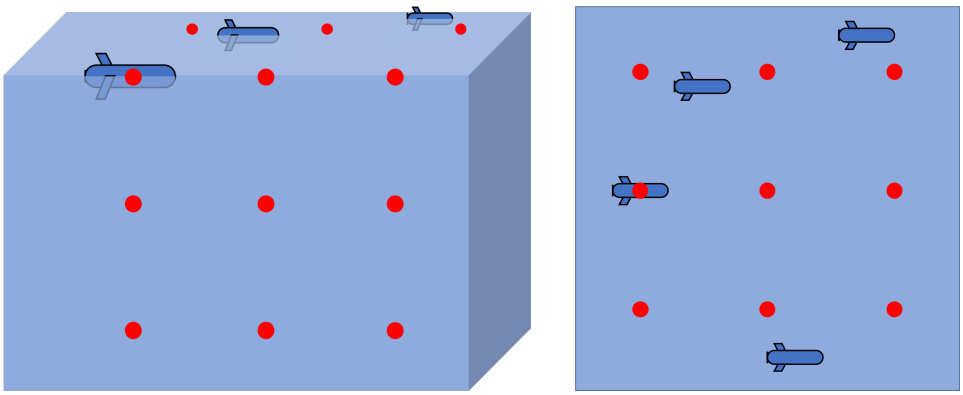

Figure 49: **Initial Deployment.** UUVs are deployed in a region of interest where spatial nodes have initial interest values of zero.

Two of the UUVs are initially designated as surface vehicles, while two UUVs will begin their dive operations. Since the nodes are all of equal value, the initial paths are determined to explore regions in which no UUV has been deployed. The UUV in the back (top right in the top view) will move into the page. The UUV in the left center of the grid moves to the right. The black line represents the path that the vehicle travelled.

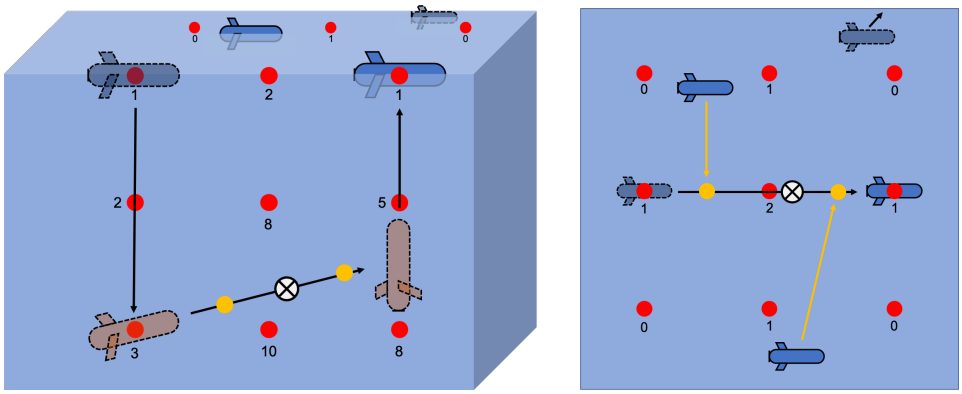

Figure 50: **Initial Steps of DOUG.** The UUVs carry out their operations. The sampled map updates the interest values based on collected data and anomalies, depicted as a circle with an X.

In this example scenario, the UUV detects an anomaly, represented by the circle with an X. After this UUV has resurfaced, it will enter surface mode to transmit the collected data. After processing the collected data, an interest value of 10 is assigned to the closest spatial node to the anomaly point, and the remaining nodes are assigned values computed from the data collected. The nodes have been assigned interest values depending on the distance from the anomaly point in this case. During its dive, the UUV receives one acoustic ping from each of the neighboring vehicles. The yellow circle represents the position at which acoustic pings were received, and the yellow arrows represent the transmission of an acoustic ping from a surface vehicle. This data is used to pinpoint the location of the anomaly in the vehicle's path.

With the updated sample map, the next UUV on the top left determines its path to explore the region of high interest value nodes. In this case, it will dive, moving out of the page to the bottom right corner and resurface. After the vehicle has resurfaced, the collected data will be transmitted back to base to be processed, and the sample map will be updated again. Once the maximum number of visits allowed for a spatial node has been reached, the UUVs will move to explore another area.

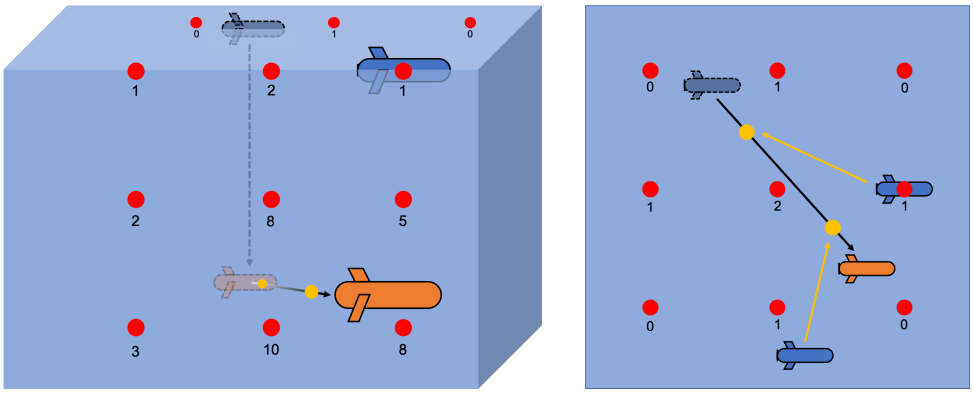

Figure 51: **Continued Exploration.** Based on the updated sampling map, UUVs determine the waypoints of next dives.

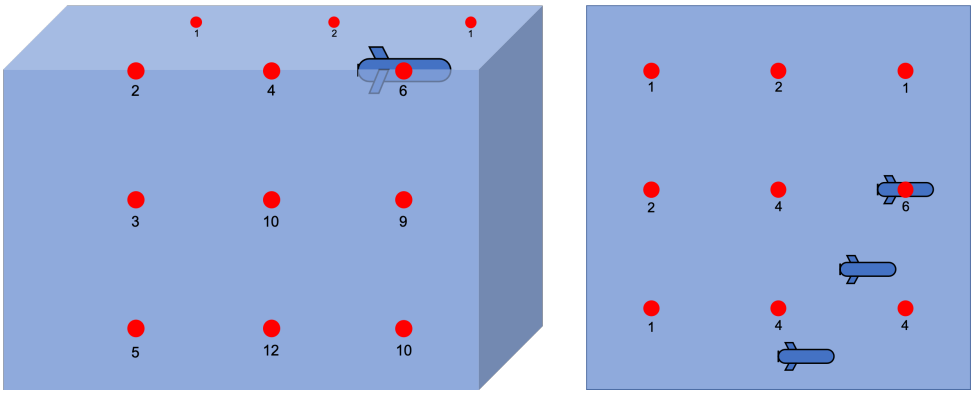

Figure 52: **Updated Map with Updated Interest Values.**

This sequence of operation will continue until the entire region of interest has been explored.

5 Electronics

This section highlights the specific electronics we have chosen for our UUV design to enable it to meet the system requirements, independently navigate, find anomalies, and work with the swarm. It also shows how each component will be connected to the overall Electrical System and provides a detailed description of each component.

5.1 Electronics system requirements

- State estimation within ~20m
- Transmit collected data
- Operating depth of 1000m
- Communicate to converge on areas of interest
- 30 day minimum endurance

5.2 System overview

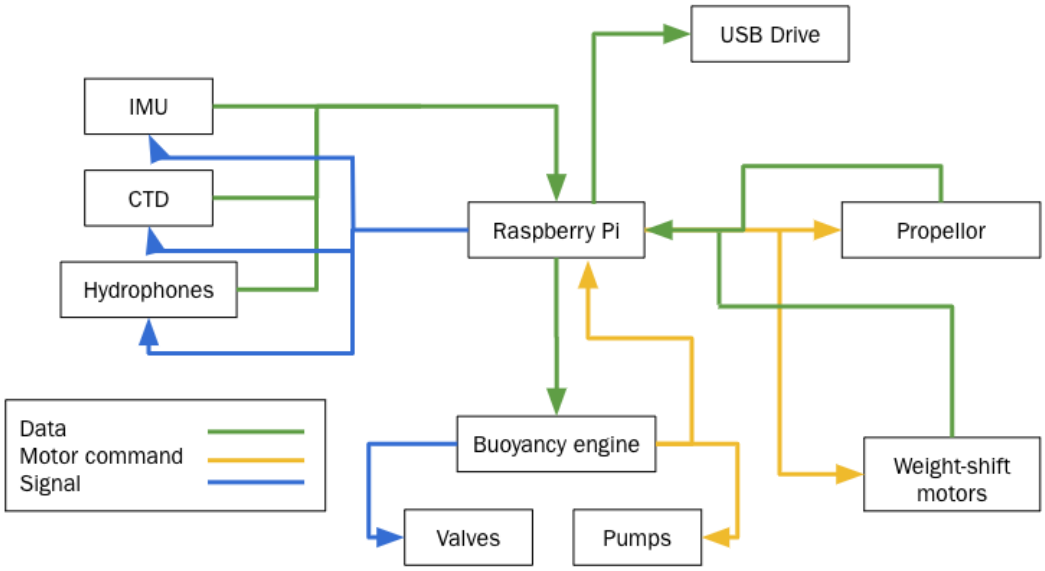

Figure 53: **Data & signal connectivity overview schematic.** The Raspberry Pi is responsible for all data, signal and motor commands across the vehicle, as abstracted here. Sensors report back data to the controller, which processes it and offloads it to data storage. Motors like those in the propellor, buoyancy engine and weight-shift controller report their back-EMF to the controller. These values are used in motor control feedback.

The electronics package was designed to be low-cost and able to handle long-term changes to the sensor package or other modules. Given the current sensor load, the

system data bandwidth is considerably small and could handle the addition of a SONAR, fluorometer, <2k resolution camera, or other sensor. The controller also runs control algorithms for all the motors onboard, using their back-EMF signals as control inputs, regulating buoyancy, pitch, roll and forward velocity.

5.3 Controller & electronics package

This section goes through the tasks and technical details of the Controller, IMU, GPS, Iridium Uplink, Projector, Hydrophone, and CTD. These components allow each vehicle to use a swarm sampling method and operate autonomously on long-endurance missions.

5.3.1 Controller

The Controller, whose selection method is shown below in Figure 54, is a microprocessor which:

- Controls the other electronics
- Stores data from sensors onto a microSD card
- Estimates the current position using IMU data
- Plans autonomous navigation
- Prepares outgoing communications
- Processes received communications

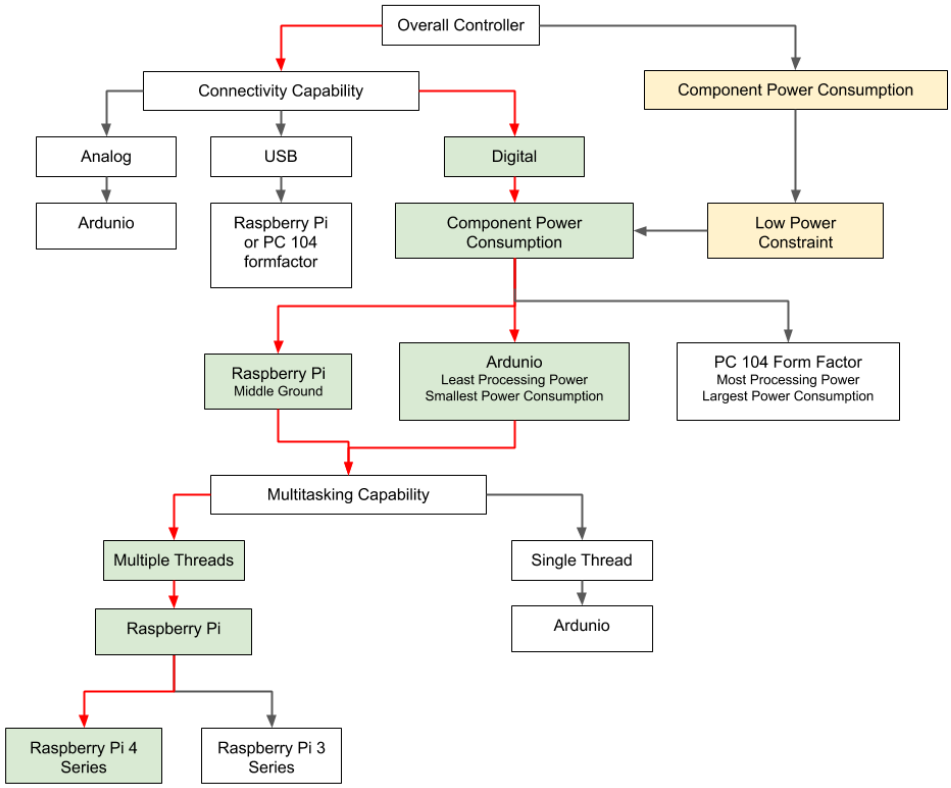

Figure 54: **Controller Decision Tree.** This shows a brief explanation of how the Raspberry Pi 4 Model B was chosen.

All of the current peripheral devices used can be interfaced with digital signals which all 3 of the potential controller categories have. While the maximum theoretical power consumption of the Raspberry Pi is about the same as that of the PC 104 form factor options, the average power of PC 104 options are much higher and comparable with the Raspberry Pi's typical tested maximum. PC 104's minimum power is also much higher with no data points below 2 W compared to most Raspberry Pi models being well under 1 W. This narrowed the choices to the Raspberry Pi and the Arduino, but the Ardunio was eliminated since it would not be able to handle simultaneous calculations and processes due to the single threaded nature of most common Arduino models. Between the 3 and 4 series Raspberry Pi models, the 4, shown in Figure 55, was chosen due to its increased native connectivity options on the 40 pin GPIO header as shown in the Appendix.

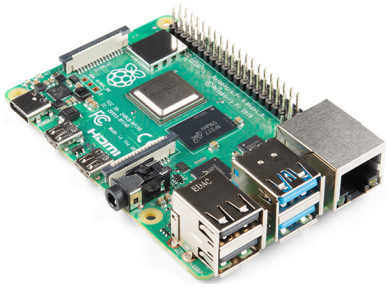

Figure 55: **Raspberry Pi 4 Model B.** Dimensions (in): 3.4 x 2.2 x 0.8, Mass (lb): 0.1.[22]

The Raspberry Pi 4 Model B has 40 GPIO pins and is capable of having up to 6 I2C connections, 6 UART connections, 5 SPI connections, and 2 PWM connections.[23] Additional connectivity includes 4 USB connections, a micro SD card slot, and 1 Gigabit Ethernet connection with Power over Ethernet (PoE). For a complete list of connectivity options see the appendix. The communication methods used in this case include:

I2C

1. GPS
2. IMU
3. Iridium

Serial

1. CTD

It can communicate wirelessly over 2.4 GHz and 5.0 GHz IEEE 802.11ac wifi and Bluetooth 5.0 BLE. These communication methods can be used for programming UUVs before a mission, but the range will be limited.

Data storage is handled by a microSDHC card. A Raspberry Pi has been tested to accept at least up to a 400 GB microSD card. A Samsung PRO Endurance 32 GB Class 10 module was chosen due to its durability, low cost, and being tested to work with the Raspberry Pi.[24] This microSD card is designed mainly for video surveillance and has been tested to have resistance to magnets and x-rays, is rated for -25°C to 85°C, can record continuously for up to 5 years, and can survive up to 72 hours in seawater.[25] These capabilities will give data from a lost or breached UUV a higher chance of being recoverable. This module is also currently available in capacities up to

---

[22] "Raspberry Pi 4 Model B (4 GB) - DEV-15447 - SparkFun Electronics" [Online]. Available: https://www.sparkfun.com/products/15447.

[23] "Raspberry Pi 4 Model B Datasheet." Available: https://www.raspberrypi.org/documentation/hardware/raspberrypi/bcm2711/rpi_DATA_2711_1p0_preliminary.pdf.

[24] "Best MicroSD Cards for Raspberry Pi," Tom's Hardware [Online]. Available: https://www.tomshardware.com/best-picks/raspberry-pi-microsd-cards.

[25] "MicroSDHC PRO Endurance Memory Card w Adapter 32GB Memory & Storage - MB-MJ32GA/AM | Samsung US," Samsung Electronics America [Online]. Available: https://www.samsung.com/us/computing/memory-storage/memory-cards/microsdhc-pro-endurance-memory-card-w-adapter-32gb-mb-mj32ga-am/.

128 GB to accommodate future upgrades or additional sensors such as a camera. The 32 GB capacity was chosen for this version due to its lower cost and lower power consumption. This module has a maximum write speed of 30 MB/s which easily accommodates the current version's peak estimated data generation rate of around 1 KB/s with a safety factor of about 30,000.

The maximum power consumption of the Raspberry Pi 4 Model B is about 3 A at 5.1 V or about 15.3W, but the actual power consumption will be lower and variable. Power consumption will change depending on the load placed on the CPU and the power needed for peripherals. Power saving measures that can be taken include only turning on wireless connectivity when programming on the surface, turning off diagnostic LEDs, reallocating RAM to the CPU to lower GPU usage, and underclocking the CPU once the actual CPU load is known.

5.3.2 IMU

The IMU shown in Figure 56[26] is for:

- Estimating the UUV's current position
- Estimating the UUV's position at the time of an acoustic ping
- Approximating the path the UUV took between GPS pings
- Time keeping

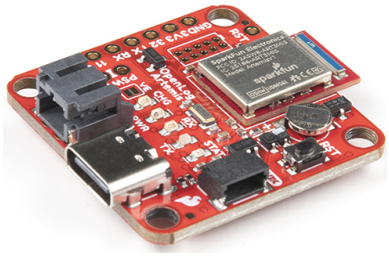

Figure 56: **SparkFun OpenLog Artemis.** Dimensions (in): 1.3 x 1.3 x 0.3, Mass (lb): 0.02.[27]

This 9DoF IMU can record as fast as 250 Hz and uses a gyroscope, 3-axis accelerometer, and magnetometer to track the UUV's position, orientation, and heading.[28] Compared to IMU's usually put into UUV's this is relatively cheap and

---

[26] "SparkFun OpenLog Artemis - DEV-16832 - SparkFun Electronics" [Online]. Available: https://www.sparkfun.com/products/16832.

[27] Awale, S., Beeman, M., Bui, T., Correa, M., Fritzinger-Pittman, N., Gomes, C., Konuru, J., Li, S., Meyer, C., Neil, L., Paul, J., Pierre, J., Quenon, V., Raven, M., Sison, E., Smith, M., and Zheng, O, 2020, "R.A.P.I.D."

[28] "SparkFun OpenLog Artemis - DEV-16832 - SparkFun Electronics" [Online]. Available: https://www.sparkfun.com/products/16832.

inaccurate, but its data will be combined with the GPS measurements from when it is on the surface and the position estimations from the acoustic pinging method to increase accuracy.

This IMU communicates with the controller using I2C and comes with a Real Time Clock (RTC) which can be used by the controller to keep time.[29] It can be put into a sleep mode with a power consumption as low as 59.4 μA, but normal power consumption is around 0.01 W.[30]

5.3.3 GPS

The GPS shown in Figure 57[31] is for:

- Accurately measuring UUV position when on the surface
- Accurately measuring the position of surface UUVs when they send a ping

Figure 57: **SparkFun NEO-M8P-2 Qwicc.** Includes the Board, Base plate, and Antenna. Dimensions (in): 1.6 x 1.3 x 0.2, Mass (lb): 0.01.[32]

The GPS interfaces with the Controller using I2C, generates about 90 Bytes of data per sample, and consumes an average of around 0.1W while on [6, 7]. It also includes an optional backup battery which can be used to decrease the time-to-first-fix to as little as 1 second. While it can report its location as accurately as within 1 inch, on the ocean it will likely be limited to reporting as accurately as within 8 feet.[33]

---

[29] *Ibid*

[30] Awale, S., Beeman, M., Bui, T., Correa, M., Fritzinger-Pittman, N., Gomes, C., Konuru, J., Li, S., Meyer, C., Neil, L., Paul, J., Pierre, J., Quenon, V., Raven, M., Sison, E., Smith, M., and Zheng, O, 2020, "R.A.P.I.D."

[31] *Ibid*

[32] "SparkFun GPS-RTK Board - NEO-M8P-2 (Qwiic) - GPS-15005 - SparkFun Electronics" [Online]. Available: https://www.sparkfun.com/products/15005.

[33] *Ibid*

5.3.4 Iridium uplink

The Iridium shown in Figure 58[34] is for:

- Sending data to be processed
- Receiving new orders
- Resyncing the clock

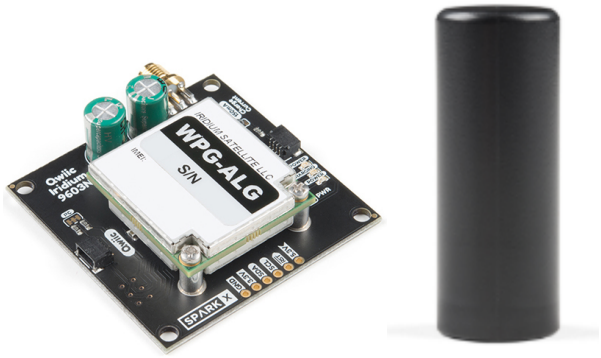

Figure 58: **Qwiic Iridium 9603N.** Includes the Board (Dimensions (in): 2.4 x 2.1 x 0.6) and Antenna (Dimensions (in): 1.9 x 0.7 diameter) [8, 9]. Overall Mass (lb): 0.1.[35]

The Iridium enables satellite communication for data transfer whenever there is no obstruction in the line of sight between the antenna and satellite. It communicates with the Controller using an I2C connection and consumes an average of 0.5W of power while active. The antenna has an IP-67 rating.[36] Iridium communication does have an upkeep cost of about $15 per month of use.[37]

5.3.5 Projector

At the time of publication of this white paper, we are still in communication with a supplier regarding which projector is best for our system. We anticipate being able to choose and source a compatible projector by December of 2020.

---

[34] "Qwiic Iridium 9603N - SPX-16394 - SparkFun Electronics" [Online]. Available: https://www.sparkfun.com/products/16394.

[35] Awale, S., Beeman, M., Bui, T., Correa, M., Fritzinger-Pittman, N., Gomes, C., Konuru, J., Li, S., Meyer, C., Neil, L., Paul, J., Pierre, J., Quenon, V., Raven, M., Sison, E., Smith, M., and Zheng, O, 2020, "R.A.P.I.D."

[36] "Qwiic Iridium 9603N - SPX-16394 - SparkFun Electronics" [Online]. Available: https://www.sparkfun.com/products/16394.

[37] "RockBLOCK 9603 | Rock Seven" [Online]. Available: https://www.rock7.com/products/rockblock-9603-compact-plug-play-satellite-transmitter.

5.3.6 Hydrophone

The Hydrophone shown in Figure 59 is for:

- Receiving signals from the projector

Figure 59: **SQ26-01 Hydrophone.** Dimensions (in): 1 x 1 diameter, Mass (lb): 0.04.[38]

This Hydrophone is rated for a max depth of 2,000m, a safety factor of 2. The SQ26-01 can operate in a versatile range of frequencies (.001 to 28 kHz), making it a valuable sensor as we plan on incorporating multiple signals across multiple ranges. It can also operate in many different environments, with a temperature range of -30 to 60 degrees Celsius.[39]

[38] Olsen, J., "Sensor Technology SQ26-01 Hydrophone - Research Hydrophones," Cetacean Research Technology [Online]. Available: https://www.cetaceanresearch.com/hydrophones/sq26-01-hydrophone/index.html.
[39] *Ibid*

5.3.7 CTD

The CTD shown in Figure 60 is for:

- Profiling the ocean
- Finding anomalies
- Estimating the speed of sound in the area

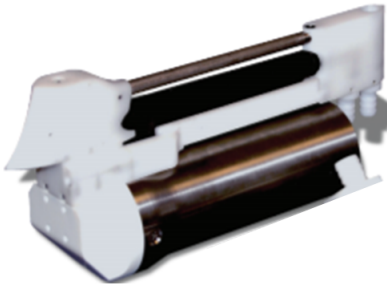

Figure 60: **Seabird Glider Payload CTD.** Dimensions (in): 10.1 x 4.6 x 2.5, Mass (lb): 2.6.[40]

This CTD is an accurate low-power model designed for autonomous underwater gliders and rated for depths up to 1500m, a safety factor of 1.5. It consumes around 0.2 W, communicates with the controller using a serial interface, generates about 41.2 KB of data per hour, and has a real-time output mode.[41] While the software is Windows only, since only a few commands are needed it is theoretically possible to hardcode the signals that need to be sent to initiate those commands.

[40] "Glider Payload CTD (GPCTD) | Sea-Bird Scientific - Overview | Sea-Bird" [Online]. Available: https://www.seabird.com/moving-platform/glider-payload-ctd-gpctd/family?productCategoryId=54627473789.
[41] *Ibid*

6 Structures

The structure of the UUV was designed to perform as a pressure vessel and seal off the majority of the subsystems from the sea water environment. Initial sizing was taken from RAPID and iterated upon to insure a robust design fulfilled all design requirements. Different from RAPID, the structure now includes frames (ribs) to improve upon buckling capability and supports the added equipment needed to perform its mission.

6.1 Structures System Requirements

Table 15 provides an overview of the system requirements for the vehicle's structural components. These requirements are primarily driven by the ocean environment and the goal of deploying the vehicle as inexpensively as possible.

A maximum depth of 1000 m was specified by sponsors at the start of the project. At this depth, external pressure is approximately 10 MPa and the density of seawater is approximately 1033 kg/m3. Any components in contact with seawater must handle this pressure gradient without failing. The vehicle should be positively buoyant (or neutrally buoyant, at minimum) while at depth to ensure it can be recovered in case of major failures.

To help minimize the overall cost of the vehicle, we specified an overall maximum manufacturing cost of $50,000 and a maximum weight of 80 kg. Our goal for this vehicle was to have a lower cost than RAPID's $50,000 manufacturing cost. Our preliminary research revealed that deployment cost increased drastically for a vehicle over 80 kg due to the need for a lift and other heavy machinery. A vehicle under 80 kg can be simply lifted into the water by two people.

Requirement	Value	Reasoning
Maximum External Pressure	10 MPa	Sponsors require 1000 m depth capability
Weight	80 kg	Enables 2-person deployment
Cost	$50k	Achieve lower cost than RAPID
Average Density at Depth	1033 kg/ m3	Prevent sinking if vehicle fails at depth

Table 15: **Design requirements relevant to structures subsystem.**

6.2 System Overview

6.2.1 Hull Layout

The hull consists of a 8”OD x 7.5” ID x 72” 6061-T6 aluminum tube with 6061-T6 aluminum ribs arranged throughout the central portion to stiffen the structure against buckling/collapse at depth as well as reduce overall vehicle compression. Overall the hull weighs approximately 30 kg. Two end caps seal either end with a simple set of o-ring grooves and a handful of set screws to secure them.

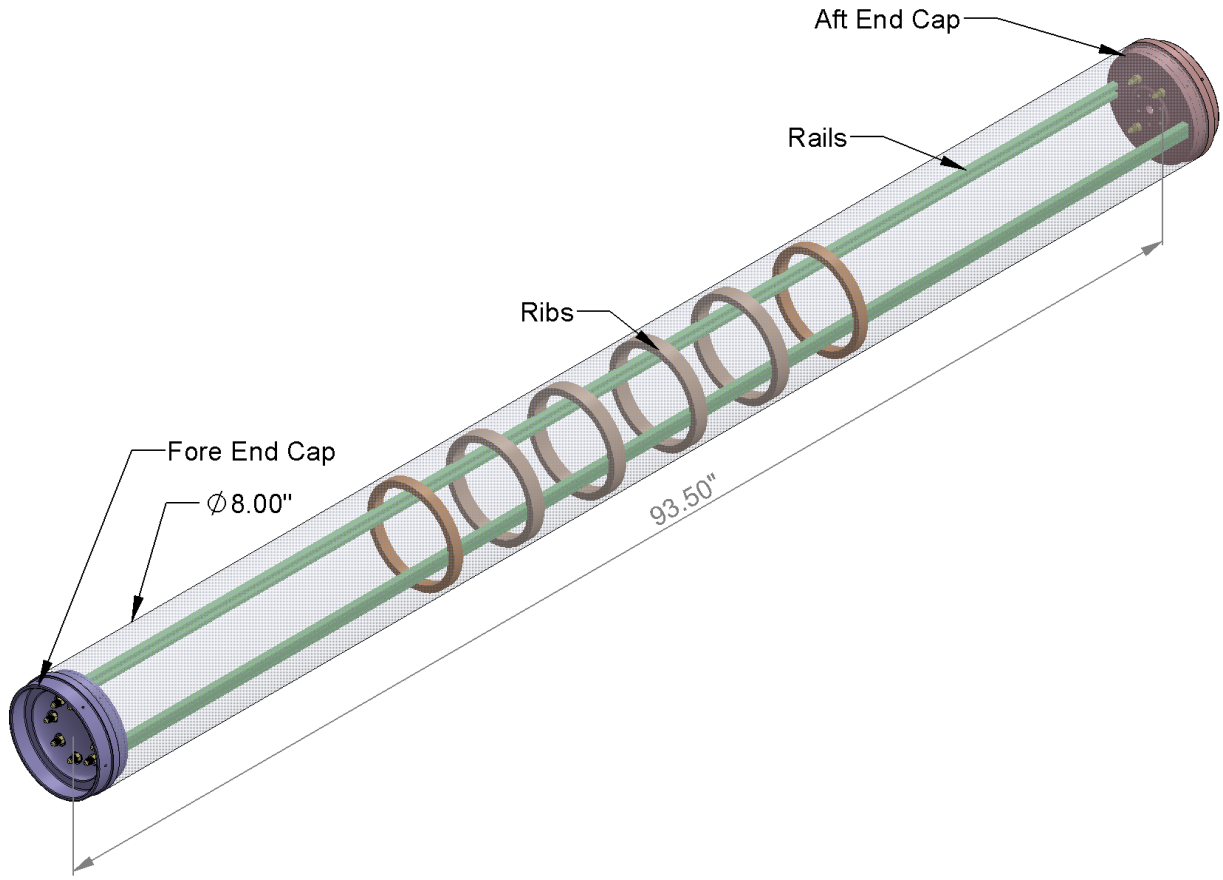

Figure 61: **Overall hull design.** The six rings near the center are the ribs which are all notched to help support the rails pictured at either side.

Components are mounted and spaced within the hull using a skeletal structure consisting of a pair of extruded aluminum rails. The rails themselves are supported by slight notches or features in the ribs as well as by the end caps, the intent being that it should be relatively easy to slide out the entire set of internals of a system in order to assemble/disassemble them, perform maintenance, and swap out components. Having better accessibility and more universal mounting of internal components is also

intended to yield higher modularity of the vehicle as a whole, as sensor packages and operational groups within the vehicle may be shifted, modified, and replaced with ease. Component mounts and individual cross braces will help stiffen the overall structure. The overall hull was designed to either use inexpensive off the shelf parts or be relatively easy to manufacture in house using a CNC mill or lathe.

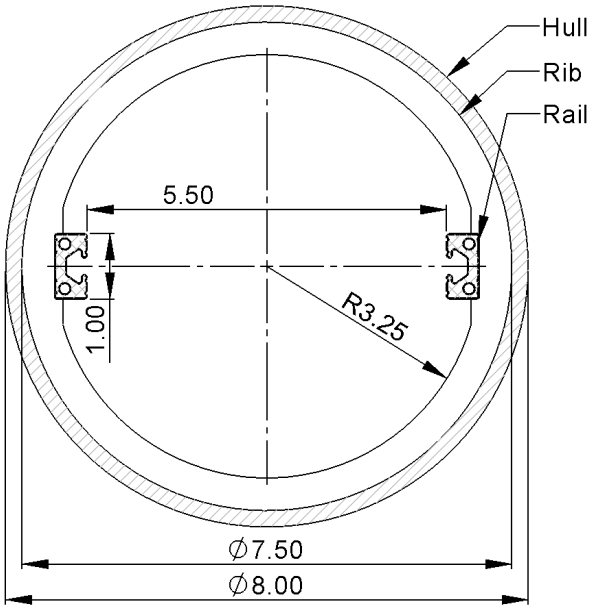

Figure 62: **Cross sectional view of the hull.** With the ribbing the space to package components narrows down roughly to a 6.5” diameter circle with side mount points at 5.5” apart.

Each component in the hull’s assembly is specified as aluminum 6061-T6. Aluminum was chosen for its relatively high strength to weight ratio (since we are interested in maintaining a lighter and potentially easier to deploy package), for its ease of manufacture, and for its comparatively low price point. The specific 6061-T6 alloy and temper was specified since it is one of the most widely available and versatile, for instance most of the metal suppliers we checked with only regularly stock 8” OD aluminum tubes in 6061-T6. We would recommend spending more time investigating different supplier options.

6.2.1 Material Selection

The criteria for material selection was cost, weight, corrosion resilience, and strength. Initial materials considered were 2000, 5000, and 6000 series aluminums, 316 class stainless steel, glass and carbon fiber composites, and both ABS and HDPE plastics. The down selected material was chosen to be 6061-T6 aluminum.

Initial first order cost of raw and preformed materials was calculated using procurement cost for various internet sources. Physical and tensile properties of these materials are available from literature and internet sources. Corrosion resilience was determined using the anodic and cathodic material properties found in the United States Naval Aviation Cleaning and Corrosion Control Manual (NA-01-1A-509-1) and shown in Figure 63.[42] Using a single material reduces the potential for corrosion to deteriorate the hull.

[42] "NAVAIR 01-1A-509-1 NAVAIR CLEANING CORROSION CONTROL" [Online]. Available: http://everyspec.com/USN/NAVAIR/NAVAIR_01-1A-509-1_8121/.

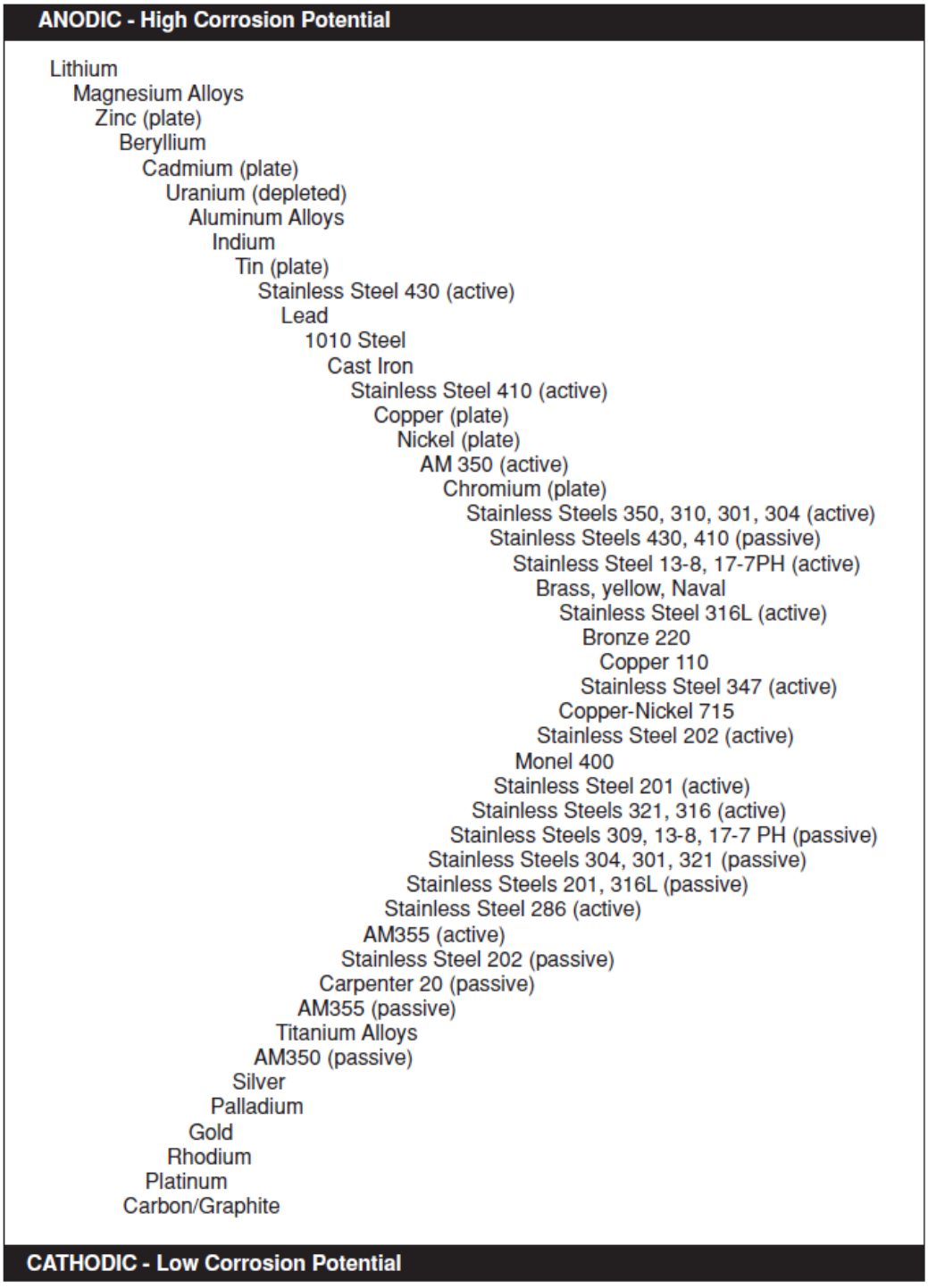

Figure 63: NA-01-1A-509-1 **Anodic and Cathodic** materials chart. When using anodic and cathodic materials the potential for corrosion can be limited by selecting materials that are near each other from this chart.

6.3 Ribbed Hull

6.3.1 Sizing Constraints

Our team down-selected a semi-monocoque design to reduce weight and improve buckling capability. The hull design uses 72-inch-long, 8-inch outer diameter, 0.25-inch wall thickness aluminum tubing reinforced with 6, 0.5 x 0.5-inch aluminum frames (ribs). The frames are equally spaced from each other and are located only on the center two-thirds of the hull to reduce overall weight.

Since ductile materials, such as aluminum, do not typically fail in compression (due to excessive straining) we decided to focus on buckling capability while ensuring no plastic deformation at our design depth.[43] Due to the nonlinear nature of buckling failure, we built finite element models of the cylindrical hull with nonlinear geometry and material properties. The model had a ramped pressure load equal to approximately 2x the operating pressure to determine how much capability the structure had beyond the expected operating depth.

This initial study demonstrated that a 0.25 inch aluminum tube at a 65 inch length met both our requirements: it did not buckle at 1.5 times the operating pressure and showed no plastic deformation at the operating pressure. However, upon further research, we identified one downside to designing structures as monocoque cylindrical tubes is their susceptibility to manufacturing imperfections. One pressure vessel design reference suggests a 1.5 plasticity knockdown factor on a linear buckling hand calculation.[44] This knockdown factor is based on several data sets which correlated linear buckling predictions to cylinder buckling test data. Based on this methodology, the hull thickness would need to increase to greater than 0.5 inches to maintain the required safety factors.

Furthermore, to confirm this susceptibility, we ran a buckling analysis with the same setup as previously mentioned with the only exception being the initial geometry. The input geometry represented an imperfect cylinder and its shape imitated the first eigenvalue buckling mode, but the deformation magnitude was within manufacturing tolerances of a cylindrical tube. Details about this analysis are in the appendix. This study solidified the plasticity factor design methodology and showed with a defect within manufacturing tolerances, the 0.25 inch hull would buckle at a pressure equivalent to half of our required operating depth which was about a 75% decrease in

---

[43] Tseng, W. J., “Chapter 4: Other Tests of Plastic Behavior,” p. 11. Available: http://audi.nchu.edu.tw/~wenjea/mechanical103/Chapter_4.pdf.

[44] Ross, C., Bowler, T., and Little, A., 2009, “Collapse of Geometrically Imperfect Stainless Steel Tubes under External Hydrostatic Pressure,” Journal of Physics: Conference Series, **181**, p. 012030.

overall capability compared to a perfect cylinder. However, increasing the hull thickness to 0.5” to meet the buckling requirements was not viewed as a possible design path due to the associated 2x weight penalty.

This hefty weight penalty drove us to explore two alternate concepts: a rib-reinforced shell and a corrugated design. Due to manufacturing complexity, we tabled the corrugated design and details regarding that configuration are in the appendix.

6.3.2 Hull Costs

Material and machining costs for the semi-monocoque design are estimated to be 5000.00 USD. 451.64 dollars for the 72inch length of 8inch OD/7.5 in ID tubing. 533.43 dollars 12 inch long 8inch diameter rod to be machine down to make 6 ribs and 2 end caps. As a first order rule of thumb, typical machining cost for parts of this complexity is approximately 7.5x the raw material cost.

6.3.3 Finite Element Analysis

3D Finite Element Analysis (FEA) Modeling was performed using ANSYS Workbench Academic Student version 2020 R2. FEA model used geometry imported from the CAD model using only the hull, frames and end caps as there are the only load bearing members. Non-linear material properties (elastic-plastic) of 6061-T6 aluminum are included in ANSYS model and pressure associated from the operating depth reacting all exterior surfaces was used. Boundary conditions allowed for unrestricted growth of the model by only fixing one node that is the front of the model in the 6 degrees of freedom. The frames and end caps were modeled using “bonded” contacts to keep the joining surfaces in contact without relative motion. Figure 64 shows the elastic-plastic Von-Mises stress plot of the hull design. The peak stress (34 ksi) occurs at the ID of the ribs (not shown) and is 90% of the 0.2% yield stress of 6061-T6 Aluminum.

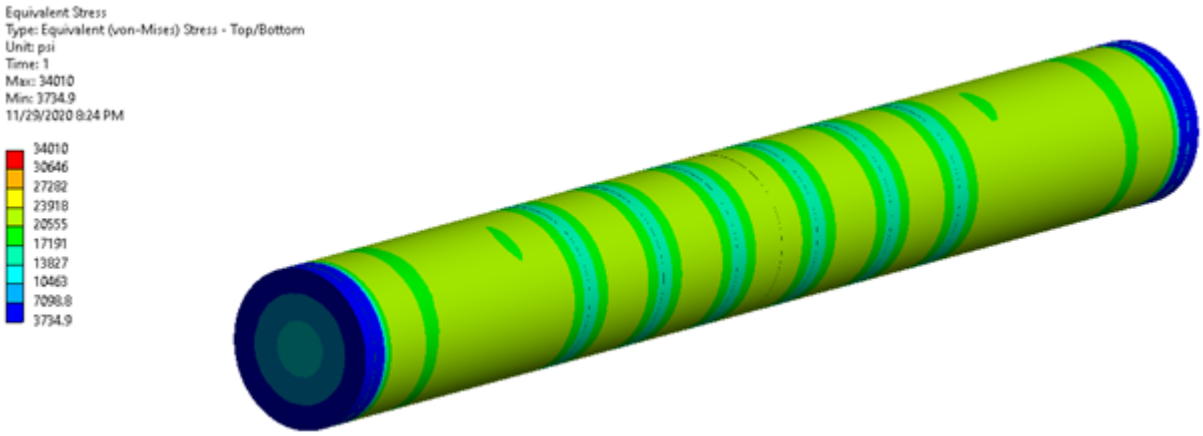

Figure 64: **FEA Model of Semi-Monocoque Hull Design** Showing Von-Mises Stress due to 1000m depth

Using the same boundary conditions as the stress model an Eigenvalue buckling analysis was performed. The first buckling mode, shown in Figure 65, shows deformation concentrated in the center of the hull. This was used to locate the ideal placement of the 6 frames.

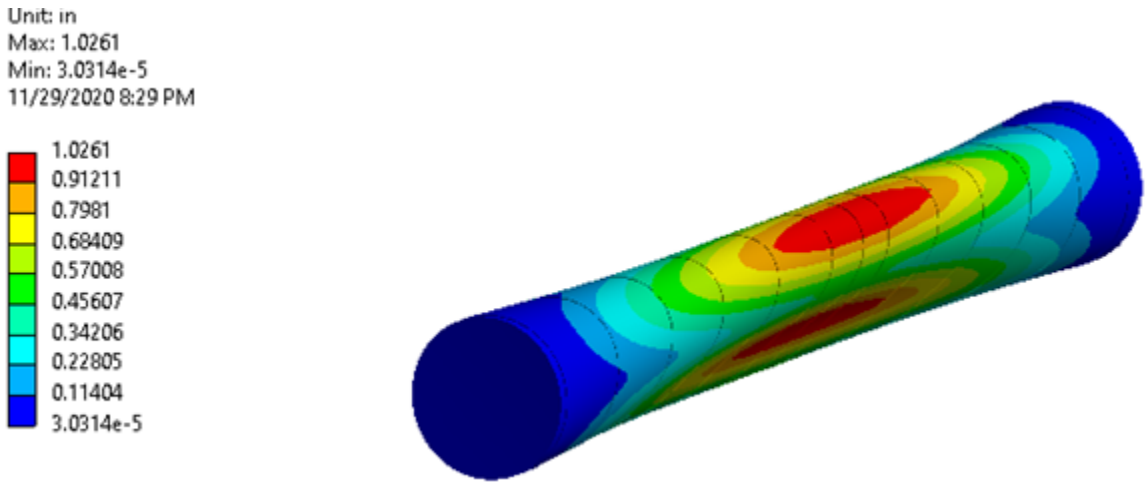

Figure 65: **FEA Model of Semi-Monocoque Hull Design** Showing Total Deformation from the 1st Buckling Mode.

Tolerance effects were analyzed to ensure a robust design. The published OD and ID tolerances from the tube manufacturer "OnlineMetals.com" gave a variation of ± 0.045[45] on the diameter for an extruded tube. However, that is the overall variation of the lot of tubing produced, not the variation that a single 72-inch tube length will see. Diameter variation expected over 72-inch tube length is conservatively assumed to be 1/6th (± 0.0075 in) of the lot variation. Scaling the deformation of the first buckling mode by this tube thickness variation was then performed to mimic the effects of these tolerances. Once the scaling was completed a nonlinear stress model (elastic-plastic) using the same boundary conditions was run again this time by ramping the pressure loads till failure occurred. While this analysis shows that failure of the hull will occur at 90% of the operational depth, it was also computed using very conservative assumptions and deemed sufficient for this design. Figure 66 shows the elastic-plastic Von-Mises stress plot of the hull design at 900m depth where ultimate tensile strength begins to be exceeded.

---

[45] Online Metals (n.d.). Retrieved November 23, 2020, from https://www.onlinemetals.com/en/aluminum-tolerances

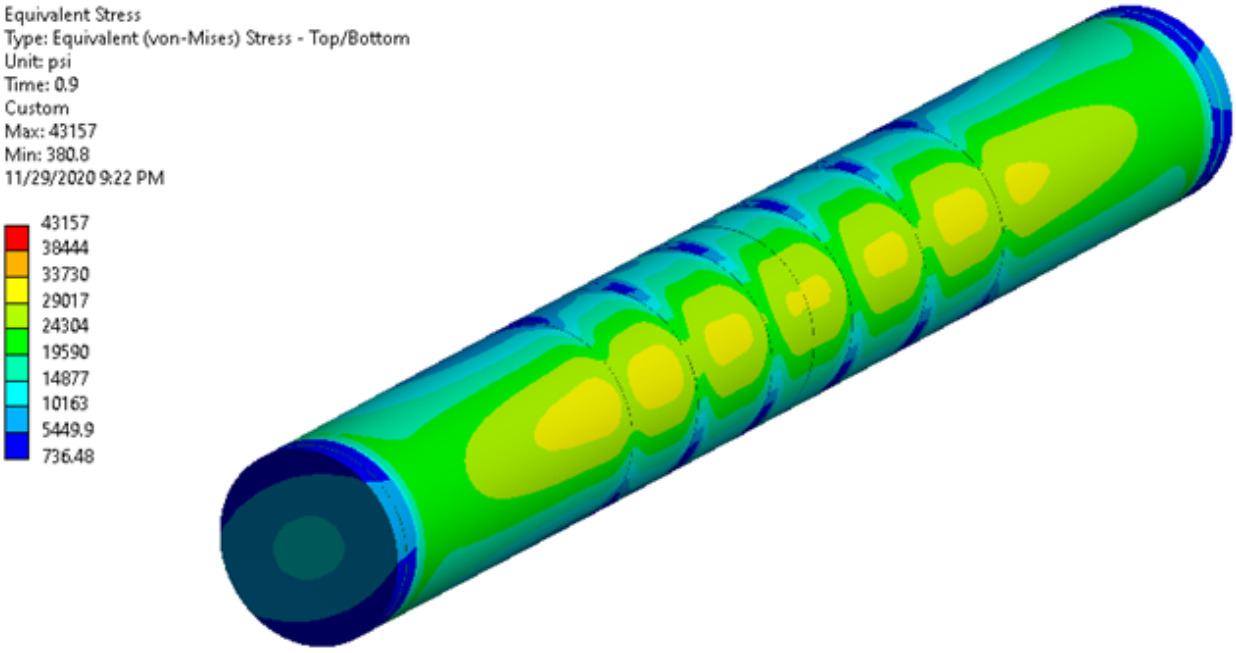

Figure 66: **FEA Model of Semi-Monocoque Hull Design** Showing Von-Mises Stress due combined buckling mode and manufacturing tolerance effects at 900m depth.

A sub-model of each end cap was modeled individually. The caps were de-featured to omit small provisions such as o-ring glands and fittings. Using the same boundary conditions and pressure from the 1000m depth the elastic-plastic stress analysis of the end caps, Figure 67, shows the Von-Mises stress. The peak stress (33 ksi) occurs at the center of both end caps and is 88% of the 0.2% yield stress of 6061-T6 Aluminum.

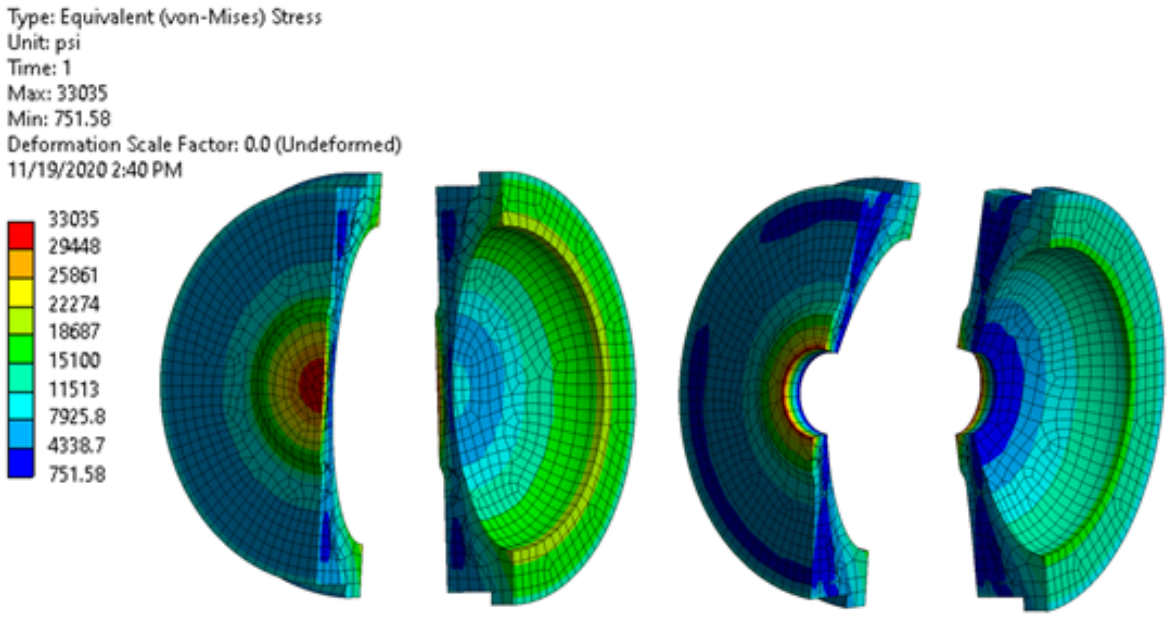

Figure 67: **FEA Model of End Cap Designs Showing** Von-Mises Stress. The left-hand images are the forward endcap and the right-hand images are the aft endcap. The caps are shown in halves so that the stress profile can be shown.

The FEA results show that the 6061-T6 aluminum hull, frames, and end caps are capable of meeting the operational depth requirement of 1000m without yielding. The converative buckling analysis demonstrated that UUV structure is also capable of meeting 90% of the pressure load assuming worst case tolerance effects of the hull which was significantly better than the 75% drop off in capability of the monocoque design. Future iterations can improve by taking deep dives into weight reduction and stress optimization.

6.4 Rails, Inner Mounting & Layout

6.4.1 Rails

The vehicle components are mounted on 80/20 1” x 1” rails (part no. 1010) that fit in grooves along the length of the hull. These rails are lightweight, weighing around 3 lb per rail, readily available, and have various mounting accessories that can be utilized for different components. Additionally, the rails do not take up much space.

Ultimately, the 80/20 rails are a justified design choice due to the mounting flexibility. However, there is room for improvement, notably around the structural integrity of the

rails. The 1010 series rails start bending at higher weights, and due to the length (72”), deflection will be even more pronounced.

6.4.2 Inner Mounting

Most of the components can be mounted directly to the rails using T-nuts that allow the components to be fastened securely with screws. These mounts are low profile and slide into the T-slot, keeping the area around the rails free of obstructions. Other series 10 fasteners can be utilized, depending on component needs.

The battery pack needs translational movement and will be mounted on a platform. The platform itself can be rolled along the rails using 0.36'' OD x 0.08 ''ID wheels and rods of diameter 0.07'' to connect the wheels. This platform is inserted into the rails first.

The motor to rotate the battery pack can also be mounted on this platform using a clamp motor mount that is attached to the platform using screws. This will reduce vibrations from the motor and allow for secure attachment to the battery pack.

6.4.3 Layout

The structural integrity of the rails remains an important consideration when designing the layout of the vehicle. The components need to be arranged in a way that the rails do not have high weight focused on one section. The rails we are using are susceptible to deflection with loads above 15lb, so careful consideration of the component placement is necessary. The space needed for battery pack translation needs to be taken into account as well.

In addition, as discussed in the system requirements, the vehicle needs to remain at least neutrally buoyant. Ideally, the center of mass and center of buoyancy should overlap nominally when the vehicle is submerged, and placement of components needs to result in as homogenous of a weight distribution as possible to maintain neutral buoyancy while in use.

6.5 End Caps & Fin Mounts

6.5.1 End Caps

The end caps were designed with a few goals in mind. The first is to create a water-tight seal to prevent the surrounding seawater from entering the dry hull. The second is to incorporate a fastening technique such that the end cap can be attached to the hull without introducing flanges, which could lead to unintended drag increases. The last motivation is to reinforce the geometry such that the end cap will not fail at depth.

With regards to forming the water-tight seal, this design used o-rings to prevent water from flowing into the rest of the hull. The ring itself is made of EDPM rubber and deforms easily to fill the space around it. The design of o-ring glands have been well-documented, with several companies providing manuals on how to best incorporate their product. The chosen o-ring, Dash Number 2-262, is approximately 7.262” in diameter. This was the closest in size to our cap’s inner diameter of 7.5” and could easily be sized with resources online. The groove dimensions to slot the o-ring into were taken from Parker Hannefin. As seen in Figure 68 below, two o-ring grooves were used in case one were to fail prematurely.

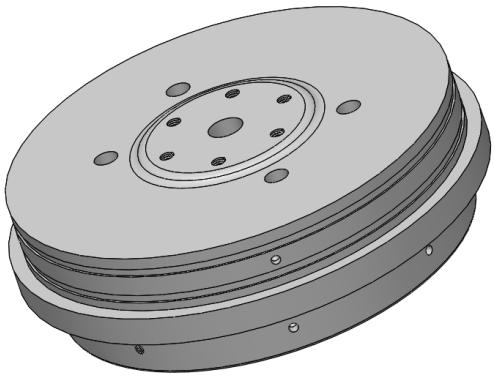

Figure 68: **3D Model of End Cap**

For the o-rings to prevent water from leaking into the hull, a constant radial force needs to be applied so that they fill up the gland space. This is achieved by drilling 4 circumferential holes around the end cap. Once the end cap is slotted into the hull, it can be firmly secured with these screws. An alternative method of creating flanges around the end cap was considered, but could create drag around the edges and was therefore avoided. The fairing attachment is identical for reasons discussed. We create

a “lip” on the outward facing face of the end cap for more circumferential screws to be fastened into.

Hull Wall
Housed Components

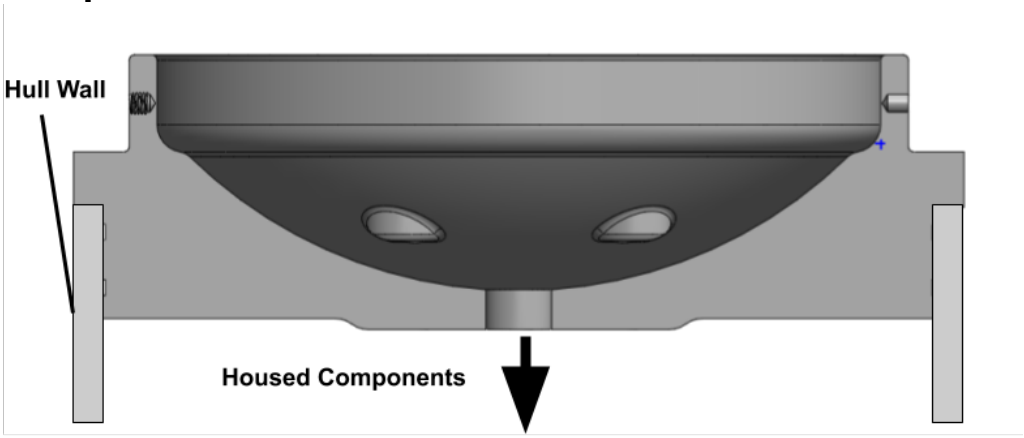

Figure 69: **Cross-Section of End Cap to show geometry and circumferential holes**

Finally, the pressure resistance was addressed by changing the geometry of the end cap. It is known that any fluid will exert a pressure force normal to any surface within it. Thus, changing the geometry will also reduce compressive loads felt by this object. This design uses a hemispherical shape to best do this.

6.5.2 Fin Mounts

The fins are mounted on the surface of the hull using a modular fin mount component shown in Figure 70. The fins slide into the fin slots and are bolted down to the mount itself. The mount is then securely attached to the hull using hose clamps with a width of 0.5”, with a clamping diameter range of 7"-9.9", which is sufficient for the OD of the hull.

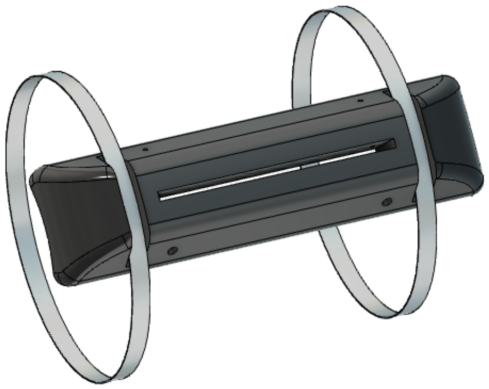

Figure 70: **A preliminary fin mount design** with a slot to securely bolt the fins down and grooves to attach the system to the main structure using hose clamps.

The fin mount and clamp system is capable of not only withstanding the drag force on the fin but also impact forces up to half the structure weight. The main advantage of using this mounting system is that it is easy to assemble/disassemble and replace fins when necessary. This was designed to make use of both inexpensive off the shelf parts as well as easily in-house manufacturable components using a CNC mill.

6.6 Assembly

Assembly of the ribs to the hull will be accomplished by interference fits and adhesive to secure the ribs in place. The process of heating and chilling will be used to obtain the clearance needed to assemble the frames into the hull. The tube section will be heated to 150°C which is the max it can be heated without annealing the properties. The frames will be chilled to -75°C which is the sublimation temperature of dry ice. Using a simple calculation (Equation 26) to determine that a clearance of 0.5 mm (on the diameter) is obtained from the heat and chill process.

$$\Delta D_{OD} = D_{OD}\alpha_{alum}\Delta T \tag{26}$$

Using the appropriate personal protective equipment and pressing jigs, the ribs can be placed into the correct locations. Simple tooling which was sized to the length of the rib location can be used as jigs to aid in this time sensitive process. The interference is then obtained as temperatures normalize to ambient. Once cooled, beads of adhesive are used to bond the ribs to the hull as a means for secondary retention.

All the internal components will mount to the rails. The rails will be first bolted to the rear end cap. The propeller motor, the battery shifting mechanism, and the buoyancy engine can subsequently be installed to the rails. The rear fairing can be installed and

the propeller can be fastened to the propeller shaft. After all necessary wiring and piping has been fastened, the skeleton is ready for insertion into the hull.

Sliding in the skeleton can be done by 2 people holding each side of the rail and sliding in the rails into the rib notches.

Figure 71: **Horizontal view of the separate hull and internal skeleton sections**

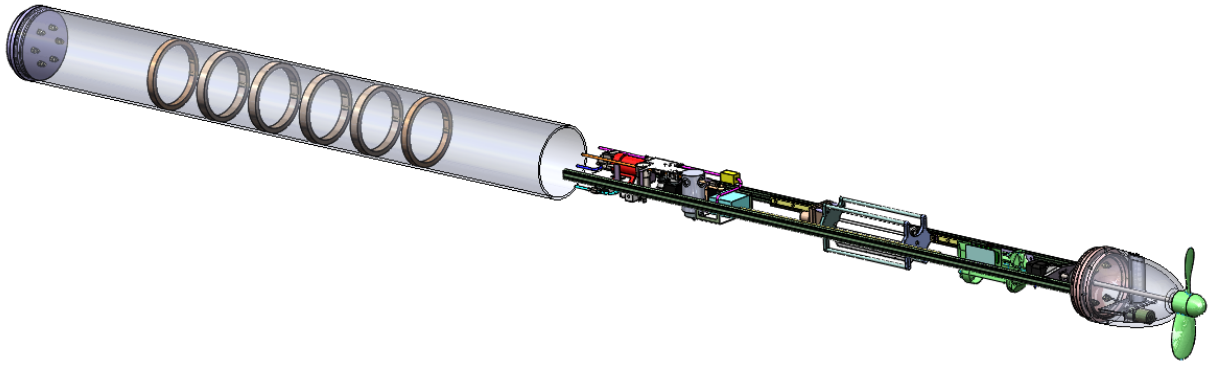

Figure 72: **Isometric view of the separate hull and internal skeleton sections**

7 Next steps

7.1 4 year plan

7.1.1 System recap

The DOUG LE1000 system is a lightweight and cost effective vehicle that can be deployed on 30-day missions before recovery. The strategy for this system is to deploy a large number of vehicles (a “Swarm”) to perform ocean data acquisition activities for a large volume of water. Each individual vehicle is very low in cost, and performs rapid dive cycles up to 1000m in depth, therefore sampling high volumes of water while keeping the overall system cost low.

The vehicle’s long endurance is achieved through a hybrid aluminum-powered buoyancy engine and fuel cell. Aluminum fuel is stored in power form on-board the vehicle. When surface-treated aluminum is reacted with water, it creates hydrogen. This hydrogen is used in the buoyancy engine, and then fed through a fuel cell when the vehicle reaches the surface. The fuel cell recharges a battery pack which powers the vehicle through the following dive. A propeller is used to supplement the buoyancy engine for propulsion. A PV array is used to supplement the battery recharging.

The vehicle performs navigation through INS, GPS, and acoustic positioning systems. These three systems work together to accurately communicate the vehicle’s position throughout the mission. The INS system is able to determine the position of the vehicle, while the GPS can pinpoint the vehicle’s position at the surface. Acoustic positioning takes advantage of the vehicle swarm strategy for real-time positioning of vehicles that are at deeper depths.

The system is controlled via a Raspberry Pi controller, and is positioned using a weight-shifting mechanism. The battery pack is used as a weight, which is shifted forward and aft via rails in the vehicle in order to control pitch and roll.

The aluminum hull is able withstand the high pressures experienced at 1000 m under the sea by utilizing a ribbed design, which adds stiffness to the hull and increases resistance to buckling. Fluids are able to pass through the hull via forward and aft end caps, and the vehicle’s fins are also mounted to the hull. Conical fairings create a hydrodynamic shape while protecting the external components from environmental factors.

Each of DOUG's subsystems are integrated to deliver a vehicle that is low in cost, low in weight, and able to perform a 30-day mission. This system is an improvement on existing AUV designs in terms of logistics, maintenance, endurance, and data sampling volume.

7.1.2 Modularity

Modularity of DOUG should be improved as part of the four-year plan. Currently, each subsystem is integrated into the main pressure hull of DOUG. The subsystems can be further designed so that they are "plug and play" easily replaceable between missions. Certain components, such as the fuel cell,batteries and blader, are likely single-use and should be discarded after each mission.

The DOUG vehicle is also modular in that it is designed for swarm sampling. Each individual vehicle is very low in cost and could therefore be disposed of without major losses.

7.1.3 Deployment

As mentioned in previous sections, the deployment of DOUG vehicles is made to be as simple and logistically simple as possible. The vehicle mass is less than 80kg total, which allows it to be lifted and deployed from a ship with a two-person lift. No cranes or hoist equipment is required. Additionally, the low cost of DOUG allows a swarm of vehicles to be deployed at once. A group of vehicles may be deployed from a ship, and recovered 30 days later. This low-cost swarm strategy reduces the logistical need for surface vehicles to monitor the vehicles. Surface vehicle monitoring is the largest driver of cost for typical UUV systems.

8 Appendix

Energy

Hybrid Aluminum Buoyancy Engine and Fuel Cell

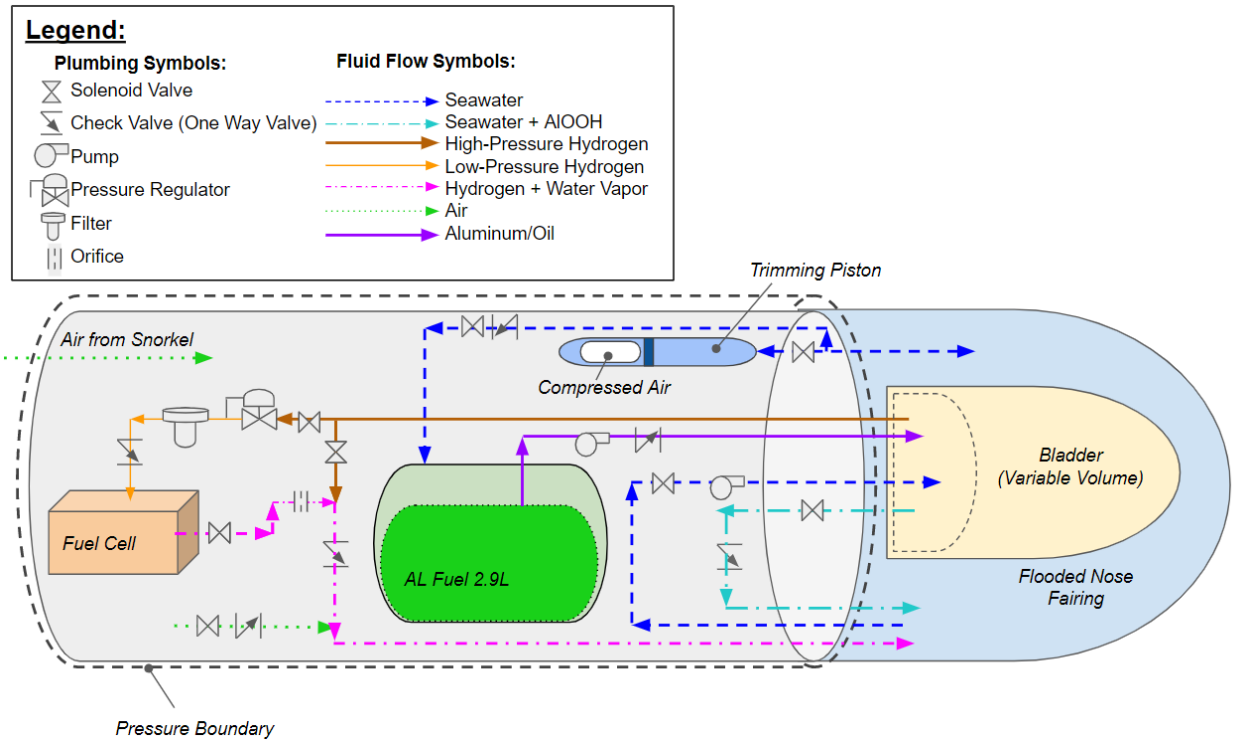

Figure A1: **Hybrid aluminum buoyancy engine and fuel cell.** The compound energy system is shown here.

Navtronics

Weight shifting math

We wrote a MATLAB script to determine the moment balance in different states of buoyancy engine inflation and battery displacement. Input parameters are as follows:

Lift parameters:

Lift coefficient C_L
Cruising velocity v
Wing surface area A

Environmental constants:

Water density ρ
Gravitational constant g

Hull dimensions:

Outer radius R
Vehicle length L

Masses:

Structures m_{struct}:
Hull m_{hull}
Wiring harness $m_{harness}$

Energy m_{energy}:
Fuel cell $m_{fuelcell}$
Battery $m_{battery}$
DCDC converter m_{DCDC}
Snorkel $m_{snorkel}$
Electrical components m_{elec}
PV cell m_{PV}

Hydro m_{hydro}:
Starting aluminum fuel m_{Al}
Propeller m_{prop}
Propeller motors $m_{prop\ motors}$

Propeller coupling $m_{coupling}$

Buoyancy engine m_{BE}

Nav m_{nav}:

Electronics $m_{nav\ elec}$

Hydrophone $m_{hydrophone}$

CTD m_{CTD}

Positions (measured from rear end):

$r_{component}$for $component$ in

$\{hull,\ wiring\ harness,\ fuel\ cell,\ battery,\ DCDC\ converter,\ snorkel,\ energy\ electrical\ components,\ PV\ cell,\ Al\ fuel,\ propeller,\ prop\ motors,\ prop\ coupling,\ buoyancy\ engine,\ nav\ electronics,\ hydrophone,\ CTD\}$

Bladder volumes:

$V_{BE},\ max$ (fully inflated)

$V_{BE},\ min$ (fully deflated)

From these input parameters, buoyancy forces and subsequently, moment contributions from all buoyancy and gravity forces can be computed.

$Buoyancy force\ =\ -\rho Vg$for a specified bladder volume. Total hull buoyancy can be computed the same way, though compression effects must be accounted for, which cause the hull to lose buoyancy with depth.

Lift force and moment contribution from the wings is computed as follows:

$$F_{lift} = \frac{1}{2} C_L \rho v^2 A$$

Center of buoyancy and center of mass locations can now be computed:

$$r_{COB} = \frac{\sum_{components} F_{b,\ component} r_{component}}{\sum_{components} F_{b,\ component}},\ r_{COM} = \frac{\sum_{components} F_{g,\ component} r_{component}}{\sum_{components} F_{g,\ component}}$$

Finally, the total moment about the center of mass can be computed as follows, where θ_{init} is the pitch angle of the vehicle. This is the critical figure in determining vehicle control dynamics and the viability of any particular layout of components.

$$Moment = cos(\theta_{init})\frac{r_{COM} - r_{COB}}{\Sigma F_b}$$

Electronics

Controller Selection

The goal of controller selection was to pick the lowest power controller which still had the connectivity to interface with the required devices and the processing power to control the required devices and do the required calculations. The original potential options included Raspberry Pi like, Ardunio like, and PC 104 form factor controllers. Because of the cost, availability, documentation, and helpful community associated with Raspberry Pis and Ardunios, it was later decided to not expand into the “knock-off” and less common versions. After researching it appeared that at least most of the UUVs with information about their controller publicly available use a PC 104 form factor controller.

A Raspberry Pi is essentially just a small low power computer using an ARM CPU similar to those used in smartphones. Raspberry Pis also offer many of the connectivity options a computer would as well as a 40 pin GPIO header which is compatible with digital signals. Arduinos usually also use an ARM based CPU, but it is much lower power and typically only has one thread meaning it can’t multitask. Arduinos are capable of handling both digital and analog signals. PC 104 is a small form factor for computers with stackable interconnecting boards so as to increase modularity by allowing a user to choose which stackable modules to add for their use case. It often uses a low power x86 chip such as Intel Atom, but versions with higher end CPUs, such as one similar to Core i7 laptop chips, are also available.

All of the options where temperature range information could be found were rated for a temperature at least as low as 0°C and as high as 50°C. While the range goes low enough for the estimated 4°C temperatures expected at depth, it does not encompass the estimated -2°C surface temperatures expected around the North Pole.[46] While it is likely they will still work, further testing of the electronics will be required before confidently deploying it to areas with similarly cold surface temperatures to ensure they can operate under those conditions. All of the options can also have expandable

[46] “NWS JetStream - Layers of the Ocean” [Online]. Available: https://www.weather.gov/jetstream/layers_ocean.

storage, but this is more complicated with Ardunios since they would also require an additional PCB shield board.

Raspberry Pi 4 Model B Connectivity

Figure A2: **Raspberry Pi 4 Model B Pinout.** This shows which pins can be used for I2C, UART, and SPI. Pins 12, 32, 33, and 35 are also capable of PWM.[47] [48]

[47] "Raspberry Pi 4 Model B Datasheet." Available: https://www.raspberrypi.org/documentation/hardware/raspberrypi/bcm2711/rpi_DATA_2711_1p0_preliminary.pdf.

[48] "Raspberry Pi GPIO Pinout: What Each Pin Does on Pi 4, Earlier Models," Tom's Hardware [Online]. Available: https://www.tomshardware.com/reviews/raspberry-pi-gpio-pinout,6122.html.

The Raspberry Pi 4 Model B has 40 GPIO pins and is capable of having up to 6 I2C connections, 6 UART connections, 5 SPI connections, 2 PWM connections, 2 USB 2.0 connections, 2 USB 3.0 connections, a micro SD card slot, 1 Gigabit Ethernet connection with PoE, a 4 pole 3.5mm audio jack, 2 micro HDMI connections, a 2-lane MIPI CSI camera port, a 2-lane MIPI DSI display port, 2.4 GHz IEEE 802.11 b/g/n/ac wifi, 5.0 GHz IEEE 802.11 b/g/n/ac wifi, and Bluetooth 5.0 BLE.[49]

CTD Selection

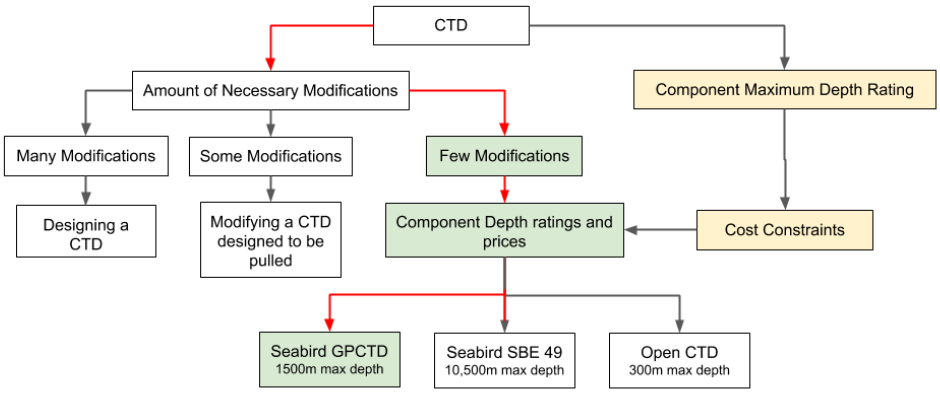

Figure A3: **CTD Decision Tree.** This shows a brief explanation of how the Seabird GPCTD was chosen.

CTD selection was based partially on the time constraints of this class. Designing our own CTD could likely be its own class and designing modifications for an existing one is difficult without actually having a physical sample since many of these manufacturers are reluctant to give out detailed CAD that includes interior components. When looking at depth ratings and pricing, existing cheap DIY CTDs are not up to the task. Between the Seabird CTDs, chosen due to documentation claiming they were the common CTDs used in UUVs and gliders, The GPCTD was chosen due to its lower power.[50]

Future CTD Option

In future iterations of this swarm concept a cheaper CTD could be used for most of the vehicles. This idea involves having some vehicles outfitted with an accurate CTD such as the GPCTD used on this version and most vehicles outfitted with a cheaper, less-accurate custom made CTD. The data from the more accurate CTDs could be used to to estimate if the cheaper CTDs were still calibrated and possibly even allow post-

---

[49] "Raspberry Pi 4 Model B Datasheet." Available: https://www.raspberrypi.org/documentation/hardware/raspberrypi/bcm2711/rpi_DATA_2711_1p0_preliminary.pdf.

[50] Wood, S., and Pardis, R., 2013, "Inexpensive Expendable Conductivity Temperature and Depth (CTD) Sensor."

mission data correction. This concept needs more refinement, but could prove useful in reducing overall swarm costs.

Navigation math

The SLBL positioning scheme utilizes data from the CTD, hydrophones, and internal clocks. As Figure A4 shows, the CTD is used to determine the speed of sound in the water using the equations in Figure A5. The speed of sound is multiplied by the one way travel time of the acoustic ping sent from a surface vehicle to determine the Euclidean distance between the two vehicles. The one way travel time is derived by the time difference of when the ping was scheduled to be sent and when the underwater vehicle receives the ping. The depth measurement is taken from the CTD and combined with the Euclidean distance to determine a circle radius around the surface vehicle that the underwater vehicle could be in. This process is repeated with multiple surface vehicles and the multiple circles calculated are used to triangulate the position of the vehicle. The common intersection is used to find the relative position which is converted to an absolute position based on the GPS locations of the surface UUVs.

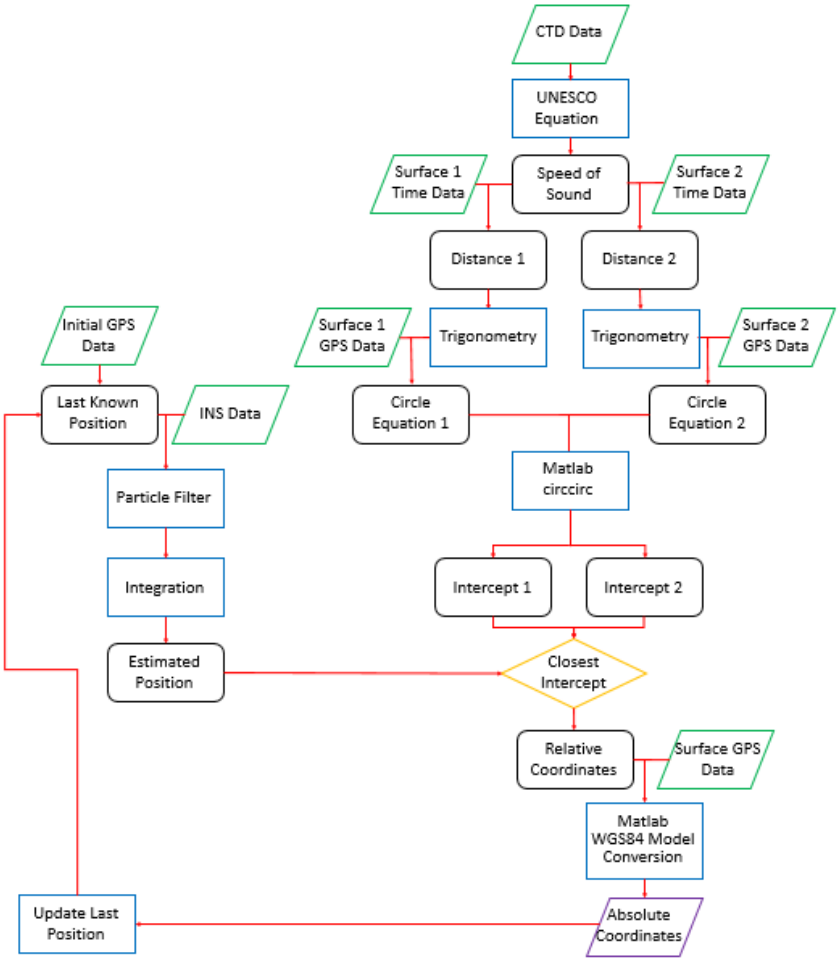

Figure A4: **Acoustic Positioning Signal Processing Flow Chart.** This shows a simplified flow of how the absolute position is calculated.

$$V_{Sound} = c(\mathrm{S,T,P})$$

$$c(S,T,P) = Cw(T,P) + A(T,P)S + B(T,P)S^{3/2} + D(T,P)S^2$$

$$Cw(T,P) = (C_{00} + C_{01}T + C_{02}T^2 + C_{03}T^3 + C_{04}T^4 + C_{05}T^5) + (C_{10} + C_{11}T + C_{12}T^2 + C_{13}T^3 + C_{14}T^4)P + (C_{20} + C_{21}T + C_{22}T^2 + C_{23}T^3 + C_{24}T^4)P^2 + (C_{30} + C_{31}T + C_{32}T^2)P^3$$

$$A(T,P) = (A_{00} + A_{01}T + A_{02}T^2 + A_{03}T^3 + A_{04}T^4) + (A_{10} + A_{11}T + A_{12}T^2 + A_{13}T^3 + A_{14}T^4)P + (A_{20} + A_{21}T + A_{22}T^2 + A_{23}T^3)P^2 + (A_{30} + A_{31}T + A_{32}T^2)P^3$$

$$B(T,P) = B_{00} + B_{01}T + (B_{10} + B_{11}T)P$$

$$D(T,P) = D_{00} + D_{10}P$$

Coefficients	Numerical values	Coefficients	Numerical values
C_{00}	1402.388	A_{02}	7.166E-5
C_{01}	5.03830	A_{03}	2.008E-6
C_{02}	-5.81090E-2	A_{04}	-3.21E-8
C_{03}	3.3432E-4	A_{10}	9.4742E-5
C_{04}	-1.47797E-6	A_{11}	-1.2583E-5
C_{05}	3.1419E-9	A_{12}	-6.4928E-8
C_{10}	0.153563	A_{13}	1.0515E-8
C_{11}	6.8999E-4	A_{14}	-2.0142E-10
C_{12}	-8.1829E-6	A_{20}	-3.9064E-7
C_{13}	1.3632E-7	A_{21}	9.1061E-9
C_{14}	-6.1260E-10	A_{22}	-1.6009E-10
C_{20}	3.1260E-5	A_{23}	7.994E-12
C_{21}	-1.7111E-6	A_{30}	1.100E-10
C_{22}	2.5986E-8	A_{31}	6.651E-12
C_{23}	-2.5353E-10	A_{32}	-3.391E-13
C_{24}	1.0415E-12	B_{00}	-1.922E-2
C_{30}	-9.7729E-9	B_{01}	-4.42E-5
C_{31}	3.8513E-10	B_{10}	7.3637E-5
C_{32}	-2.3654E-12	B_{11}	1.7950E-7
A_{00}	1.389	D_{00}	1.727E-3
A_{01}	-1.262E-2	D_{10}	-7.9836E-6

Figure A5: **Speed of sound in the ocean.** Shown is a condensed version of the high-dimensional experimentally determined equation for speed of sound through the ocean.[51]

With the rough INS positioning data, triangulation can be done with only 2 surface vehicles. In this case, there should be 2 intersections of the circle radiuses as shown in Figure A6. The choice between the intersection points can be made by which intersection is closest to the INS position estimate.

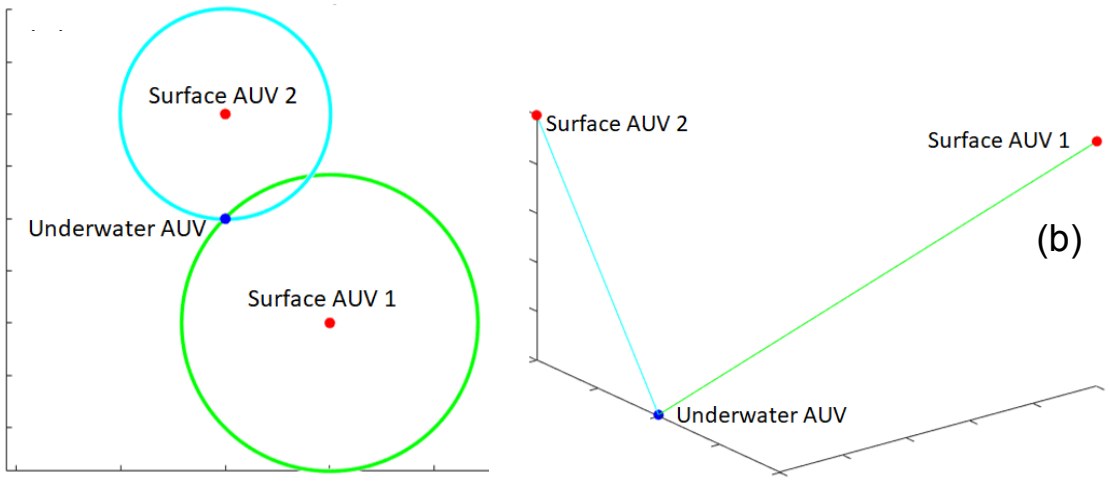

Figure A6: **Acoustic Positioning Locating Example.** (a) shows an example of the two intercepts created when only two surface vehicles are used. (b) shows the 3D relative positions of the vehicles in this example.

[51] "Technical Guides - Speed of Sound in Sea-Water" [Online]. Available: http://resource.npl.co.uk/acoustics/techguides/soundseawater/content.html.

Structures

Uniform Thickness Tube Defect Susceptibility FEA Study

One of the main reasons our team moved away from a uniform thickness tube as the hull was due to the susceptibility of that design to manufacturing defects. The source referenced in 6.3.1 points to a number of empirical data points showing how theoretical buckling solutions far exceed actual buckling capabilities for cylindrical tubes. To prove this to ourselves further we applied a delta pressure loading to a uniform thickness 0.250” tube in ANSYS workbench. The model was run with ANSYS default nonlinear material properties for aluminum alloys and nonlinear geometry effects turned on. The capability prediction was nearly 2x our operating pressure as seen by the load factor of 1.95 in the following stress plot:

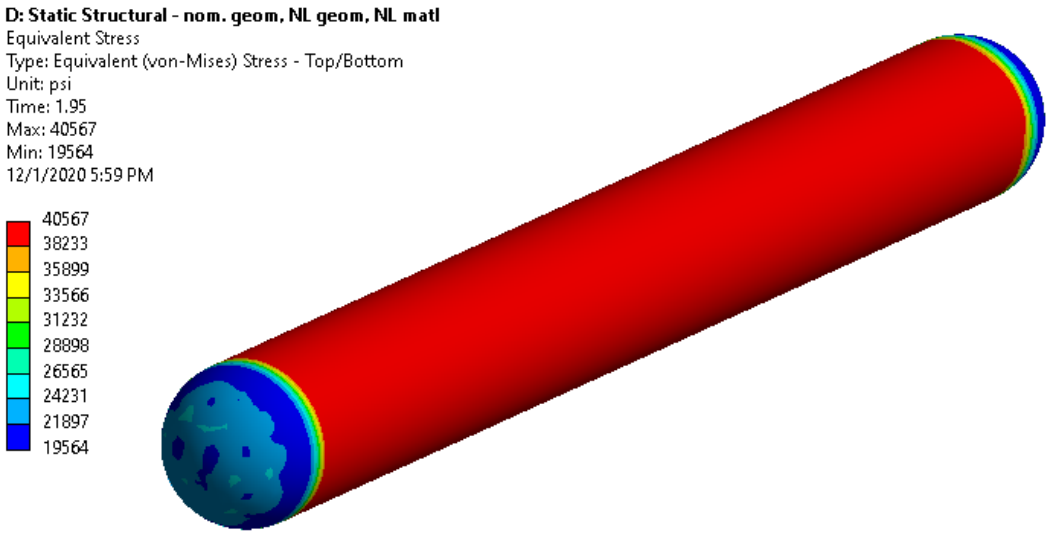

Figure A7: **Stress plot of uniform thickness tube.**

Next, we ran an eigenvalue buckling analysis to determine which buckling mode shapes we might experience. We took the first buckling mode deflected shape and scaled it to be within manufacturing tolerances for a drawn aluminum tube (+/- .015” on a diameter). The first eigenmode shape is shown in the image below:

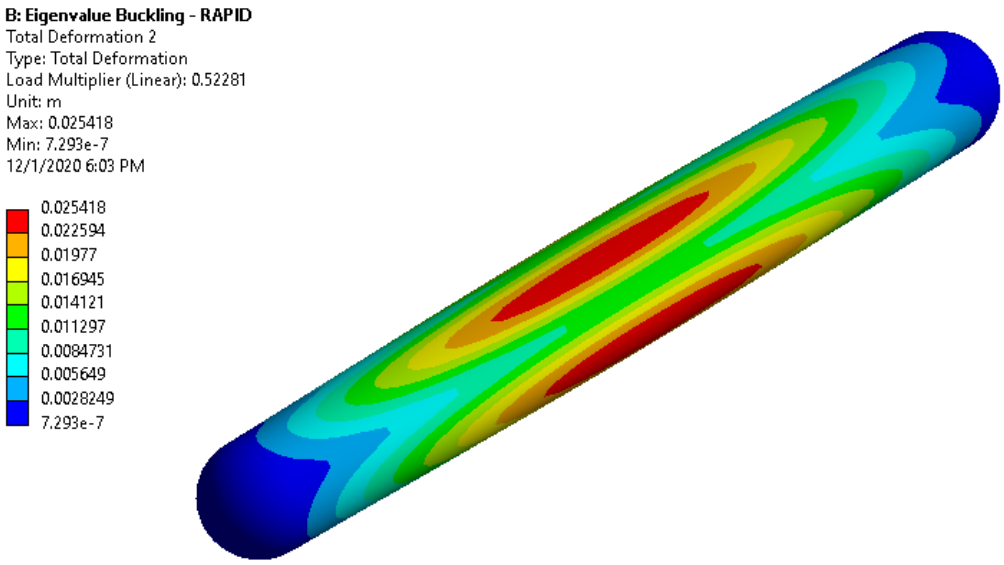

Figure A8: **Eigenvalue buckling of uniform thickness tube.**

After scaling the deflections to be within manufacturing tolerances, we fed this new geometry into the same analysis that we ran before to observe the change in capability. This resulted in a new load factor capability of 0.48:

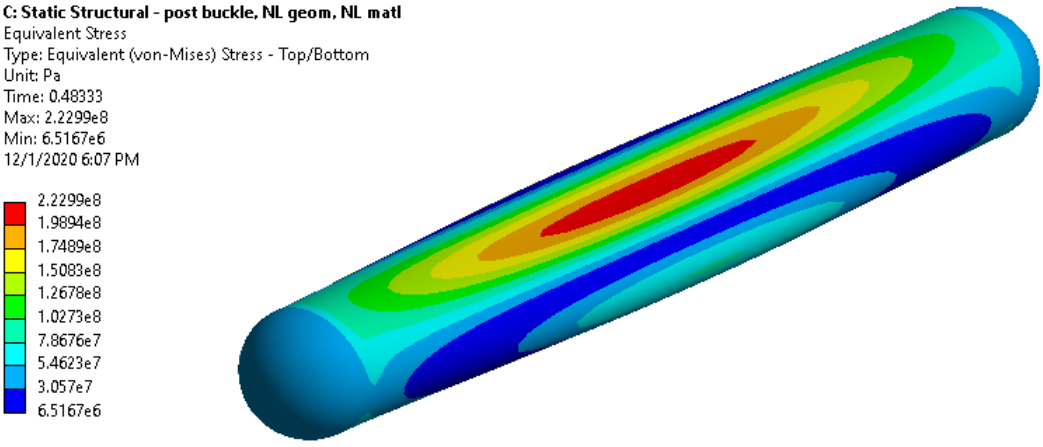

Figure A9: **Post-buckling stress plot.**

Abandoned Alternative Designs

Corrugated Hull

Concerns with a straight aluminium cylinder design included exceeding the system weight requirement, as well as the reduction of its buckling capacity due to manufacturing imperfections and local defects on the surface. Thus, a preliminary corrugated hull design shown in Figure A10 was explored with the goal of minimizing the overall mass of the vehicle while still meeting strength requirements.

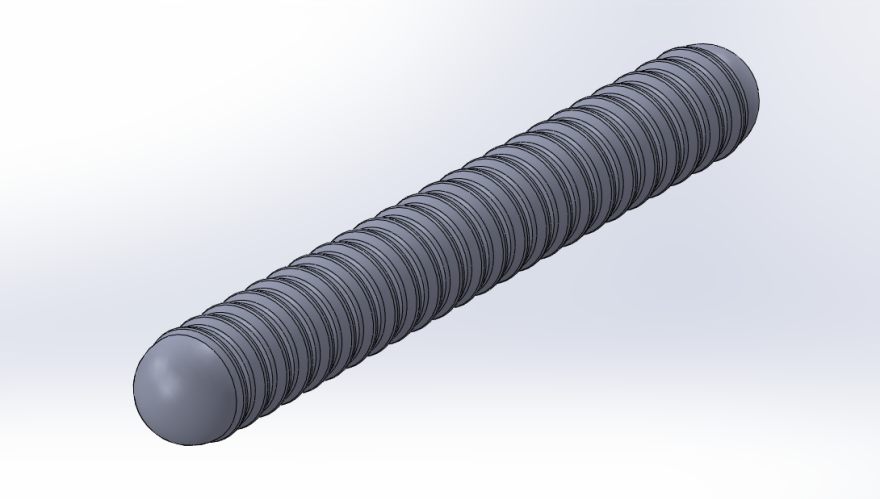

Figure A10: **A preliminary corrugated hull design** with corrugations spaced 2.67” apart uniformly through the body, with a capability of up to 1500m (1.5 S.F).

The inspiration behind this idea was driven by a documented experiment in which the research team manually added corrugations to otherwise smooth tubes. They started with a smooth wall cylinder (CSC1 in Figure A11 below) and added a corrugation along the length of the cylinder before fully corrugating the tube in configuration CSC5. They applied hydrostatic pressure and buckled each tube except for the fully corrugated design which withstood the maximum pressure they could apply. The results from their experiments are summarized in Figure A11 below.[52]

[52] Ghanbari Ghazijahani, T., Sadighi Dizaji, H., Nozohor, J., and Zirakian, T., 2015, “Experiments on Corrugated Thin Cylindrical Shells under Uniform External Pressure,” Ocean Engineering, **106**, pp. 68–76.

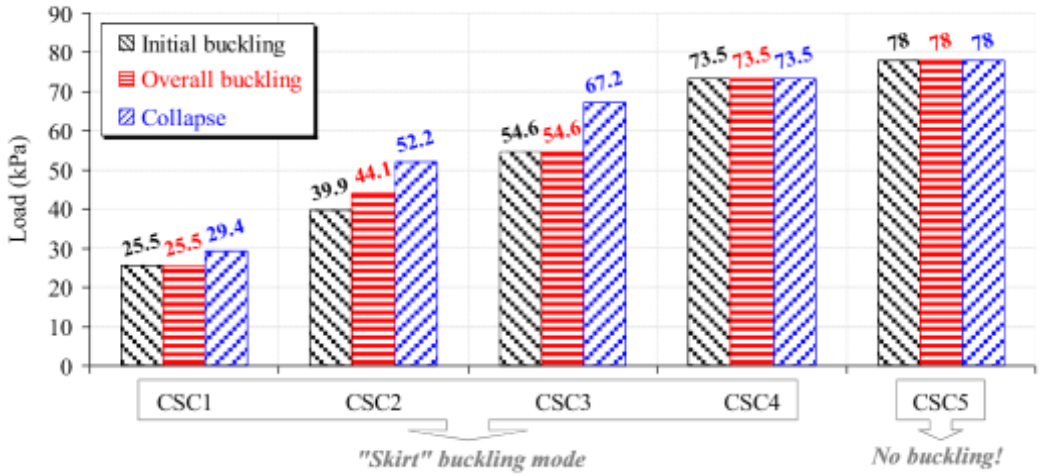

Figure A11: **Buckling performance of corrugated tubes.**[53]

This study proved that without adding additional material, adding corrugations could increase the stiffness of the tube. After realizing this, we designed our corrugation height and spacing based on industry standard metal corrugated pipes and Figure A12 below depicts the dimensions of the design:[54]

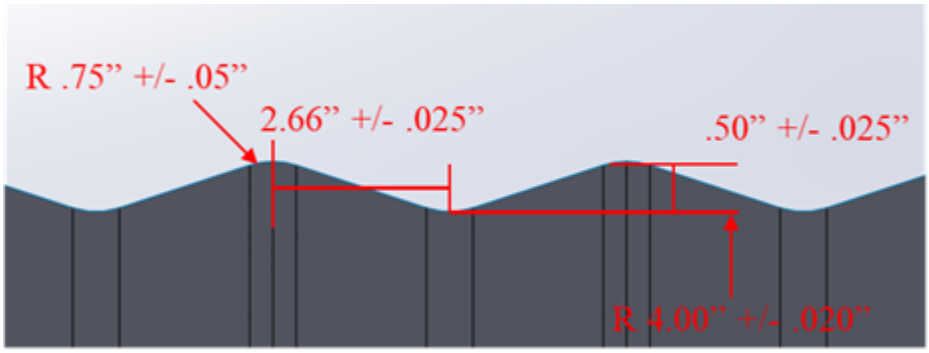

Figure A12: **Corrugated hull dimensional parameters.**

The thickness of the corrugated pipe was 0.25 inches. This design demonstrated a 1.26 load factor, just shy of the 1.5 safety factor required. There is likely some opportunity to fine tune parameters such as radius size, corrugation height, and corrugation spacing to improve upon the capability. The corrugations also showed

[53] Ghanbari Ghazijahani, T., Sadighi Dizaji, H., Nozohor, J., and Zirakian, T., 2015, "Experiments on Corrugated Thin Cylindrical Shells under Uniform External Pressure," Ocean Engineering, **106**, pp. 68–76.

[54] Contech Engineered Solutions. "Corrugated Metal Pipe Design Guide." Available: https://www.conteches.com/Portals/0/Documents/Design%20Guides/CMP-Design-Guide.pdf?ver=2018-05-16-083622-383.

resilience to defects. Utilizing the same approach for the eigenvalue post buckled shape analysis, the capability decreased from a 1.26 load factor to 1.03.

However, the manufacturing complexity associated with making a hull like this posed the biggest challenge. The manufacturing method we explored in the closest detail was tube hydroforming because it gave us the opportunity to utilize off the shelf input material which we thought would help drive cost down.[55] We were able to confirm the technical feasibility with a vendor, Quasar Industries. The one design change necessary would be to increase the bend radius size or we would have to change the aluminum alloy to something more favorable to forming than a 6000 series aluminum. Initial cost estimates were on the order of hundreds of thousands of dollars for the mold/tooling needed to make a part this size which made this manufacturing concept infeasible for low rate production and prototyping. From a technical standpoint and ease of assembly, a one-piece hull design like this is favorable, but more work must be done to identify a manufacturing method with capability of producing this geometry on a reasonable budget.

Flooded Hull

A flooded hull was a concept we explored for reducing the overall mass of the vehicle during deployment. In this concept, the interior of the hull is filled with a dielectric fluid, such as oil or deionized water which could share the load from the high external pressure applied to the hull. The hull could then be made thinner or use a lower density material (such as plastic) to reduce mass. Where needed, low density counterballasting material, such as syntactic foam, can be added to avoid excessive negative buoyancy. We determined that a flooded hull concept could reduce the unfilled mass of the vehicle by up to 15% to allow for easier handling during deployment. The main trade-off, and reason for not implementing this concept in the final design, was that the filling fluid would develop significant pressure at depth, leading to a high pressure environment for internal components. Figure A13 shows the results of this trade-off for various fill fluid and hull material combinations based on the mathematical analysis detailed later in this section.

[55] “What Is Hydroforming,” American Hydroformers. Available: https://americanhydroformers.com/what-is-hydroforming/.

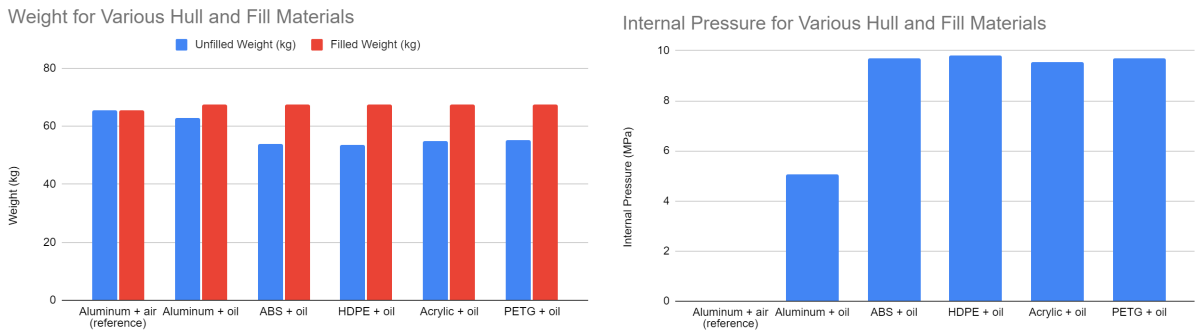

Figure A13: **Weight and internal pressure for various hull and fill naterials.** The plots show six hull and fill fluid combinations (from left to right): aluminum + air (reference configuration), aluminum + oil, ABS + oil, HDPE + oil, acrylic + oil, and PETG + oil.

During preliminary research, we found a number of candidate materials for fill fluids and counterballasting materials. A summary of these materials and some of their properties are shown in Figure A14. Of these materials, we found that a combination of vegetable oil and structural foam would be the cheapest while having sufficiently low density to keep added mass low.

Material	Density (kg/L)	Thermal Conductivity (kJ/kg*K)	Dielectric Breakdown (kV)	Cost/volume ($/L)	Gross?	Environmentally friendly?	Source
Fish oil	0.92			5.52	Yes	Yes	Alibaba product
DI water	1	Link		0.26	No	Yes	Home Depot product: re-ionizes too easily?
Microballoons	0.15			16.25	?	?	Glass Fibre website: might not be stiff enough to be effective?
Vegetable Oil	0.91	1.67		1.41	Yes	Yes	I bought vegetable oil recently... ~$2 for 1.42L
Novec	1.27		20	?	?	Supposedly	Link on 3M: quote requested for 72DE engineered fluid
Transformer dielectric	0.92		25	?	?	Yes	Cargill FR3 Fluid: quote requested
Structural foam	0.15			1.17	No	?	Composite Essentials website: "$2.75 psf" for 96" x 40" x 1" block (62.93L volume) for GR150
Syntactic foam	0.24			28.07	No	?	Syntoam website: $795 for 12" x 24" x 6" block (28.32L) for Syntoam SW

Figure A14: **Options for Fill Fluid and Counterballasting Materials with Selected Properties.** Cost and density primarily drove initial decisions, with environmental and handling considerations considered qualitatively.

According to Table 13.5 in Roark[56] and using superposition, the change in internal radius ΔR_{in} due to an external pressure and internal pressure in a cylindrical vessel is given by:

[56] Roark, R. J., Young, W. C., and Budynas, R. G., 2002, Roark's Formulas for Stress and Strain, McGraw-Hill, New York.

where all variables are as defined in Figure A15. We may also assume that the internal fluid has some compressibility defined by:

$$\Delta R_{fluid} = -p_{in}\beta R_{in} \tag{2}$$

We know that $\Delta R_{in} = \Delta R_{fluid}$ due to geometric constraints. We may also make the thin-walled cylinder approximation such that $R_{out} \approx R_{in}$ and $R_{out} - R_{in} = t$, where t is the hull's thickness:

$$-\frac{p_{out}R_{in}}{E_{hull}}\left(\frac{2R_{in}^2}{2R_{in}t}\right) + \frac{p_{in}R_{in}}{E_{hull}}\left(\frac{2R_{in}^2}{2R_{in}t} + \nu\right) = -p_{in}\beta R_{in} \tag{3}$$

$$\frac{p_{out}}{p_{in}} = 1 + (\nu + \beta E_{hull})\frac{t}{R_{in}} \tag{4}$$

Finally, this expression relating p_{out} and p_{in} can be combined with the following expression for stress in a thin-walled pressure vessel:

$$\sigma = \frac{(p_{out} - p_{in})R_{in}}{t} \tag{5}$$

to yield an expression for stress as a function of p_{out}, geometry, and material properties only.

Condition	Assumptions	Equation
Max hoop stress	σ_z and σ_r negligible compared to σ_θ Material fails if it yields	$\sigma_{max} = \frac{\sigma_y}{SF}$
Hoop stress in *rigid* hull	Thin-walled pressure vessel ($t \ll R$)	$\sigma_{max} = \frac{(p_{out} - p_{in})R_{in}}{t}$
Hoop stress in *compliant* hull	Thin-walled pressure vessel ($t \ll R$) Hull and internal fluid are both stiff	$\sigma_{max} = p_{out}\frac{\nu_{eff}}{1+\nu_{eff}\frac{t}{R}}$ where $\nu_{eff} = \nu + \beta E_{hull}$
Internal pressure in *compliant* hull	Thin-walled pressure vessel ($t \ll R$) Hull and internal fluid are both stiff	$p_{in} = \frac{p_{out}}{1+\nu_{eff}\frac{t}{R}}$
Neutral buoyancy	Some counter-ballasting is needed to reach neutral buoyancy	$\rho_{sw} = \frac{M_{hull} + M_{energy} + M_{hydro} + M_{nav} + \rho_f V_f + \rho_{cb} V_{cb}}{V_{tot}}$
Total volume	Internal volume is completely filled	$V_{tot} = \pi R_{out}^2 L = V_{hull} + V_{energy} + V_{hydro} + V_{nav} + V_f + V_{cb}$
Total mass w/ fill		$M_{tot} = \rho_{sw} V_{tot}$
Total mass w/o fill		$M_{dry} = M_{tot} - \rho_f V_f$

σ_{max} = max hoop stress
σ_y = hull material yield stress
SF = safety factor (self-imposed)
p_{out} = max pressure on outside of hull
p_{in} = pressure on inside of hull
R_{in} = inner radius of hull
R_{out} = outer radius of hull
t = thickness of hull
p_{out} = external pressure on hull
ν = Poisson ratio of hull material
β = compressibility of fluid (units of 1/Pa)
E_{hull} = Young's modulus of hull material
p_{in} = internal pressure of hull
ρ_{sw} = density of seawater

ρ_f = density of material filling the hull (ex. oil, microballoons, etc)
ρ_{cb} = density of counter-ballast material
M_{hull} = mass of hull
M_{energy} = total mass of energy subsystem
M_{hydro} = total mass of hydrodynamics subsystem
M_{nav} = total mass of navtronics subsystem
M_{tot} = total *filled* mass of the entire system
M_{dry} = total *unfilled* mass of the entire system
V_f = total volume of fill material
V_{cb} = total volume of counter-ballast material in the hull volume
V_{energy} = total volume of energy subsystem
V_{hydro} = total volume of hydrodynamics subsystem in the hull
V_{nav} = total volume of navtronics subsystem in the hull
V_{tot} = total volume of the entire system

Figure A15: **Equations and variables for flooded hull concept.** The mass and volume of the vehicle were calculated using the equations in this figure. The hull was assumed to be thin-walled with a yielding failure mode.

Heat Transfer within a Flooded Hull

As part of the calculations to validate the flooded hull design, a heat transfer model was created to better understand the effects of cold ambient temperatures on the vehicle electronics. This model assumed two cylindrical components within the vehicle, one being the hull and the other being an additional pressure vessel to house the payload. This method is listed here for completeness.

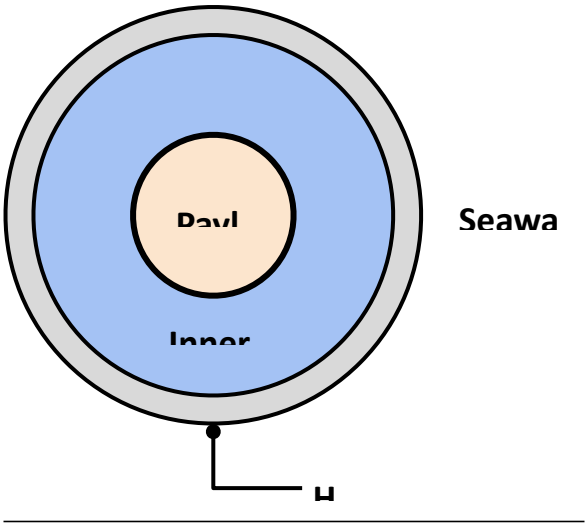

Figure A16: ***Diagram of a simplified Pressure Vessel.***

Taking RAPID's cylindrical geometry, we can simplify the structure to be two concentric cylinders within the ocean waters. This enables us to perform a one-dimensional analysis on the heat transfer going into/out of the payload. Here, the only dominant forms of heat transfer that have been considered are: conduction through the different media and the convection caused by water flow around the hull.

The final expression is at follows:

$$\dot{q}[\frac{1}{h_{sw}A_{outer}} + \frac{ln(r_{out}/r_{in})}{2\pi k_{hull}} + \frac{ln(r_{in}/r_{payload})}{2\pi k_{fluid}}] = (T_{\infty} - T_{payload})$$

h_{sw} = Convection Coefficient of Sea Water
$k_{hull/fluid}$ = Conduction Coefficient of Hull Material and Fill Fluid
$\dot{q}$ = Power Generation of Payload

Figure A17: ***Expression for Vessel's Temperature Drop.***

This expression requires knowledge on a few parameters: the thermal conductivities of the material comprising the hull, the heat per surface area generated by the payload, and the outside water temperatures. Of these, only the heat generated by the payload is expected to be the most variable depending on the power usage of the entire system.

References

[1] [2] [9] “AIR COOLED STACKS | HORIZON FUEL CELL TECHNOLOGIES,” duplicated [Online]. Available: https://www.horizonfuelcell.com/hseries.

[3] Sharkh, S., and Griffiths, G., 2003, “Energy Storage Systems for Unmanned Underwater Vehicles,” Underwater Technology, 25, pp. 143–148.

[4] “AIR COOLED STACKS | HORIZON FUEL CELL TECHNOLOGIES,” duplicated [Online]. Available: https://www.horizonfuelcell.com/hseries.

[5] [7] Fischman, J. Z., 2019, “The Development and Characterization of Aluminum Fueled Power Systems and a Liquid Aluminum Fuel,” Thesis, Massachusetts Institute of Technology.

[6] “The Development and Characterization of Aluminum Fueled Power Systems and a Liquid Aluminum Fuel.”

[8] “Parker - 1/4" Port, 4" High x 1.56" Wide, FRL Filter with Stainless Steel Bowl & Manual Drain - 60314754 - MSC Industrial Supply” [Online]. Available: https://www.mscdirect.com/product/details/60314754?fromRR=Y.

[10] “Bypass Diodes | PVEducation” [Online]. Available: https://www.pveducation.org/pvcdrom/modules-and-arrays/bypass-diodes.

[11] “Shading Losses for PV Systems and Techniques to Mitigate Them,” Aurora Solar Blog.

[12] Marion, B., Adelstein, J., Boyle, K., Hayden, H., Hammond, B., Fletcher, T., Canada, B., Narang, D., Kimber, A., Mitchell, L., Rich, G., and Townsend, T., 2005, “Performance Parameters for Grid-Connected PV Systems,” Conference Record of the Thirty-First IEEE Photovoltaic Specialists Conference, 2005., IEEE, Lake buena Vista, FL, USA, pp. 1601–1606.

[13] Dupré, O., Vaillon, R., and Green, M. A., 2015, “Physics of the Temperature Coefficients of Solar Cells,” Solar Energy Materials and Solar Cells, 140, pp. 92–100.

[14] “PowerFilm Solar: Electronic Component Solar Panels Spec Sheet.”

[15] “Solar Radiation on a Tilted Surface | PVEducation” [Online]. Available: https://www.pveducation.org/pvcdrom/properties-of-sunlight/solar-radiation-on-a-tilted-surface.

[16] [17] Fischman, J. Z., 2019, “The Development and Characterization of Aluminum Fueled Power Systems and a Liquid Aluminum Fuel,” Thesis, Massachusetts Institute of Technology.

[18] “Magnetic Coupling | Magnetic Drive Pump | Magnetic Technologies Ltd.”

[19] Fallon, M. F., Papadopoulos, G., and Leonard, J. J., 2010, “A Measurement Distribution Framework for Cooperative Navigation Using Multiple AUVs,” 2010 IEEE International Conference on Robotics and Automation, pp. 4256–4263.

[20] 2008, “Weight-Shift Control Aircraft Flying Handbook, FAA-H-8083-5.”

[21] “Linear-Quadratic Regulator (LQR) Design.” https://www.mathworks.com/help/control/ref/lqr.html.
[22] Osborne, J., and Rysdyk, R., “Waypoint Guidance for Small UAVs in Wind,” Infotech@Aerospace, American Institute of Aeronautics and Astronautics.
[23] News, C. H., E&E, “Ocean Currents Are Speeding Up, Driven by Faster Winds,” Scientific American [Online].
[24] [30] [33] [34] [38] Awale, S., Beeman, M., Bui, T., Correa, M., Fritzinger-Pittman, N., Gomes, C., Konuru, J., Li, S., Meyer, C., Neil, L., Paul, J., Pierre, J., Quenon, V., Raven, M., Sison, E., Smith, M., and Zheng, O, 2020, “R.A.P.I.D.”
[25] “Raspberry Pi 4 Model B (4 GB) - DEV-15447 - SparkFun Electronics” [Online]. Available: https://www.sparkfun.com/products/15447.
[26] [50] [52] “Raspberry Pi 4 Model B Datasheet.” Available: https://www.raspberrypi.org/documentation/hardware/raspberrypi/bcm2711/rpi_DATA_2711_1p0_preliminary.pdf.
[27] “Best MicroSD Cards for Raspberry Pi,” Tom’s Hardware [Online]. Available: https://www.tomshardware.com/best-picks/raspberry-pi-microsd-cards.
[28] “MicroSDHC PRO Endurance Memory Card w Adapter 32GB Memory & Storage - MB-MJ32GA/AM | Samsung US,” Samsung Electronics America [Online]. Available: https://www.samsung.com/us/computing/memory-storage/memory-cards/microsdhc-pro-endurance-memory-card-w-adapter-32gb-mb-mj32ga-am/.
[29] [31] [32] “SparkFun OpenLog Artemis - DEV-16832 - SparkFun Electronics” [Online]. Available: https://www.sparkfun.com/products/16832.
[35] [36] “SparkFun GPS-RTK Board - NEO-M8P-2 (Qwiic) - GPS-15005 - SparkFun Electronics” [Online]. Available: https://www.sparkfun.com/products/15005.
[37] [39] “Qwiic Iridium 9603N - SPX-16394 - SparkFun Electronics” [Online]. Available: https://www.sparkfun.com/products/16394.
[40] “RockBLOCK 9603 | Rock Seven” [Online]. Available: https://www.rock7.com/products/rockblock-9603-compact-plug-play-satellite-transmitter.
[41] [42] Olsen, J., “Sensor Technology SQ26-01 Hydrophone - Research Hydrophones,” Cetacean Research Technology [Online]. Available: https://www.cetaceanresearch.com/hydrophones/sq26-01-hydrophone/index.html.
[43] [44] “Glider Payload CTD (GPCTD) | Sea-Bird Scientific - Overview | Sea-Bird” [Online]. Available: https://www.seabird.com/moving-platform/glider-payload-ctd-gpctd/family?productCategoryId=54627473789.
[45] “NAVAIR 01-1A-509-1 NAVAIR CLEANING CORROSION CONTROL” [Online]. Available: http://everyspec.com/USN/NAVAIR/NAVAIR_01-1A-509-1_8121/.
[46] Tseng, W. J., “Chapter 4: Other Tests of Plastic Behavior,” p. 11. Available: http://audi.nchu.edu.tw/~wenjea/mechanical103/Chapter_4.pdf.

[47] Ross, C., Bowler, T., and Little, A., 2009, “Collapse of Geometrically Imperfect Stainless Steel Tubes under External Hydrostatic Pressure,” Journal of Physics: Conference Series, 181, p. 012030.
[48] Online Metals (n.d.). Retrieved November 23, 2020, from https://www.onlinemetals.com/en/aluminum-tolerances
[49] “NWS JetStream - Layers of the Ocean” [Online]. Available: https://www.weather.gov/jetstream/layers_ocean.
[51] “Raspberry Pi GPIO Pinout: What Each Pin Does on Pi 4, Earlier Models,” Tom’s Hardware [Online]. Available: https://www.tomshardware.com/reviews/raspberry-pi-gpio-pinout,6122.html.
[53] Wood, S., and Pardis, R., 2013, “Inexpensive Expendable Conductivity Temperature and Depth (CTD) Sensor.”
[54] “Technical Guides - Speed of Sound in Sea-Water” [Online]. Available: http://resource.npl.co.uk/acoustics/techguides/soundseawater/content.html.
[55] [56] Ghanbari Ghazijahani, T., Sadighi Dizaji, H., Nozohor, J., and Zirakian, T., 2015, “Experiments on Corrugated Thin Cylindrical Shells under Uniform External Pressure,” Ocean Engineering, 106, pp. 68–76.
[57] Contech Engineered Solutions. “Corrugated Metal Pipe Design Guide.” Available: https://www.conteches.com/Portals/0/Documents/Design%20Guides/CMP-Design-Guide.pdf?ver=2018-05-16-083622-383.
[58] “What Is Hydroforming,” American Hydroformers. Available: https://americanhydroformers.com/what-is-hydroforming/.
[59] Roark, R. J., Young, W. C., and Budynas, R. G., 2002, Roark’s Formulas for Stress and Strain, McGraw-Hill, New York.